Durham E-Theses

A High-speed THz Imaging System based on THz-to-optical Conversion in Atomic Vapour

DOWNES, LUCY,ALEXANDRA

How to cite:

DOWNES, LUCY,ALEXANDRA (2020) *A High-speed THz Imaging System based on THz-to-optical Conversion in Atomic Vapour*, Durham theses, Durham University. Available at Durham E-Theses Online: http://etheses.dur.ac.uk/13797/

A High-speed THz Imaging System based on THz-to-optical Conversion in Atomic Vapour

Lucy A. Downes

A thesis submitted in partial fulfilment
of the requirements for the degree of
Doctor of Philosophy

Quantum Light and Matter
Department of Physics
Durham University
November 13, 2020

A High-speed THz Imaging System based on THz-to-optical Conversion in Atomic Vapour

Lucy A. Downes

November 13, 2020

Abstract

This thesis investigates the interaction between Rydberg atoms and THz radiation and details development of an atom-based imaging system for THz frequency fields. Room temperature caesium atoms are excited to a Rydberg state using resonant infrared lasers and the response of these atoms to THz radiation is studied in multiple ways. We look at the absorption of the initial excitation laser and show how the observed lineshape changes in response to an applied THz field. We use this to measure the power of a THz field across a range of $350\,\mathrm{GHz}$. These measurements also lead us to determine values for the quantum defects in caesium without reliance on data from any other sources. These values agree within error with those previously reported in literature. We study the optical fluorescence emitted by the laser-excited vapour and develop a model to predict this emission. We highlight deviations from this model and suggest possible mechanisms for this discrepancy. We show how this model can be used to determine the optimum transition for atom-based THz imaging within our experimental parameters. We demonstrate a high-speed THz imaging system using Rydberg atoms and show that it has near diffraction-limited spatial resolution and is able to capture images at kHz framerates. We measure the minimum THz power that the system can detect and show how it compares to other technologies. This system is then used to perform some proof-of-principle experiments to highlight its usefulness in commercial settings. Using optical elements designed and produced in-house we create and characterise THz vortex beams with both radial and azimuthal phase. We show how these beams are similar to Laguerre-Gauss modes and highlight some important differences.

Declaration

The work in this thesis is based on research carried out in the Quantum Light and Matter group, Department of Physics, Durham University. No part of this thesis has been submitted elsewhere for any other degree or qualification, and it is the sole work of the author unless referenced to the contrary in the text.

Acknowledgements

First and foremost I would like to thank my supervisors, Kevin and Charles, for their patience, understanding and guidance over the past 4 years. Thank you for believing in me even when I'd stopped believing in myself, and for putting up with me sidetracking team meetings countless times. Throughout my PhD, Team THz$^{\text{TM}}$ has grown considerably and thanks must go to all members both past and present. I am indebted to Chris, Nikola and Dan for showing me the ropes and passing on your lab wisdom. I must also thank Terry for being an integral part of the experiment throughout. Thanks also to Ifan for lending me your ears, your words of wisdom and your cow-based magnetometry jokes. All three have been and continue to be invaluable.

Outside of the lab I have to thank the regular attendees at both fAtMol and Friday evening seminars for keeping me going. I would not have lasted a week without Lynne and Kathryn's supplies of coffee, chocolate and smiles. The Bransden Room has been my retreat many times when things in the lab weren't going well.

I am continually grateful for the encouragement and support of my family, without whom I would not be where I am today. Special thanks must go to my sister for her pep talks and relentless positivity, you are an inspiration. Also thanks to Kimi and Danny for your ability to cheer me up no matter what.

This thesis was written over the spring and summer of 2020, during the first peak of the Covid-19 pandemic. When we left the office on the 13$^{\text{th}}$ March I thought it would be for a month or so, I never thought I'd be finishing this thesis on my laptop in my bedroom. I could not have done this, or any of the last 4 years without the unwavering love, support and encouragement of my partner Ollie. Thank you so much.

Contents

List of Figures

List of Tables

Chapter 1

Introduction

The work in this thesis combines two very different topics; that of THz radiation which has traditionally been the realm of materials physics and engineering, and Rydberg atomic physics which has historically been reserved for lab-based studies and has only recently been shown to have practical applications [1]. While atom-based quantum technologies are progressing rapidly, the field of THz technology has been slower to progress. This thesis aims to use an example of an atom-based technology to bridge this so-called 'THz gap'.

1.1 Atom-based Sensors

Sensors based on probing atomic systems can offer high performance across a range of applications. Since atoms have well-known properties and give reproducible measurements that can easily be related to SI units, they are ideal candidates for use in a new generation of sensors in the growing field of quantum technology [2]. For example, atom-based sensors have been used for precise measurements of magnetic fields [3–5] and gravity [6,7] and are beginning to be marketed and used in fields as diverse as biomedical sensing [8], geomagnetic [9] and defence applications [10]. The advances in atomic vapour cell technology have allowed many of these experiments to take place in thermal atomic ensembles which removes the need for complex laser cooling and trapping arrangements. Combined with the progress in the miniaturisation of narrow linewidth laser technology, atom-based sensors are becoming

Property	n dependence
Binding energy	n^{-2}
Energy level spacing	n^{-3}
Orbital radius	n^2
Dipole moment $\langle nl|er|n'l'\rangle$	n^2
Polarisability	n^7
Radiative lifetime	n^3
Fine-structure interval	n^{-3}

Table 1.1: **Scaling properties of Rydberg atoms:** The scaling of various properties of Rydberg atoms as a function of principal quantum number n, adapted from Table 2.4 in [13].

marketable as sensitive portable devices [11, 12].

1.1.1   Rydberg Atoms

Rydberg atoms, named for the Swedish physicist Johannes Rydberg, are atoms in states of high principal quantum number n [13]. Since in these atoms the valence electron is far from the atomic nucleus, they are extremely sensitive to changes in their environment, be that an applied field or the presence of other Rydberg atoms. This sensitivity, combined with the fact that Rydberg states are comparatively long-lived, makes them ideal candidates for a wide range of applications including sensing and metrology [1]. The fact that properties of Rydberg atoms can be readily calculated using software packages such as `ARC` [14] makes interpretation of measurements somewhat more straightforward. The scaling with principal quantum number n of some key properties of Rydberg atoms are shown in Table 1.1.

Rydberg atoms have previously been shown to be excellent sensors for weak electromagnetic fields in the radio frequency, microwave and THz ranges [15–18], as well as for trace gas detection [19]. The ability of Rydberg atoms to provide IR-to-optical conversion has begun to be exploited [20–22] and imaging of high-power pulsed IR [23] and THz [24] fields has been demonstrated using a Rydberg atom

photocathode. The work presented in this thesis outlines the use of Rydberg atoms
in a thermal ensemble to detect and image THz frequency fields, combining the
growing fields of thermal Rydberg technologies and THz imaging.

1.2   The THz Band

The THz band is commonly defined as the section of the electromagnetic (EM)
spectrum in the 0.1-10 THz range, lying between the far infrared (IR) and microwave
regions [25]. Its ability to penetrate everyday materials such as paper, cloth and
plastics make it a promising candidate for use in non-destructive testing [26, 27],
while the fact that it is non-ionising gives it potential for use in security screening [28]
and biomedical settings [29]. Semiconductor-based devices used to detect visible and
IR light fail at such long wavelengths while electronic techniques used for microwave
and radio frequency technologies are unsuitable for the high frequencies of the THz
band. This means that despite a plethora of potential uses there is limited uptake
of technologies operating in the THz range, a phenomenon referred to as the THz
gap [30].

1.2.1   THz Imaging

THz imaging has potential uses across a broad range of applications including tu-
mour detection in medicine [29,31], quality control in manufacturing [32] and threat
detection in security [28]. However there are still technological challenges to over-
come before its usefulness can be fully realised. Current THz imaging technologies
can generally be divided into those which raster a single point detector to form an
image pixel by pixel, and others adopting a full-field approach to capture a 2D image
in one shot. Obviously each method has its own advantages and drawbacks and a
technology that satisfies the needs of most end-users is yet to be developed [25].

Single Pixel Methods

Single-pixel imaging systems often trade temporal resolution for an increase in their
spatial resolution. Single point detectors can be used to collect high-resolution

images pixel by pixel [33] but have yet to demonstrate real-time capabilities. Techniques employing thermal detectors have the advantage of being able to detect radiation over a wide frequency range [34]. The most commonly used thermal THz detectors are Golay cells [35] which rely on the heating and expansion of a gas and pyroelectric detectors. While both of these detectors operate at room temperature they are inherently slow with time constants on the order of 1 second, and are susceptible to noise [36]. While some techniques such as self-mixing in quantum cascade lasers (QCLs) can capture pixel data at significantly higher rates [37], they are limited by the speed at which they can raster between pixels. Even systems using a fast beam-deflection method for scanning between pixels only achieve an optimum acquisition rate of 240 µs per 0.5 mm pixel [38]. Systems employing digital mirror devices (DMDs) to create coded apertures can image at spatial resolutions below the diffraction limit [39,40] but again the added processing time needed to acquire data for each image (1 s [39]) makes this method unsuitable for true real-time applications. Progress has been made using THz spatial light modulators (SLMs) to perform compressive sensing but again the reported framerates remain below 10 Hz [41].

Focal Plane Arrays (FPAs)

Full-field THz imaging techniques, in which a complete image is collected in a single shot, eliminate the need to scan between individual pixels. These schemes typically consist of arrays of small point detectors such as microbolometers [42,43], field-effect transistors (FETs) [44] or carbon nanotubes [45]. Such arrays can operate at video frame-rates of up to 90 Hz [46] but their sensitivities are limited and scaling to large pixel numbers can be challenging [47]. More sensitive arrays such as those based on superconductors [48] suffer similar scaling problems and rely on cryogenic cooling to overcome thermal noise, making them cumbersome, expensive and complex to operate.

Frequency Conversion

Another promising approach to full-field THz imaging is frequency up-conversion, where a nonlinear optical material such as diamond [49] or DAST crystal [50] is used to convert incident THz photons to more easily-detectable wavelengths allowing images to be collected using standard optical or IR cameras. Typically the conversion process requires very high intensity THz fields to obtain usable signal levels. Consequently these devices can only be used with pulsed THz fields, limiting their duty cycle and thus their framerate. Recently, an efficient THz-to-optical conversion technique was reported [51] in which THz radiation is converted to visible light using a room-temperature atomic vapour, however far-field imaging capabilities were not demonstrated.

Despite the high demand across a wide range of practical applications, a room-temperature THz imaging system combining both high speed and sensitivity has yet to be realised [25, 30, 33]. In this thesis we aim to build on the work in [51] to develop a far-field THz imaging technique based on THz-to-optical conversion in a room-temperature atomic vapour.

1.3 Thesis Structure

The first chapter will be devoted to the theoretical background of the relevant atomic physics and will introduce concepts that will be referred to throughout. We then go on to describe details of the experimental methods used in the subsequent chapters. This includes descriptions of experimental layouts, equipment and data taking procedures.

In Chapter 4 we use Rydberg atoms to measure the power of an incident THz field through the Rydberg electrometry technique across a broad (350 GHz) frequency range. We also use this data to calculate values of the quantum defects in caesium without reliance on data from other sources.

Chapter 5 investigates the fluorescence emitted by the atomic vapour both with and without an applied THz field. We identify the origin of various fluorescence lines and attempt to develop a simple model to predict the fluorescence emitted from any

given Rydberg state. We also look at the dependence of different fluorescence lines with temperature and note some interesting features that are not predicted in the simple model. The model is used to select the best transition to perform THz imaging experiments within the limits of our experimental system.

In Chapter 6 we describe and characterise an atom-based THz imaging system. We show that it has near diffraction limited spatial resolution and can image at frame rates of up to 6 kHz. We discuss where this novel approach fits within existing THz technologies and consider simple improvements to the system. We then go on to use this system to demonstrate some real-world applications in Chapter 7. We perform proof-of-principle experiments in food quality monitoring and non-destructive testing to give examples of how this system might be commercialised.

In Chapter 8 we investigate creating THz vortex beams with radial and azimuthal phase using Teflon phase plates. We use our imaging system to characterise these beams and their properties, and discuss how they compare to Laguerre-Gauss beams.

1.4   Publications

The following publications have arisen from work described in this thesis:

- L. A. Downes, A. R. MacKellar, C. S. Adams, and K. J. Weatherill, "High-speed thz imaging for production line monitoring," in *2019 44th International Conference on Infrared, Millimeter, and Terahertz Waves (IRMMW-THz)*, pp. 1–2, 2019

- L. A. Downes, A. R. MacKellar, D. J. Whiting, C. Bourgenot, C. S. Adams, and K. J. Weatherill, "Full-field terahertz imaging at kilohertz frame rates using atomic vapor," *Phys. Rev. X*, vol. 10, p. 011027, Feb 2020

- L. A. Downes, C. S. Adams, I. G. Hughes and K. J. Weatherill, "Measurements of quantum defects in Cs using THz-frequency transitions in a thermal vapour," *In preparation*

- L. A. Downes, D. J. Whiting, C. S. Adams and K. J. Weatherill, "Spectral emission of a thermal Rydberg gas," *In preparation*

Chapter 2

Atom-Light Theory

In this chapter we will establish some of the theoretical concepts that underpin the work in this thesis. We will first describe how atomic structure is calculated and how this is relevant to the atomic species used in this work. We then go on to describe interactions between atoms and light fields, stating important results that will be relevant throughout. It is important to note that most of the calculations of values for atomic properties such as matrix elements and transition frequencies were performed using the Alkali Rydberg Calculator in Python (`ARC`) [14] and not calculated from scratch. Hence in this chapter we describe the methods used in this module and adopt the corresponding conventions.

2.1   Atomic Structure

In 1885, Balmer defined an empirical formula to predict the wavelengths of the spectral lines that had been previously observed in hydrogen (the Balmer series). This inspired Rydberg to propose the Rydberg formula in 1888, which gave the wavelength λ of the lines as

$$\frac{1}{\lambda} = R \left(\frac{1}{n^2} - \frac{1}{n'^2} \right),\tag{2.1.1}$$

where n, n' are integers and R is a constant now known as the Rydberg constant. This more general formula led to the discovery of other spectral line series in hydrogen, for example the Paschen and Lyman series. At its conception this was still

an empirical formula, and it would not be until 1913 that Bohr's model of the atom provided an explanation of its origins. The Bohr equation [54][eqn. 2.20] gives the energy levels of hydrogen as

$$E = -hc\frac{R_\infty}{n^2}, \tag{2.1.2}$$

where R_∞ is the Rydberg constant, n is the atomic principal quantum number and h and c are the Planck constant and speed of light respectively. The physics behind the discrete nature of atomic energy levels would not be described until the advent of quantum mechanics in the 1920s.

In a quantum-mechanical description an electron can be described through its wavefunction, ψ. The Schrödinger equation for an electron subject to a Coulomb potential $V(r)$ can be written

$$\left(\frac{-\hbar^2}{2m_\mathrm{e}}\nabla^2 + V(r)\right)\psi = E\psi, \tag{2.1.3}$$

where ψ is the wavefunction of the electron with mass m_e. In this case of a spherically symmetric potential the wavefunction can be written as

$$\psi(r, \theta, \phi) = R_{n,l}(r)Y_{l,m}(\theta, \phi), \tag{2.1.4}$$

where n, l and m are the principal, angular momentum and magnetic quantum numbers respectively. Here the radial part of the solution is described by $R_{n,l}(r)$ and the angular dependence is given by the spherical harmonic $Y_{l,m}(\theta, \phi)$. For each value of l we have $2l + 1$ possible values of m, ranging from $-l$ to l.

2.1.1 Corrections to the Schrödinger Picture - Fine Structure

The Dirac picture introduces extra terms in the hydrogen Hamiltonian; the spin-orbit, kinetic and Darwin terms [54]. The Darwin term is a result of a relativistic correction which shifts the levels for which $l = 0$ while the spin-orbit term causes levels with $l > 0$ to be split. For the heavier alkalis only the spin-orbit term is significant, so we will focus on this. This spin-orbit, or $\mathbf{L} \cdot \mathbf{S}$, coupling arises from the coupling of the orbital angular momentum L and spin S of the electron, leading to the emergence of fine structure in atomic energy levels. In this coupling scheme the total angular momentum of the electron is given by $J = L+S$, and the new total

angular momentum quantum number j can take values in the range $|l-s| \leq j \leq l+s$. For atoms with a single valence electron $s = 1/2$, so this interaction splits each $nl > 0$ level into two with values of $j = l \pm 1/2$. The energy separation of these fine structure levels is given by the Landé formula [54][eqn. 4.13], which shows an approximate scaling with principal quantum number as n^{-3}. Now l, m_l are no longer good quantum numbers to describe the system, instead we use l, j, m_j. When referring to atomic energy levels in this thesis we use the notation nL_j where the value of L is expressed as the letters S, P, D for $l = 0, 1, 2$ etc. In this notation the ground state of Cs can be described by the quantum numbers $n = 6$, $l = 0$, $j = 1/2$ so is written as $6S_{1/2}$.

2.1.2 Hyperfine Structure

The total angular momentum of the electron J couples to the total nuclear angular momentum I to give the total angular momentum $F = I + J$. The associated quantum number F takes values in the range $|J - I| \leq F \leq J + I$, thus splitting each fine-structure state into multiple hyperfine states. The energy shift of these hyperfine states can be found through [54][eqn. 6.9]

$$E_{\text{HFS}} = \frac{A_{\text{HFS}}}{2} \left(F(F+1) - I(I+1) - J(J+1) \right), \quad (2.1.5)$$

where the magnetic dipole constant A_{HFS} is unique for each value of l and J. For levels with $j \neq 1/2$ there is an additional magnetic quadrupole term B_{HFS}, but this is a small correction so has not been included here. Each hyperfine level F has $2F + 1$ magnetic (Zeeman) sub-levels, labelled as m_F. At zero field these levels are degenerate, but this degeneracy is lifted in the presence of a magnetic field.

2.1.3 Alkali Metals

The alkali metals, particularly rubidium and caesium, have become the go-to atomic species for atomic physics experiments. This is partly due to their high room-temperature vapour pressures and the relative simplicity of their structure, but also due to fortunate coincidences in early laser technology. The first cheap commer-

cial diode lasers used in CD players operated close to a ground-state transition in rubidium (780 nm) making experiments more viable [55].

The alkali metals can be described as hydrogenic, meaning that their structure can be well approximated by a central 'core' potential and a single valence electron. This means that the results for hydrogen can be easily generalised to describe their structure. For example to generalise equation 2.1.2 to the alkalis we include the quantum defect $\delta_l(n)$ as [54][eqn. 4.1]

$$E(n, l) = -hc\frac{R_\infty}{(n - \delta_l(n))^2}.$$ (2.1.6)

The quantum defect arises from the need to correct for the interaction of the valence electron with a core potential of differing sizes. The l dependence of the quantum defect arises from the differing radial dependences of the wavefunction for different values of l. Lower l states have a greater overlap with the core potential, leading to a larger quantum defect. For higher values of l the wavefunction is very similar to that of hydrogen and we find that for these levels $\delta_l \approx 0$ [54][pg. 63]. Often the quantum defects are specified separately for each j state, leading to a j dependence alongside the l and n dependences. The quantum defects for each l, j state can be parameterised by a modified Rydberg-Ritz equation [13][eqn. 16.19]

$$\delta_{l,j}(n) = \delta_0 + \frac{\delta_2}{(n - \delta_0)^2} + \frac{\delta_4}{(n - \delta_0)^4} + \frac{\delta_6}{(n - \delta_0)^6} + \cdots.$$ (2.1.7)

For states with large n the higher order terms are neglected so that the quantum defects are often described in terms of the coefficients $\delta_{0,2,4}$.

2.1.4 Electric Dipole Transitions

The strongest coupling between atomic states is due to coupling with the electric dipole moment of the valence electron, $\boldsymbol{\mu} = e\mathbf{r}$. We can define the dipole operator as $\mu = e\mathbf{r} \cdot \hat{\mathbf{e}}$ where $\hat{\mathbf{e}}$ is the unit vector in the direction of the electric field polarisation.

The dipole matrix element for the transition between states a and b can be written in integral form as

$$\mathbf{d}_{ba} = -e \int \psi_b^*(\mathbf{r}) \mu \psi_a(\mathbf{r}) \mathrm{d}\mathbf{r}.$$ (2.1.8)

If the states a and b are well described by the quantum numbers (n, l, m) and (n', l', m') respectively, then using equation 2.1.4 the wavevectors $\psi_{a,b}$ can be expressed as

$$
\psi_a(\mathbf{r}) = R_{n,l}(r) Y_{l,m}(\theta, \phi)
$$
$$
\psi_b(\mathbf{r}) = R_{n',l'}(r) Y_{l',m'}(\theta, \phi).
$$

(2.1.9)

This separation means that the integral in equation 2.1.8 can be separated into radial and angular parts. The solution for the radial part of the integral is finite but the angular part is only non-zero in specific cases and is dependent on the relative orientation of the vectors $\mathbf{r}$ and $\hat{\mathbf{e}}$ in the dipole operator. We can decompose the polarisation vector $\hat{\mathbf{e}}$ into three components with respect to the quantisation axis of the atom; one aligned with the quantisation axis (π) and two others rotating in opposite directions in the plane normal to the quantisation axis ($\sigma^{\pm}$) [54][pg 30]. We can then transform the polarisation vector from the cartesian basis into a new set of basis vectors where

$$
\epsilon_0 = e_z
$$
$$
\epsilon_{\pm 1} = \frac{1}{\sqrt{2}}(e_x \pm i e_y).
$$

(2.1.10)

The dipole operator can then be related to the spherical harmonics through

$$
\mu_q = e\mathbf{r} \cdot \boldsymbol{\epsilon}_q = r\sqrt{\frac{4\pi}{3}} Y_{l,q}(\theta, \phi),
$$

(2.1.11)

where $q = -1, 0, +1$ correspond to σ^-, π and σ^+ transitions respectively. The dipole matrix element can then be written as

$$
\langle n', l', j', m'_j | \mu_q | n, l, j, m_j \rangle = (-1)^{j'-m'_j} \begin{pmatrix} j' & 1 & j \\ -m'_j & q & m_j \end{pmatrix} \langle n', l', j' || \mu || n, l, j \rangle,
$$

(2.1.12)

where we have introduced the Wigner-3j coefficient $(\cdots)$ and the reduced matrix element $\langle \cdots || \mu || \cdots \rangle$. The reduced matrix element has no angular dependence and is related to the overlap between the wavefunctions and the dipole moment. It can be thought of as a measure of the coupling between states via all possible polarisations. The prefactor containing the angular dependence is sometimes referred to as the Clebsch-Gordan coefficient and depends on the value of q via the Wigner-3j symbol.

By considering the properties of the 3j symbol we find that it is only non-zero if $|j'-j| \leq 1 \leq j'+j$, giving the selection rule $\Delta j = 0, \pm 1$ for electric dipole transitions. The 3j symbol is also zero unless $m_j' = m_j + q$ leading to the selection rule that $\Delta m_j = 0$ for π transitions, and $\Delta m_j = \pm 1$ for $\sigma^{\pm}$ transitions. We also have a rule that $\Delta l \neq 0$ from the fact that electric dipole transitions couple states with opposite parity. These electric dipole selection rules allow us to determine which states can be coupled by the driving fields which will be important in Chapters 4 & 5. The calculation of the dipole matrix elements will enable us to see how strongly these transitions can be driven.

Transition Rates and Atomic Lifetimes

The rate of spontaneous decay from state a to b is given by the Einstein-A coefficient. This can be related to the reduced matrix element through [13]

$$A_{ba} = \frac{\omega_0^3}{3\pi\varepsilon_0 \hbar c^3} \frac{2J+1}{2J'+1} |\langle \cdots ||\mu|| \cdots \rangle|^2, \tag{2.1.13}$$

where ω_0 is the resonant frequency of the $|a\rangle \rightarrow |b\rangle$ transition and $\langle \cdots ||\mu|| \cdots \rangle$ is the reduced matrix element. In the case of zero temperature the only possible transitions out of a state would be to states of lower energy, so the lifetime τ_0 of the state can be found by summing over the Einstein-A coefficients of all allowed transitions,

$$\frac{1}{\tau_0} = \Gamma_0 = \sum_{E_a > E_b} A_{ba}. \tag{2.1.14}$$

However in reality we must include transitions induced due to the coupling with blackbody radiation (BBR). This will allow transitions to higher energy states to occur and hence will modify the state lifetime. The rate of transitions driven by BBR (Γ_{BBR}) is given by the Einstein-A coefficient multiplied by the number of photons per mode at the transition frequency, given by the Planck distribution. The effective lifetime of the state can then be found as the sum of the radiative and BBR-induced transition rates

$$\frac{1}{\tau_{\mathrm{eff}}} = \Gamma_0 + \Gamma_{\mathrm{BBR}}. \tag{2.1.15}$$

These calculations of transition rates will be relevant in Chapter 5 when we model fluorescence arising from spontaneous and blackbody induced decay in a thermal

vapour. The calculations of radiative lifetimes are used in Chapter 6 when we consider the limits of processes that depend on the lifetime of the atomic state used.

2.2 Atom-Light Interactions

In order to model how a single atom interacts with electromagnetic (EM) fields, we take a semi-classical approach in which the radiation field is considered as classical but the atom is considered quantum mechanically. We will first look at the simplest case of a two-level atom interacting with a monochromatic near-resonant field. The total Hamiltonian H of the system is made up of two parts [54]

$$H = H_0 + H_{\text{INT}}(t), \tag{2.2.16}$$

where H_0 is the bare atomic Hamiltonian in the absence of any radiation and H_{INT} describes the interaction with a time-dependent electromagnetic field. To begin with we will ignore the effects of dephasing processes and focus only on the coherent dynamics of the system. For our two level atom with ground state $|1\rangle$ and excited state $|2\rangle$ we can write the wavevector $\psi = c_1|1\rangle + c_2|2\rangle$ where $c_{1,2}$ are coefficients relating to the probability of being in the ground and excited state respectively. If the two levels have energies E_1 and E_2, we can write the bare atomic Hamiltonian as

$$H_0 = \begin{pmatrix} E_1 & 0 \\ 0 & E_2 \end{pmatrix}. \tag{2.2.17}$$

Treating the electromagnetic field classically means it can be modelled as a simple oscillating field propagating in the z direction. The electric field is then given by $\mathbf{E} = E_0 \boldsymbol{e} \cos(kz - \omega t)$ where $\boldsymbol{e}$ is the polarisation vector and ω is the frequency of the field. Since we will consider interactions with only visible, infra-red and THz radiation we can neglect the z dependence of the electric field. This is the dipole approximation and is valid since the scale of the atomic wavefunctions is much smaller than the wavelength of the light. In this approximation the electric field can be written $\mathbf{E} = E_0 \boldsymbol{e} \cos(\omega t)$. The field interacts with the atom via the dipole operator μ as described previously, leading to an interaction Hamiltonian of the

form

$$H_{\text{INT}} = -\mu E_0 \cos(\omega t). \tag{2.2.18}$$

The total system Hamiltonian can then be written as

$$H = \begin{pmatrix} E_1 & \hbar\Omega(t)\cos(\omega t) \\ \hbar\Omega^*(t)\cos(\omega t) & E_2 \end{pmatrix}, \tag{2.2.19}$$

where we have defined the Rabi frequency as

$$\Omega(t) = \frac{\langle 1|\mu E_0|2\rangle}{\hbar} \tag{2.2.20}$$

$$= \frac{E_0 \mathbf{d}_{21}}{\hbar}, \tag{2.2.21}$$

with the dipole matrix element $\mathbf{d}_{21}$ defined in equation 2.1.12.

2.2.1 Dressed Atom Approach

Making the rotating wave approximation which transforms into a frame rotating with the frequency of the driving field allows the rapidly oscillating terms to be neglected, and introducing the detuning $\Delta = \omega - \omega_0$ where ω_0 is the resonant frequency of the transition allows us to write the total Hamiltonian in equation 2.2.19 as

$$H_{\text{TOT}} = \frac{\hbar}{2} \begin{pmatrix} 0 & \Omega \\ \Omega & -2\Delta \end{pmatrix}. \tag{2.2.22}$$

This combined atom-light Hamiltonian allows us to explore properties of the coupled atom-light system. The effective energy levels of the atom-light system $E_{\pm}$ are found as the eigenvalues of this Hamiltonian and are given by

$$E_{\pm} = -\frac{\hbar\Delta}{2} \pm \frac{\hbar}{2}\sqrt{\Delta^2 + \Omega^2}. \tag{2.2.23}$$

In the absence of the field (i.e. for $\Omega = 0$) the eigenstates are the bare states of the system ($|1\rangle$ and $|2\rangle$), but when considering the coupled laser-atom system the bare states are no longer eigenstates. For a near resonant field (i.e. for $\Delta \approx 0$) the eigenstates are given by

$$|\pm\rangle = \frac{1}{\sqrt{2}}\left(|1\rangle \pm |2\rangle\right). \tag{2.2.24}$$

These new states are known as dressed states, and are linear superpositions of the bare states. From the eigenenergies in equation 2.2.23 it can be seen that for increasing Ω the levels $E_\pm$ will be shifted further from each other; an effect known as the AC Stark effect or light shift [54].

Three-Level System

When considering the simple case of a two-level system we did not have to pay attention to the configuration of the states, however as we add more states and fields coupling these states we need to think about how they are connected. The most straightforward case, and the case used for the work in this thesis, is that of a 'ladder' configuration in which the state $|i+1\rangle$ is higher in energy than state $|i\rangle$. Each state is only coupled to the one directly above by a field with Rabi frequency $\Omega_{i,i+1}$ which is detuned from resonance by $\Delta_{i,i+1}$. We can then extend our simple two-level model from the previous section to include an extra state $|3\rangle$ and driving field Ω_{23} that couples the intermediate and highest energy states. A diagram of this simple 3-level ladder scheme and the relevant parameters can be seen in Figure 2.1, *left*. For this 3-level system we apply the same methods and approximations as before and write the total Hamiltonian in the interaction picture as

$$H_{\text{TOTAL}} = \frac{\hbar}{2} \begin{pmatrix} 0 & \Omega_{12} & 0 \\ \Omega_{12} & -2\Delta_{12} & \Omega_{23} \\ 0 & \Omega_{23} & -2(\Delta_{12} + \Delta_{23}) \end{pmatrix}. \qquad (2.2.25)$$

To understand the dynamics of this atom-light system we look at the composition of the dressed states in certain conditions. First we consider the limit in which the coupling of the upper states is stronger than that of the lower states, $\Omega_{12} \ll \Omega_{23}$, known as the weak probe limit. Setting $\Omega_{12} = 0$ in equation 2.2.25 and solving for the eigenvectors yields the dressed states

$$|\pm\rangle = (\Delta_{23} \pm \sqrt{\Delta_{23}^2 + \Omega_{23}^2})|2\rangle + \Omega_{23}|3\rangle, \qquad (2.2.26)$$

with eigenenergies given by

$$E_\pm = -\frac{\hbar}{2}\left(2\Delta_{12} + \Delta_{23} \pm \sqrt{\Delta_{23}^2 + \Omega_{23}^2}\right). \qquad (2.2.27)$$
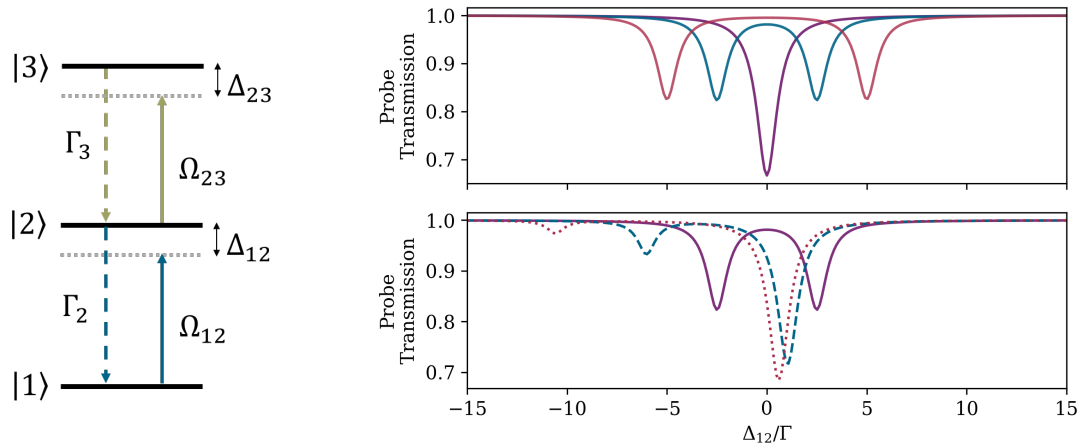
Figure 2.1: **Example of a theoretical 3-level ladder scheme and associated probe transmission spectra.** *Left:* The three levels are coupled by two driving fields with Rabi frequencies $\Omega_{12,23}$ that are detuned from resonance by $\Delta_{12,23}$. The decay out of the excited states is given by $\Gamma_{2,3}$. *Right:* Plots of the transmission of the probe laser (coupling states $|1\rangle$ and $|2\rangle$) under different circumstances. The top plot shows the result of increasing the value of Ω_{23}/Γ from 0 (purple line) to 5 and then to 10 (blue and red lines respectively). The features are separated by Ω_{23}. The lower plot shows the effect of increasing the value of Δ_{23}/Γ from 0 (purple line) to 5 and then to 10 (blue dashed and red dotted lines respectively), illustrating the asymmetry of the lineshape. The other parameters used were $\Omega_{12}/\Gamma = 1$, $\Gamma_2 = \Gamma_3 = \Gamma$.

When both beams are on resonance ($\Delta_{12,23} = 0$) the expression for the dressed states becomes $|\pm\rangle = 1/\sqrt{2}\,(|3\rangle \pm |2\rangle)$ and we see that their eigenenergies are separated by $\hbar\Omega_{23}$. This splitting of the bare states is known as the Autler-Townes effect [56]. If we vary the detuning of the first laser Δ_{12} the field will become resonant with a dressed state at $\Delta_{12} = \pm\Omega_{23}/2$ and its absorption profile will exhibit features separated by Ω_{23}, as shown in the top right-hand plot of Figure 2.1. For $\Delta_{23} = 0$ both dressed states contain an equal amount of the bare state $|2\rangle$ so the heights of the features in the absorption spectrum will be equal. Any detuning of the second field will result in an unequal mixture of the bare states in the dressed states and hence an asymmetric coupling to the ground state. This leads to features of unequal heights in the absorption spectra, as seen in the lower plot on the right-hand side

of Figure 2.1. This effect of detuning a coupling field is what gives rise to the asymmetric lineshapes seen in Chapter 4.

It is important to note that the composition of the dressed states means the system will be transparent to a resonant probe field ($\Delta_{12} = 0$). Even in cases of very small Ω_{23}, the transparency will remain as the dressed states are still the eigenstates of the system. This is no longer due to Autler-Townes splitting but is due to Fano interference between the decay pathways from the two dressed states [57]. This electromagnetically-induced transparency (EIT) can lead to very narrow transparency features that cannot be modelled as the sum of two displaced Lorentzian lineshapes. The distinction between Autler-Townes splitting and EIT is not well defined but it is generally accepted that EIT requires the condition of weak pump and probe fields (i.e. small $\Omega_{12,23}$) [57]. As Ω_{23} increases, Autler-Townes splitting becomes the dominant effect and the transparency window widens. The lineshapes seen in Chapter 4 are likely due to Autler-Townes splitting rather than EIT as we do not impose the condition of weak fields and they can be modelled as the sum of two Lorentzians.

2.2.2 Optical Bloch Equations

So far in our treatment of atom-light interactions we have not taken into account the effects of spontaneous emission on the evolution of the state vector $|\psi\rangle$. To this end we introduce the density matrix defined as $\hat{\rho} = |\psi\rangle\langle\psi|$ and consider its evolution instead of that of the state vector. This approach of finding the steady-state solutions of the density matrix will be important in our understanding and modelling of the system in Chapter 4.

The diagonal elements of the density matrix describe the evolution of the populations of the states $|1\rangle, |2\rangle$ and $|3\rangle$ respectively, while the off-diagonal elements describe the coherence between states which will allow us to extract measurable quantities. The coherent time evolution of the density matrix is given by the Liouville equation [58]

$$i\hbar\frac{d\hat{\rho}}{dt} = \left[\hat{H}, \hat{\rho}\right],$$

(2.2.28)

in which $\left[\hat{H}, \hat{\rho}\right]$ represents the commutator of the Hamiltonian $\hat{H}$ and the density matrix $\hat{\rho}$. This equation is analogous to the time-dependent Schrödinger equation for the state vector. In order to include dissipative effects we use the Master equation

$$\frac{d\hat{\rho}}{dt} = -\frac{i}{\hbar} \left[\hat{H}, \hat{\rho}\right] + \hat{\mathcal{L}}(\hat{\rho}), \qquad (2.2.29)$$

where again $\hat{H}$ is the Hamiltonian of the atom-light system and $\hat{\mathcal{L}}$ describes the decay/dephasing in the system.

Again we use the example of a 3-level ladder system with the total Hamiltonian given in equation 2.2.25 describing the coherent driving between levels in the system. The dissipative processes are included in the decay operator $\hat{\mathcal{L}}$ which can be split into two separate parts; one part describing the atomic decay $\hat{L}_{\text{atom}}$ and another describing dephasing due to the finite linewidths of the driving fields $\hat{L}_{\text{dephasing}}$. The total operator will then be the sum of these parts $\hat{\mathcal{L}} = \hat{L}_{\text{atom}} + \hat{L}_{\text{dephasing}}$.

First we focus on the Lindblad operator $\hat{L}_{\text{atom}}$ describing spontaneous decay between levels. In the ladder configuration we assume that each level decays to the level directly below it at a rate Γ_n, and that there is no decay out of the lowest energy level. In this case the off-diagonal elements will be given by $L_{ij,\, i\neq j} = -\frac{\Gamma_i+\Gamma_j}{2}\rho_{ij}$ while the diagonal elements will be given by $L_{ij,\, i=j} = \Gamma_{i+1,j+1}\rho_{i+1,j+1} - \Gamma_{ij}\rho_{ij}$ [59]. This means that for our example 3-level system we have

$$\hat{L}_{\text{atom}} = \begin{pmatrix} \Gamma_2\rho_{22} & -\frac{\Gamma_2}{2}\rho_{12} & -\frac{\Gamma_3}{2}\rho_{13} \\ -\frac{\Gamma_2}{2}\rho_{21} & \Gamma_3\rho_{33} - \Gamma_2\rho_{22} & -\frac{\Gamma_2+\Gamma_3}{2}\rho_{23} \\ -\frac{\Gamma_3}{2}\rho_{31} & -\frac{\Gamma_3+\Gamma_2}{2}\rho_{32} & -\Gamma_3\rho_{33} \end{pmatrix}, \qquad (2.2.30)$$

where we have made the assumption that there is no decay out of the lowest level ($\Gamma_1 = 0$). The dephasing due to the finite laser linewidths only affects the coherences (off-diagonal density matrix elements). The elements of the dephasing matrix can be expressed as $L_{ij,i\neq j} = -\left(\gamma_{i,i+1} + \cdots + \gamma_{j-1,j}\right)\rho_{ij}$ where $\gamma_{n,n+1}$ is the linewidth of the field coupling the n and $n+1$ levels [60]. Now we have expressions for the Hamiltonian and decay operator, we can substitute them into equation 2.2.29 to get an expression for the time evolution of the density matrix. In the case without dissipation, the solution to the evolution of the density matrix would be itself time-dependent and we would observe Rabi oscillations between the states. The inclusion

of the dephasing terms means that these oscillations will be damped and the system will reach a steady-state solution which is no longer time dependent. This steady-state solution can be found by setting $d\hat{\rho}/dt = 0$ in equation 2.2.29 and solving for $\hat{\rho}$.

Numerical Solutions

When written explicitly, equation 2.2.29 is a complex system of coupled equations that cannot easily be solved analytically. In cases such as the weak-probe regime simplifications can be made allowing for full analytic solutions to be extracted, but these approximations do not always hold. To this end we briefly describe solving equation 2.2.29 numerically without making any initial assumptions. This will be relevant in Chapter 4 when modelling our complex 5-level system.

To make this complex system of equations more convenient to solve we write them in the form $d\hat{\rho}_{\text{vect}}/dt = \hat{M}\hat{\rho}_{\text{vect}}$ where $\hat{\rho}_{\text{vect}}$ is a column vector containing all n^2 elements of $\hat{\rho}$, and $\hat{M}$ is an $n^2 \times n^2$ matrix of coefficients. We now have an expression for $d\hat{\rho}_{\text{vect}}/dt$ in terms of the matrix $\hat{M}$ multiplied by $\hat{\rho}_{\text{vect}}$. In the steady state, $d\hat{\rho}_{\text{vect}}/dt = 0$ so we need to solve the expression $\hat{M}\hat{\rho}_{\text{vect}} = 0$. This can be solved numerically by performing a singular value decomposition (SVD) on the matrix $\hat{M}$ [61]. The full details of the theory of the SVD are beyond this discussion, it is suffice to say that the SVD transforms $\hat{M}$ into three matrices such that $\hat{M} = U\Sigma V^{\text{T}}$. The matrix Σ is diagonal, the elements corresponding to the singular values of $\hat{M}$. The solution to the system of equations is then the column of V corresponding to the zero singular value. Since we have the same number of equations as we have unknowns we expect only one non-trivial solution. If none of the singular values are zero ($\hat{M}$ is non-singular) then there is no non-trivial solution. From this we can find the steady-state values of all elements in the density matrix, both populations and coherences. We assume that the population is conserved throughout the evolution, and so normalise the sum of the populations to be 1.

Measurable Quantities

We now have the values of the steady state density matrix elements, from which we can extract useful measurable quantities to compare to experiment. Often the experimental quantity of interest is the transmission of the probe laser, the laser coupling the lowest two levels (in this case $|1\rangle$ and $|2\rangle$). The absorption coefficient α can be found from the imaginary part of the complex susceptibility χ through $\alpha = k\mathrm{Im}[\chi]$ [60]. The susceptibility of the medium to the probe laser is related to the steady state coherence term ρ_{12} through

$$\chi = -\frac{2N|\mathbf{d}_{21}|^2}{\hbar\varepsilon_0\Omega_{12}}\rho_{12}, \qquad (2.2.31)$$

where N is the atomic number density and $\mathbf{d}_{21}$ is the dipole matrix element of the $|1\rangle \rightarrow |2\rangle$ transition. From these expressions it can be seen that the absorption of the probe $\alpha_{12} \propto -\mathrm{Im}[\rho_{12}]$ and hence the probe transmission can be approximated as $1+\mathrm{Im}[\rho_{12}]$. Since the numerical method described in the previous section calculates the steady state solution for the entire density matrix we can easily extract the susceptibility of the medium to any of the applied fields by using the appropriate coherence term and dipole matrix element in equation 2.2.31. For an atom at rest the probe transmission profile will have a Lorentzian shape, the width of which will be defined by the atomic linewidth. In reality the lineshapes observed in thermal vapour experiments are rarely Lorentzian in shape. To understand why, we need to consider the entire ensemble of atoms within the vapour.

2.2.3   Ensemble Effects

In all of the above we have assumed that the atoms are at rest and so all experience the same driving field frequencies. However in a thermal vapour this is not the case and the Doppler shift experienced by atoms with different velocities must be taken into account. The distribution of velocities within the thermal ensemble of atoms will be described by the Maxwell-Boltzmann distribution

$$f(v) = \frac{1}{u\sqrt{\pi}} \exp\left(\frac{-v^2}{u^2}\right), \qquad (2.2.32)$$

where u is the most probable velocity, given by $u = \sqrt{2kT/m}$ where k is the Boltzmann constant, T is the temperature and m is the mass of an atom [54]. From this it can be calculated that at room temperature atoms in a Cs vapour cell have a most probable velocity of around $200\,\mathrm{m\,s^{-1}}$. An atom moving with/against the direction of propagation of the laser field will see a red/blue-shift in the frequency of the field due to the Doppler effect. This can be taken into account in the Hamiltonian in equation 2.2.25 by replacing the detunings with the modified detunings $\Delta_{\mathrm{eff}} = \Delta + \mathbf{k} \cdot \mathbf{v}$ where $\mathbf{k}$ is the wavevector of the laser field, and $\mathbf{v}$ is the atomic velocity vector. Since in practice all our laser fields are colinear we only need to consider the velocity component along the propagation axis. In this case the expression for the modified detuning can be simplified to $\Delta_{\mathrm{eff}} = \Delta \pm kv$ where the plus/minus applies for atoms moving against/with the propagation direction.

In order to model the response of the entire thermal vapour, a range of velocity classes needs to be considered and then the response of each integrated with respect to their relative abundance. This leads to a broadening of the atomic lineshape such that the width is no longer defined by the atomic linewidth and is now defined by the temperature of the vapour, the Doppler width. At room temperature the Doppler width of alkali atomic vapours is several orders of magnitude larger than the atomic linewidth. For example the natural linewidth of the Cs D2 $6\mathrm{S}_{1/2} \rightarrow 6\mathrm{P}_{3/2}$ transition is $5.22\,\mathrm{MHz}$ [62], which is less than the hyperfine splitting of the $6\mathrm{P}_{3/2}$ state. At room temperature however the linewidth is Doppler broadened to around $500\,\mathrm{MHz}$ such that the individual hyperfine states are no longer resolved. The shape of these Doppler-broadened spectral lines is better described by a Gaussian than a Lorentzian. Often since spectral lines consist of many unresolved hyperfine transitions they are better approximated by a summation of several Gaussians, however if the hyperfine splitting is much smaller than the Doppler linewidth (such as for high values of n) they are well approximated by a single Gaussian.

2.3 Conclusion

In this chapter we have outlined the theory that underpins the concepts described in the rest of this thesis. We detailed calculations of atomic structure including fine and hyperfine splitting and described the method used to calculate dipole matrix elements for atomic transitions. We outlined a semi-classical approach to atom-light interactions and used this to arrive at the optical Bloch equations which allow our complex atomic system to be modelled numerically. We also briefly described the considerations we make due to the fact that the work is done in a thermal vapour so the atoms will experience Doppler-shifted driving fields. As highlighted previously, the calculations for atomic properties such as transition frequencies and dipole matrix elements used in this thesis were not performed from scratch but were instead calculated using the `ARC` package in Python [14], so we have adopted the same conventions.

Chapter 3

Experimental Methods

This chapter will provide details of the experimental set-up and methods used throughout this thesis. This will include details of the atomic system used, details of the laser and THz sources, and details of the methods used to collect data. The experiments described in this thesis can be broadly divided into two categories: electrometry experiments in which Rydberg spectroscopy is used to measure properties of an incident THz field, and imaging experiments in which the spatial distribution of the THz field is measured. While both of these experimental schemes rely on forming Rydberg atoms in an atomic vapour cell, the methods used differ significantly.

3.1   Atomic System

The atomic species used throughout this thesis is caesium (Cs). One advantage of using Cs over other commonly used alkalis is that there is only one stable isotope (^{133}Cs), meaning that we do not have to account for any isotope shifts in our calculations. Caesium has an atomic number density of $1 \times 10^{10} \, \mathrm{cm}^{-3}$ at 20℃ [62] meaning that all of our experiments can be done at room temperature or with moderate heating to around 60℃. In all experiments performed in this thesis the Cs vapour is contained within quartz vapour cells to allow optical access. We use a three-step excitation to reach the desired Rydberg level [63]. The probe laser (852 nm) excites atoms to the $6P_{3/2}$ state, and the coupling laser (1470 nm) takes atoms from the
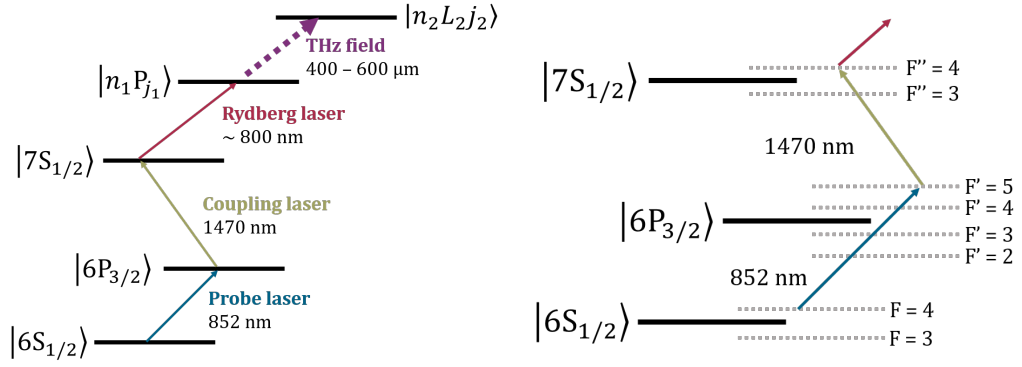
Figure 3.1: **Diagram of the atomic system used in this thesis.** *Left:* The atomic transitions in Cs and the corresponding laser excitations used in the Rydberg excitation scheme. The first two lasers always address the labelled transitions, whereas the Rydberg laser and THz field can be tuned to address different transitions. *Right:* Diagram showing the hyperfine levels used in the locking of the first two lasers in the excitation scheme. More details can be found in Appendix A.

$6P_{3/2}$ state to the $7S_{1/2}$ state. From here we have access to any nP Rydberg states up to the ionisation threshold. From these nP Rydberg states we can apply a resonant THz field to couple to either an S or a D state. This excitation scheme is depicted in Figure 3.1.

3.2 Laser Systems

Both probe (852 nm) and coupling (1470 nm) lasers are commercial ECDLs (Toptica DL100 and DLPro respectively) with sub-MHz linewidths and are frequency stabilised to atomic transitions as shown in Fig. 3.1. The probe laser is stabilised to the $6S_{1/2}$ F = 4 → $6P_{3/2}$ F' = 5 hyperfine transition using polarisation spectroscopy [64], while the coupling laser is stabilised to the $6P_{3/2}$ F' = 5 → $7S_{1/2}$ F'' = 4 using excited state polarisation spectroscopy [65]. More details of the laser stabilisation techniques can be found in Appendix A.

Two laser systems were used to provide the laser light for the final step in the excitation to the Rydberg state:

- a widely tunable (700 nm-1100 nm) MSquared SolsTiS titanium:sapphire laser

was used for the electrometry work in Chapter 4 to enable access to many different Rydberg states.

- a MOGLabs cateye diode laser system at 843 nm was used for the imaging experiments in Chapters 6, 7 and 8 once the optimum wavelength and laser parameters had been established.

Neither of these laser systems was actively frequency stabilised, however the frequency drift was over such long timescales (around 10 MHz per minute) that the laser frequency was considered constant throughout each individual exposure or measurement. This drift did however pose problems in taking longer term measurements.

3.3   THz Source

The THz field used in this work is both narrowband and continuous wave. It is generated using an amplifier multiplier chain (AMC), manufactured by Virginia Diodes Inc., which is seeded by a microwave signal generator (HP8672a). The AMC comprises a series of frequency multipliers utilising GaAs Schottky diodes to increase the input frequency while suppressing unwanted harmonic content. Again two different AMCs were employed:

- a low power (max. 50 µW) source tunable between 500 GHz and 750 GHz was used for the electrometry work in Chapter 4, in which access to many different THz frequency transitions was required. This source has a multiplication factor of 54.

- a higher power (max. 4 mW) source with a narrower tuning range (540 GHz to 560 GHz) was used for the imaging experiments once optimum parameters had been chosen. This source has a multiplication factor of 36.

For coarse control over the THz power Nylon attenuators were placed in the beam path. The transmission T of an attenuator of thickness l is given by the Beer-Lambert law [66]

$$T = e^{-\alpha l}, \tag{3.3.1}$$

where α is the absorption coefficient for the attenuator material. Nylon has an absorption coefficient of $\alpha = 5.5\,\mathrm{cm}^{-1}$ at $0.55\,\mathrm{THz}$ [67], so each of the $0.50\,\mathrm{cm}$ thick attenuators used reduced the transmitted THz power by a factor of 15.6. Fine attenuation is provided by the user-controlled attenuator (UCA) built into the THz sources which provides voltage-tunable attenuation. The frequency of both THz sources is controlled by tuning the frequency of the input microwave signal. The input microwave source has a frequency resolution of $2\,\mathrm{Hz}$ so we assume that the THz field has a linewidth of $n \times 2$ where n is the multiplication factor of the AMC. Since this is much narrower than any of the atomic transitions addressed it is neglected. The THz field is launched into free space using a diagonal horn antenna, again manufactured by Virginia Diodes Inc., with an approximately 84% Gaussian mode content [68]. In order to estimate the size of the THz beam at any given point we assume that the beam emerging from the horn is a perfect Gaussian described exactly by the parameters on the specification sheet [68]. The specification sheet for the diagonal horn antennas used gives a $3\,\mathrm{dB}$ beamwidth of $10\,°$. This is the angle between the points at which the intensity falls to half of its peak value, equal to the full width half maximum (FWHM). This can be related to the more commonly used definition of the $1/e^2$ Gaussian beam radius ω through

$$\omega = \frac{\mathrm{FWHM}}{\sqrt{2\ln 2}}, \tag{3.3.2}$$

allowing us to calculate the size of the beam as it propagates through the optics.

3.4   Data Readout

Multiple different methods were used to collect information about the response of the vapour to the applied THz field.

3.4.1   Probe Laser Transmission

An important source of information about the system is the probe laser transmission which can be monitored on a silicon photodiode (Thorlabs PDA8A/M). An interference filter centred on $852\,\mathrm{nm}$ was used before the photodiode to filter out

the copropagating coupling laser light. This photodiode signal was the source of the electrometry signals in Chapter 4 and as a guide for alignment of the light sheet used in later chapters.

3.4.2 Spectrometer

To collect spectral information about the fluorescence emitted from the vapour, as in Chapter 5, we use an OceanOptics USB fibre-coupled spectrometer (Flame-T, grating #9, 25 μm slit). The system was sensitive to wavelengths from 460 nm to 800 nm with a sub-nm resolution, allowing individual spectral lines to be resolved. A shortpass filter (Thorlabs FESH0750, 750 nm cut-off) was used to eliminate scattered light from the excitation lasers and collect data on the visible and NIR fluorescence.

3.4.3 Cameras

When performing the THz imaging experiments described in Chapter 6, three different optical cameras were used to record images of the fluorescence from the vapour. The true-colour images were taken using a commercial Nikon D5500 DSLR (henceforth referred to as DSLR) with an exposure time of 0.5 s, an F-stop of f/1.8 and an ISO of 100. An Andor iXon EMCCD camera (referred to as iXon) was used for high resolution low-noise images, running without water-cooling to the EMCCD. An exposure time of 200 ms was used for this camera with the EM gain set to minimum. A Photron FASTCAM SA4 (referred to as Photron) was used to record the high speed video at exposure times equal to the reciprocal of the frame rates stated. When using the iXon and the Photron cameras we use a simple 1 inch 1:1 Steinheil achromatic triplet lens to image the vapour, and bandpass filters (Semrock BrightLine 535/6nm and 505/119nm) to remove unwanted IR scatter and background fluorescence.

Pixel Size Calibration

Although the lens used on the iXon and the Photron is designed to be 1:1, the addition of the filters meant that the magnification was not exactly unity. In order to find the magnification of the lens and filters together we take images of an object

of well-known size (e.g. graduations on a ruler) and use this to calculate the size represented by each pixel. An example of this is shown in Fig. 3.2 for the iXon camera. This was done separately on both the iXon and the Photron due to the difference in pixel size and distance of the lens mount to the sensor.
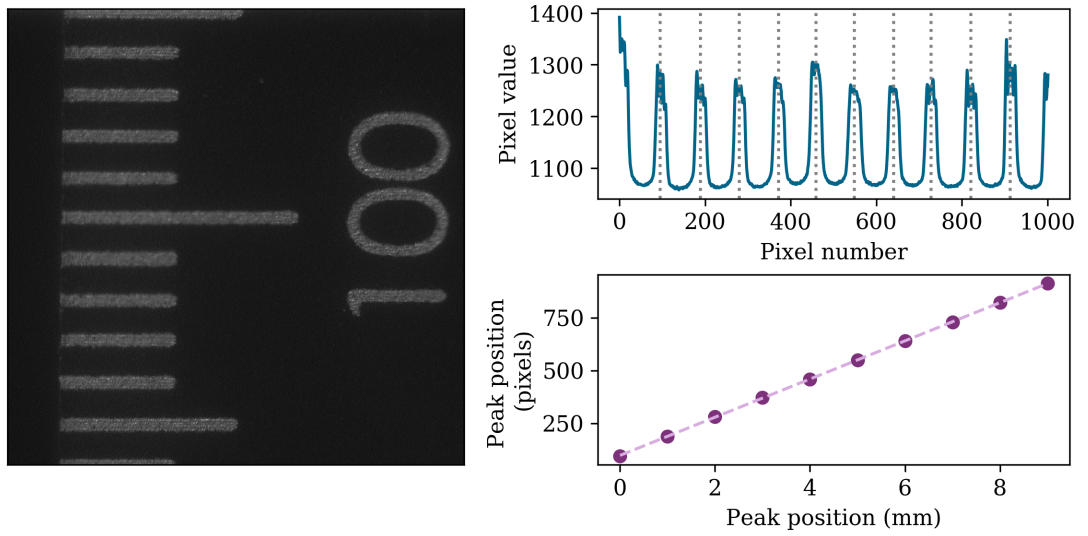
Figure 3.2: **Pixel size calibration.** *Left:* Image of ruler graduations taken with the iXon camera. *Right:* Taking an average of the pixel values horizontally over the central region of interest reveals a series of 'peaks' corresponding to the ruler graduations (upper plot). By looking at the pixel spacing between these peaks and knowing the real distance between them (1 mm) we can fit a straight line (lower plot) and extract a scaling of 90.4 ± 0.2 pixels per mm.

Image Processing

Since the high-speed Photron camera was not optimised for low-light applications, the images presented in this thesis and those used to make the high-speed videos have undergone post-processing to improve clarity and reduce noise. First a background image was subtracted, then the resulting image was binned into 4×4 superpixels. This revealed a periodic grid-like structure which varies between frames and so cannot be removed by subtracting a blank field image. To remove this grid while retaining as much of the image data as possible we perform a spatial Fourier filter to

eliminate the unwanted structure. To do this we perform a 2D fast Fourier transform (FFT) (`numpy.fft.fft2`) on the binned image and manually mask out the features corresponding to the periodic grid structure by setting these regions equal to zero. We then perform the inverse 2D FFT (`numpy.fft.ifft2`) to recover the filtered image. To further improve image clarity we smooth the filtered image using a uniform filter (`scipy.ndimage.uniform_filter`) with `size = 3`. Each frame taken with the Photron was processed in this fashion, including the frames used to make the videos.
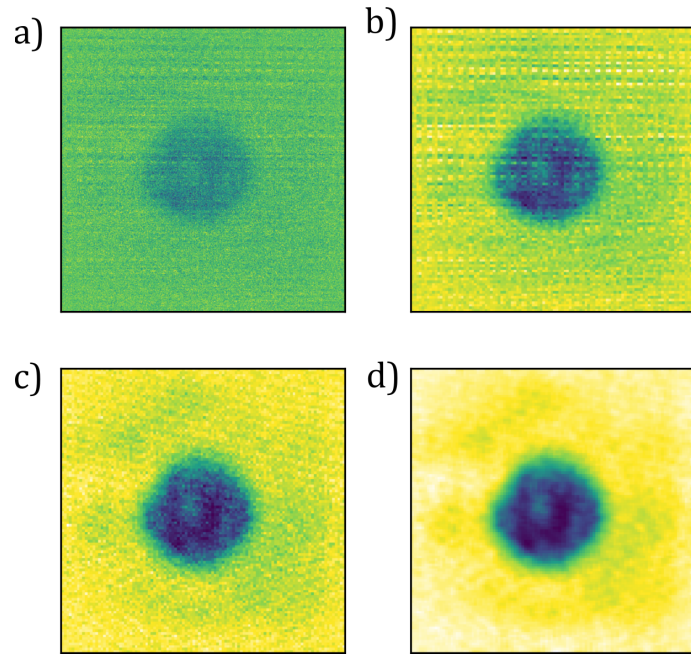
Figure 3.3: **Image processing.** The sequence of steps used to process frames taken with the high-speed Photron camera. (a) The raw camera image with the background subtracted. (b) The resulting image after performing 4×4 binning. The grid-like structure is most apparent here. (c) The result of applying the spatial Fourier filter. The grid-like structure is mostly removed without distorting the image. (d) The final image after applying the uniform filter.

3.5   Experimental Control

Much of the experiment was controlled via computer, allowing measurements to be synchronised and complex sequences to be carried out automatically. This control

was implemented in Python using freely available packages. Custom packages allowed full control of the iXon (`PyAndor` [69]) and the spectrometer (`pyseabreeze` [70]). GPIB control of the microwave source was implemented through VISA (`pyvisa` [71]) allowing the frequency, power and on/off state to be set remotely. For setting the power of the THz field via the UCA we used a multifunction NI USB-6009 data acquisition card controlled using the `nidaqmx` package [72]. This allowed the voltage to the UCA to be set automatically. This method of setting the THz power was preferred over changing the power output of the microwave source as the latter was slow to respond with a measured delay of 80 ms. For this reason when taking data requiring the THz field to be turned on and off rapidly (such as when taking background exposures) the THz field was turned off by setting the attenuation to maximum using the UCA. When a temperature reading of the cell was required this was also automated using an NI USB thermocouple reader and the `nidaqmx` package. For situations that did not require a series of repeat measurements, for example when taking individual images or video sequences, the cameras were triggered directly by the user and not automatically controlled through Python. Control of the iXon was via Micro-Manager [73], allowing a real-time view of the camera output for alignment and focussing. Data was captured from the Photron using the proprietary Photron FASTCAM Viewer software package.

3.6 Bench Layouts

Two different experimental configurations were used in this thesis: one for the electrometry experiments in Chapter 4 and another for the THz imaging experiments in Chapter 6 onwards. The main differences are the shaping of the laser beams, the shape and size of vapour cell used and the method used to collect data from the experiment. Certain aspects of the bench layout are common to both experiments, these are shown in Fig 3.4. In each case a small amount of light from the 852 nm and 1470 nm lasers is split off to be used in the frequency stabilisation. The majority is coupled into single mode polarisation-maintaining fibres and sent to the main experiment. Not only do the fibres allow for easy reconfiguration and realignment
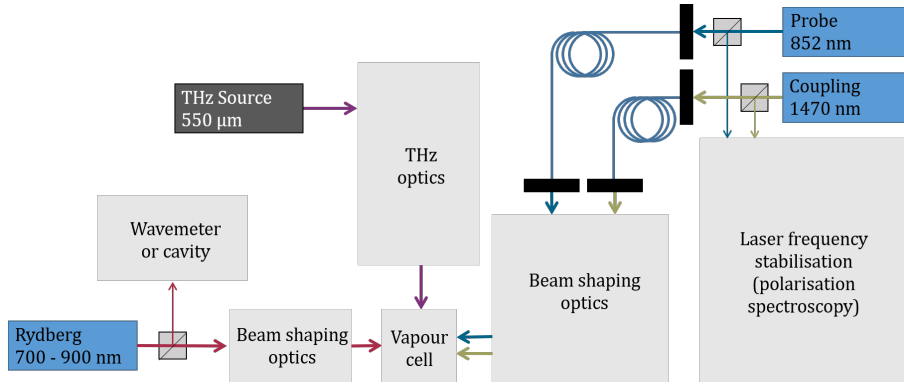
Figure 3.4: **Diagram of the main table layout.** The configuration of three laser sources (blue boxes), THz source (grey box) and the other optical set-ups is shown in a very simplified fashion. This overall layout remains the same for all experiments performed in this thesis.

of the table, they also act as spatial filters to help ensure a pure Gaussian mode. In the case of the Rydberg laser, a small amount of light is picked off to be sent to either a wavemeter to provide a wavelength reading or a cavity with a free spectral range (FSR) of 300 MHz in order to calibrate the scan range of the laser. In both cases the laser beams propagate coaxially through the vapour cell, with the Rydberg laser propagating in the opposite direction to the probe and coupling lasers.

3.6.1 Electrometry

Rydberg electrometry is concerned with using Rydberg atoms to measure a local electric field. To do this, Rydberg atoms are created via the 3-step excitation scheme described earlier, and the transmission spectrum of the probe laser is monitored as the frequency of the Rydberg laser is scanned. When performing the electrometry measurements, all three laser beams were focussed through a vapour cell with an optical path length of 2 mm which was enclosed in an insulating Teflon oven and heated to around 60°C. The probe and coupling lasers were copropagating through the vapour cell with the transmission of the probe laser subsequently monitored on a photodiode. The Rydberg laser and THz field propagated in the opposite direction to the first two lasers. The $1/e^2$ beam waists and powers used are summarised in Table 3.1. It is worth highlighting that the Rydberg laser power was not constant
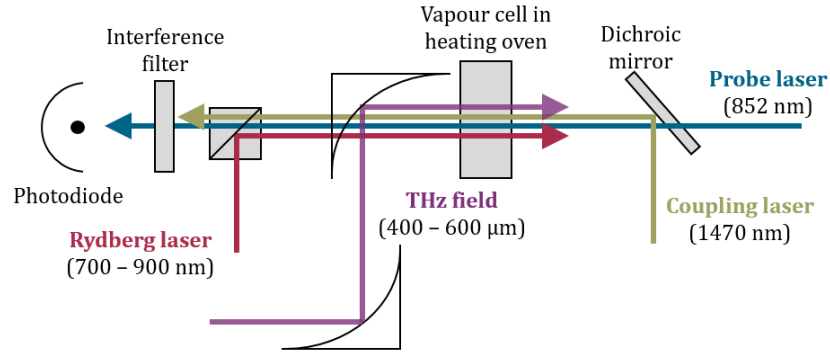
Figure 3.5: **Experimental layout used in the electrometry experiments.** A dichroic mirror is used to overlap the probe and coupling beams before they arrive at the vapour cell. Lenses (not shown) are then used to focus the laser beams into the vapour cell. The THz field is also focussed at the point of the vapour cell using off-axis parabolic mirrors. After passing through the cell, an interference filter blocks the copropagating coupling laser light from reaching the photodiode so that only the probe laser light is detected.

throughout. Due to the varying dipole matrix elements of the different Rydberg transitions the power had to be adjusted to avoid broadening of the signal. The Rydberg laser was scanned across the atomic transition (by about $2\,\mathrm{GHz}$) and the transmission of the probe laser through the vapour was recorded. The Rydberg laser light was also monitored on an external cavity (Coherent, $300\,\mathrm{MHz}$ FSR) to provide a frequency reference for the scan. For the THz beam we use two off-axis parabolic mirrors with focal lengths of $150\,\mathrm{mm}$ to collimate and focus the beam at the position of the vapour cell. In this configuration we estimate that the THz beam has a waist of $0.50\,\mathrm{mm}$ and hence a Rayleigh range of between $1.31\,\mathrm{mm}$ (at $500\,\mathrm{GHz}$) and $1.96\,\mathrm{mm}$ (at $750\,\mathrm{GHz}$) at the position of the cell.

3.6.2 Imaging

In the imaging experiments the quantity of interest is the spatial dependence of the THz field after it has propagated through certain optical elements. When performing the THz imaging experiments described in Chapter 6 onwards, we create a 2D sheet

Laser	Wavelength (nm)	Beam waist at position of vapour cell (µm)	Power into vapour cell (µW)
Probe	852	46	1
Coupling	1470	170	17
Rydberg	700-900	70	>1000

Table 3.1: Beam sizes and powers used in the electrometry measurements, measured at the point of the vapour cell. The beam waist measured is the $1/e^2$ radius of the Gaussian beam. The size of the Rydberg laser waist was measured at $780\,\mathrm{nm}$ and varied slightly with wavelength, however it remained larger than the probe beam waist.

of Rydberg atoms which act as a 2D THz sensor allowing us to capture an image of the incident THz field in a single shot. To do this we use a different vapour cell design and experimental layout to the one used in the electrometry experiments. We use a cuboidal vapour cell manufactured in-house with approximate dimensions of $10\,\mathrm{mm} \times 10\,\mathrm{mm} \times 60\,\mathrm{mm}$, allowing optical access from 4 sides. The cell is still heated but due to the optical access requirements it cannot be entirely encased in an insulating Teflon mount. Instead the lower portion sits in a Teflon mount and is in contact with metal ceramic heaters (Thorlabs HT24S) on two sides. The Cs reservoir sits in a steel heat sink to ensure that it remains the coldest point of the cell to minimise the amount of Cs that condenses on the cell walls. The upper portion of the vapour cell is open to the air, and the temperature of the glass at the very top is monitored using a thermocouple held in place by a Teflon block. The temperature was not actively stabilised, instead the equilibrium temperature of the cell as a function of current through the resistive heaters was measured and used as a reference to set the approximate cell temperature. In normal operating conditions this method of applying a constant current led to small temperature variations (on the order of $2\,°\mathrm{C}$) over a period of several minutes. When a more stable temperature was required (for instance when studying the vapour fluorescence as a function of temperature in Chapter 5) a cardboard enclosure was placed around the cell to reduce air currents and help minimise temperature fluctuations while still allowing
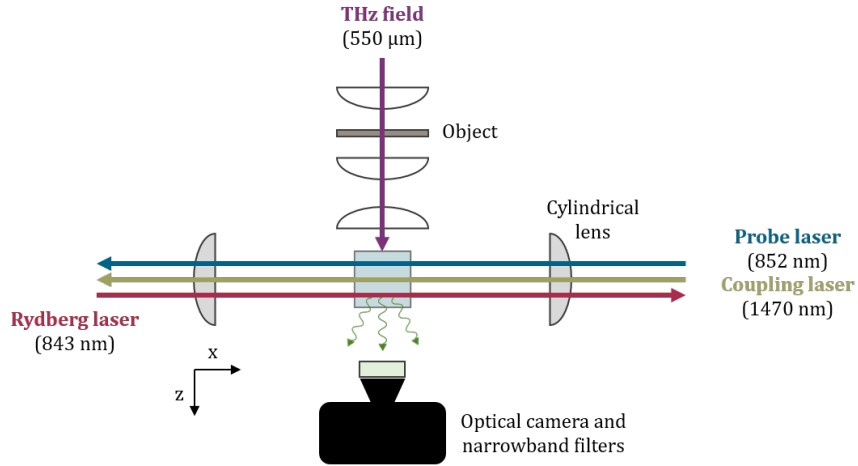
Figure 3.6: **Experimental layout of the THz imaging experiment.** In contrast to the electrometry experiments, the THz field now propagates perpendicular to the laser beams and is shaped using Teflon lenses. The laser beams pass through cylindrical lenses to form a light sheet at the position of the vapour cell. An optical camera is used to image fluorescence emitted by this light sheet from the opposite direction to the incident THz field.

optical access. In order to create a 2D sheet of excited atoms we expand all 3 laser beams in the y direction using cylindrical telescopes, and then focus in the z axis at the position of the vapour cell using a final cylindrical lens. At the position of the cell the overlapping beams form a light sheet with dimensions of approximately $10\,\text{mm} \times 10\,\text{mm} \times 100\,\mu\text{m}$. The final focusing cylindrical lenses are chosen to have long focal lengths ($300\,\text{mm}$) to ensure that the Rayleigh range of the light sheet is longer than the propagation distance through the vapour cell. This should ensure that the laser intensity remains relatively constant across the vapour cell, leading to a more uniform image. Due to the increased beam size, the laser powers required were larger than those used in the electrometry experiments. The probe and coupling laser powers used were $15\,\text{mW}$ and $20\,\text{mW}$ respectively, while the Rydberg laser power was around $50\,\text{mW}$. To form an image on the sheet of atoms the THz field propagates along the z axis and is incident on the vapour cell normal to the sheet of excited atoms. For ease of alignment we use Teflon lenses to collimate and focus the THz field instead of the parabolic mirrors used previously. A single lens of focal
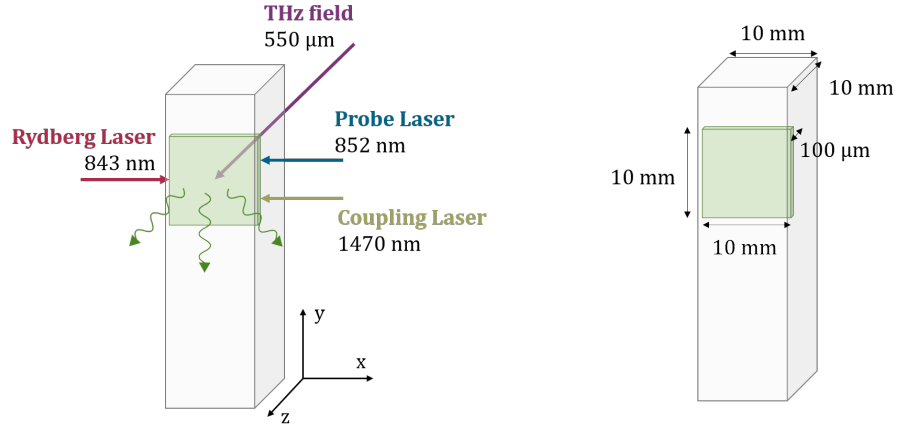
Figure 3.7: **Diagram of the custom vapour cell used in the imaging experiments.** *Left:* The probe and coupling lasers (blue and green arrows) counterpropagate with the Rydberg laser (red arrow) along the x axis to form a light sheet (green shaded region) while the THz field (purple arrow) is incident along the y axis. The fluorescence (green arrows) is imaged from the front of the cell. *Right:* The dimensions of the custom cuboidal vapour cell used, including the dimensions of the light sheet formed by the overlapping laser beams.

length 75 mm is used to collimate the THz beam and provide uniform illumination of the target object. In this case the beam will have a radius of 11.1 mm (FWHM of 13.1 mm) at the position of this first lens. Two further lenses are then arranged to project a 1:1 image of the transmitted field onto the vapour. In this configuration the beam shape at the first lens is the same as the beam shape at the position of the light sheet. The fluorescence from the vapour is then imaged from the opposite side to the incident THz field.

3.7 Conclusion

In this chapter we described experimental techniques and details that will provide the basis for all of the work in this thesis. We described details of the layouts and components of the experiments and outlined the procedures used to capture data. While some elements such as the laser frequency stabilisation are common to both the electrometry and the imaging experiments, there are important differences in

the experimental configurations used to perform these different experiments.

Chapter 4

THz Electrometry Using Rydberg Atoms

In this chapter we use the fact that applying a resonant THz field to Cs Rydberg atoms causes Autler-Townes (AT) splitting which can be seen in the transmission signal of the probe laser. We use this splitting to measure the Rabi frequency of the applied THz field and hence the power output of the THz source. We perform these measurements in a wide frequency range, from $450\,\text{GHz}$ to $800\,\text{GHz}$. We also use this frequency-dependent splitting to measure values for some of the quantum defects in Cs, improving on those currently used in `ARC` [14].

4.1   Introduction

Rydberg atoms are highly sensitive to external electric fields, as their polarisability scales as n^7 [13]. This property can be exploited to measure weak DC electric fields by looking at the DC Stark shift of Rydberg states in the presence of an applied field [74–76]. Rydberg atoms can be exploited to measure the field strength of resonant EM fields through the AC Stark effect, which causes Autler-Townes splitting of the Rydberg state [58]. This Rydberg electrometry technique has previously been used to detect weak resonant radio [15, 77], microwave [16, 17] and THz frequency [18] fields. Although this relies on there being an atomic transition at the frequency of interest, the large number of atomic transitions available enables this technique

to be used over a wide frequency range. The fact that atomic properties are well-known and traceable to SI units means that these detectors are in some respects 'self-calibrating'. Devices employing Rydberg atoms have in recent years been used to receive radio communications [78, 79] and to record music in 'real-time' [80]. Performing such experiments in thermal vapour cells allows devices to be made compact and portable [81], hence leading to their commercialisation [11, 12].

In this chapter we use our Cs Rydberg system to measure the power of the THz field from our THz source as a function of frequency. This information will be important later when we come to select optimum parameters for our THz imaging experiments. We find that our measurements are similar to those performed previously using different methods for the same THz source [82]. We also find differences between the measured and theoretical values for some atomic transition frequencies leading us to calculate new values of the quantum defects in Cs. This is the first example of Cs quantum defects measured in an atomic vapour cell experiment, and is the first comprehensive measurement of Cs quantum defects that does not rely on data from other sources.

4.2 Principle of Rydberg Electrometry

In Chapter 2 we set up the optical Bloch equations to describe a 3-level ladder system, and discussed how to include the effects of the varying Doppler shift across different atomic velocity classes. These equations can be extended to describe the 5-level atomic system used in the experiments described in this chapter. By solving these equations for some typical experimental parameters we see that in the presence of the 3 laser fields (but in the absence of the THz field) our probe transmission spectrum as a function of Rydberg laser detuning exhibits a peak, as in the left-hand plot of Figure 4.1. We refer to this as our 'Rydberg signal' as it is a consequence of population being transferred to the Rydberg state. This signal has an approximately Lorentzian shape as shown by the dashed line in Figure 4.1, the width of which is defined by the Rydberg laser power. When a THz field is applied that is resonant with a transition to another Rydberg state, Autler-Townes splitting causes this

single peak to become a double peak, the separation of which is equal to the Rabi frequency of the applied THz field, Ω_{THz}. This is shown in the central and right-hand columns of Figure 4.1 for THz Rabi frequencies of $\Omega_{\text{THz}} = \{10, 20\} \times 2\pi$ MHz respectively.
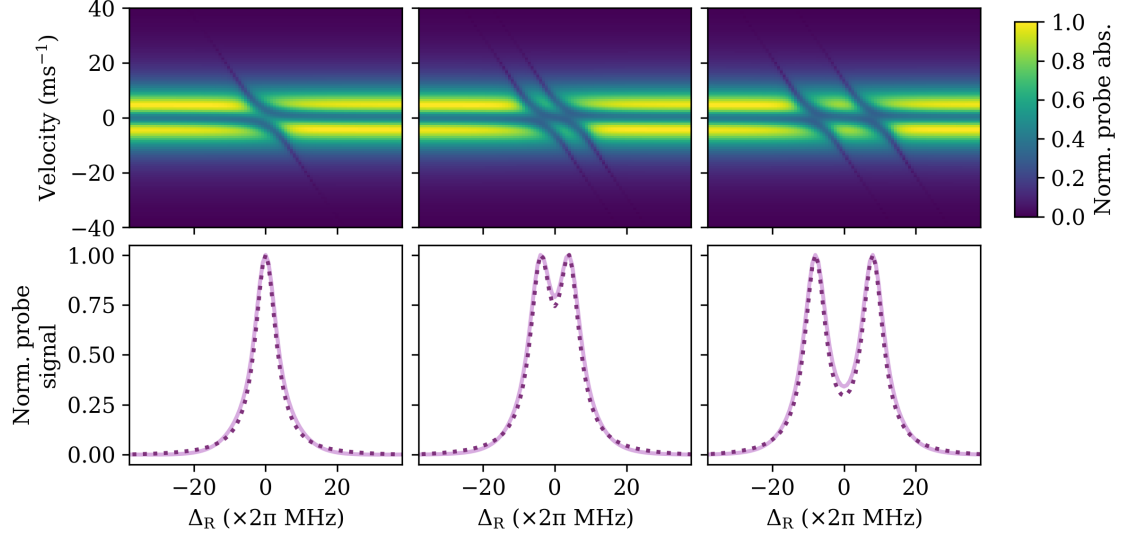
Figure 4.1: **Simulated results demonstrating the effect of an applied THz field on the probe transmission signal.** Results of numerically solving the optical Bloch equations for a 5-level ladder system with different THz Rabi frequencies. The top plots show the normalised absorption of the probe laser as a function of the Rydberg laser detuning (Δ_{R}) for a range of atomic velocity classes. The lower plots show the ensemble averaged probe transmission signals (light purple solid lines) and the sum of two Lorentzians separated by Ω_{THz} (purple dotted lines). From left to right, $\Omega_{\text{THz}} = \{0, 10, 20\} \times 2\pi$ MHz. The simulation parameters were $\Omega_{\text{p,c,R}} = 10 \times 2\pi$ MHz, $\Gamma_2 = 6 \times 2\pi$ MHz, $\Gamma_3 = 1 \times 2\pi$ MHz, $\Gamma_{4,5} = 0.05 \times 2\pi$ MHz for a 30°C vapour.

The amplitude of the THz electric field $|E_{\text{THz}}|$ can then be found from this measured value of Ω_{THz} and the calculated dipole matrix elements $\mathbf{d}_{54}$ for the transitions through

$$|E_{\text{THz}}| = \frac{\hbar \Omega_{\text{THz}}}{\mathbf{d}_{54}}. \tag{4.2.1}$$

We can then use this to compare the power output P_{THz} of the source at different

frequencies, since

$$P_{\text{THz}} \propto |E_{\text{THz}}|^2. \tag{4.2.2}$$

In Chapter 2 we detailed the method of calculating the dipole matrix elements for atomic transitions and showed that they depend on the initial and final values of m_j involved in the transition. In our excitation scheme we use linearly polarised light to excite atoms from the $6S_{1/2}$ state so we assume that only the $m_j = \pm 1/2$ states are populated. Since the THz field is colinear and also linearly polarised we assume it can only drive π transitions, so we only consider the dipole matrix elements relating to the $m_j = \pm 1/2 \to m'_j = \pm 1/2$ transitions on the final step [83]. In the case where the polarisation of the THz field is not matched to that of the laser fields we would expect to see an additional feature in the centre of the two peaks [84]. Since we do not see such a feature we assume our polarisation is well matched and we are justified in using the dipole matrix element for $m_j = \pm 1/2 \to m'_j = \pm 1/2$ transitions in the calculation of the E-field.

4.3   THz Power Measurements

The power output of the THz source is highly frequency dependent. In order to measure its power output we identify transitions between Rydberg states that lie within the frequency range of the THz source (450 GHz to 800 GHz), and select 94 that are approximately evenly spaced in this region. For each of these transitions we record the probe transmission as we scan the Rydberg laser, both with and without the THz field. We then measure the width of the splitting caused by the THz field by fitting two Lorentzians to the signal and extracting their separation. An example of this fitting is shown in Figure 4.2 for the $29P_{1/2} \to 28S_{1/2}$ transition at 639 GHz. This splitting is equal to the THz Rabi frequency, Ω_{THz}, which here is found to be 11.33 ± 0.08 MHz. The uncertainty in the splitting and hence the uncertainty in Ω_{THz} is the standard error in the 3 repeat measurements of the splitting from 3 different recorded probe traces.

The results of these measurements of the THz source power are shown in Fig-
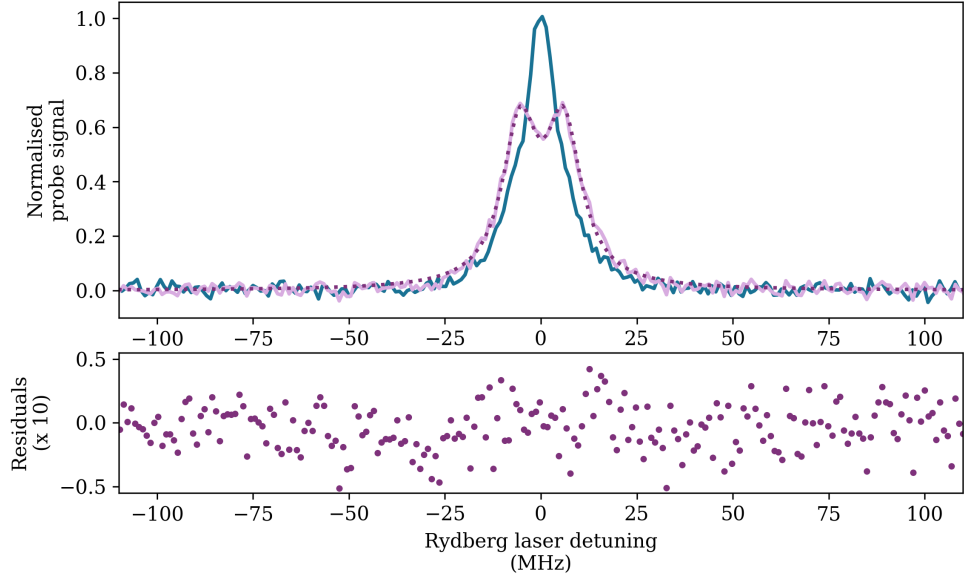
Figure 4.2: **Example of signals obtained in Rydberg electrometry.** *Top:* The Rydberg signal in the absence of the THz field (blue line) is split into a double peak (light purple line) when a resonant THz field is applied. We fit a sum of two equal Lorentzians to measure the splitting (purple dotted line). The data shown here is for the $29P_{1/2} \rightarrow 28S_{1/2}$ transition at $639\,\mathrm{GHz}$. The fit gives a splitting and hence a THz Rabi frequency of $11.33 \pm 0.08\,\mathrm{MHz}$. Note that the signals are normalised such that the height of the peak in the absence of the THz field is unity. *Bottom:* The residuals show no structure so we conclude that the double Lorentzian model is a good fit to the data in the presence of the THz field.

ure 4.3. The errorbars on the datapoints are calculated as

$$\alpha_{P_{\mathrm{THz}}} = \frac{2E_{\mathrm{THz}}\alpha_{\Omega_{\mathrm{THz}}}}{\mathbf{d}_{54}} \qquad (4.3.3)$$

where $\alpha_{\Omega_{\mathrm{THz}}}$ is the standard error on the 3 repeated measurements of the THz splitting. For some of the transitions investigated, no splitting of the Rydberg signal by the THz field was observed by eye but fitting two Lorentzians returned a non-zero separation. To determine whether the splitting measured by the fit was genuine, we fit the sum of two Lorentzians to the Rydberg signal in the absence of the THz field, and look at the measured peak separation. If this splitting was larger than that measured in the presence of the THz field we discount these datapoints as

the measured effect of the THz is anomalous. We plot our measured THz power as a function of frequency in Figure 4.3. There is no obvious trend in power output by the source as a function of frequency, however our measurements do agree somewhat with previous measurements taken by the group of M. Tarbutt at Imperial College (blue dotted line, Fig. 4.3) and measurements taken by the manufacturer Virginia Diodes (green dashed line, Fig. 4.3) of the power output of this particular source [82]. However since we have no details of how these other measurements were taken it is difficult to make more quantitative comparisons. Also we note that while our measurements give an indication of the relative power at different THz frequencies, relating these values to an absolute power would have required knowledge of the beam sizes and overlap at the point of the atoms. Since this is difficult to measure precisely, especially in the case of the THz field, we simply scale our measurements by a constant factor such that the peak of our measured 'powers' is consistent with that of the manufacturer's measurements.

4.4   Quantum Defect Corrections

For a resonant applied THz field we expect the Rydberg signal to be split into two peaks of equal heights, as demonstrated in Figure 4.1. In taking the data presented in this chapter, some of the calculated transition frequencies resulted in asymmetric splitting of the Rydberg signal, indicating that the applied THz field was detuned from resonance. In these cases the THz frequency was varied until symmetric splitting of the line was achieved. Figure 4.4 shows the change in the Rydberg signal as we vary the detuning of the THz field. For small values of THz detuning ($< 50\,\mathrm{MHz}$) the heights of the two Autler-Townes peaks vary linearly as a function of THz detuning. We can then fit straight lines to the peak heights and determine the resonant transition frequency by finding the crossing point, as shown by the black dashed line in Figure 4.4. Using this method we are able to determine the resonant frequency to within $\pm 0.5\,\mathrm{MHz}$. We were able to make a good estimate of the resonant THz transition frequency by simply looking at the signal and varying the THz frequency in real time until the peak heights appeared equal. This method
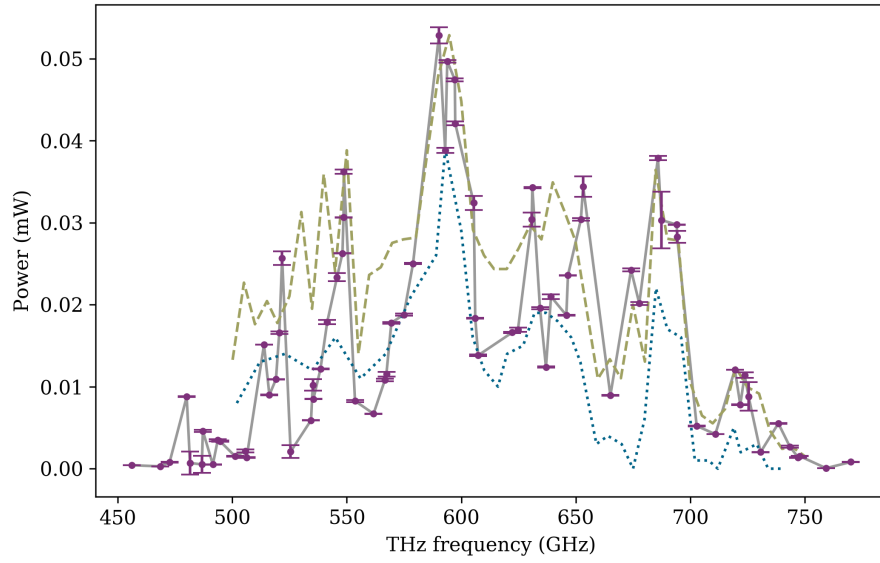
Figure 4.3: **THz source power measurements using Rydberg electrometry.**
The purple datapoints are the powers measured using the electrometry technique.
The blue dotted line is the data taken at Imperial College, and the green dashed
line is data taken from the user manual of the THz source [82]. Note that the
electrometry measurements have been scaled such that the peak power output is
equal to that measured by the manufacturer. The grey solid line is added between
the electrometry datapoints as a guide to the eye.

allowed us to measure the resonant frequency to a precision of $\pm 3\,\text{MHz}$ and is taken to be the error on our measured frequency values.

This resonant transition frequency was recorded and compared to the theoretical transition frequency as calculated by `ARC` [14]. For each transition we plot the difference between these calculated and measured frequencies against the principal quantum number of the initial state, n_1, as in the upper plot in Figure 4.5. From this figure we see two regimes; one in which the frequency difference is small ($<$ $10\,\text{MHz}$) and does not depend on n_1, and a second in which the frequency difference is significant (between $20\,\text{MHz}$ and $80\,\text{MHz}$) and decreases for larger n_1. The shape and colour of the points in Figure 4.5 indicate the initial and final states in the transition. The shape identifies the initial state (circles indicate transitions from a $P_{1/2}$ state, stars represent those from $P_{3/2}$) while the final state in the transition determines the colour (blue for transitions to $S_{1/2}$ states, light and dark purple for transitions to $D_{3/2}$ and $D_{5/2}$ respectively). We find that these two regimes are defined by the value of j_1; transitions with $j_1 = 1/2$ were more accurate than those with $j_1 = 3/2$ with the latter showing a dependence on n_1. In all cases, whether this frequency difference was positive or negative depended on the 'direction' of the transition (whether the initial state was higher or lower in energy than the final state). Note that any transitions for which no effect of the THz field was detected have not been used in this dataset as it was impossible to determine the resonant THz frequency. The fact that there is no correlation with THz frequency (lower plot, Fig. 4.5) indicates that this difference is unlikely to be due to a systematic frequency offset in our applied THz field. The discrepancy also increases with decreasing n_1 suggesting that it is unlikely to be caused by stray electric fields. Since any DC Stark effect would affect transitions involving higher n more strongly we would expect the difference to increase with increasing n_1 if caused by a stray E-field.

To understand the origin of this discrepancy we must first understand the method used by the `ARC` package to calculate the transition frequencies. In order to calculate the frequency (or wavelength) of a given transition, `ARC` first calculates the energy of each state using equation 2.1.6. The frequency of the transition ω_0 is then related
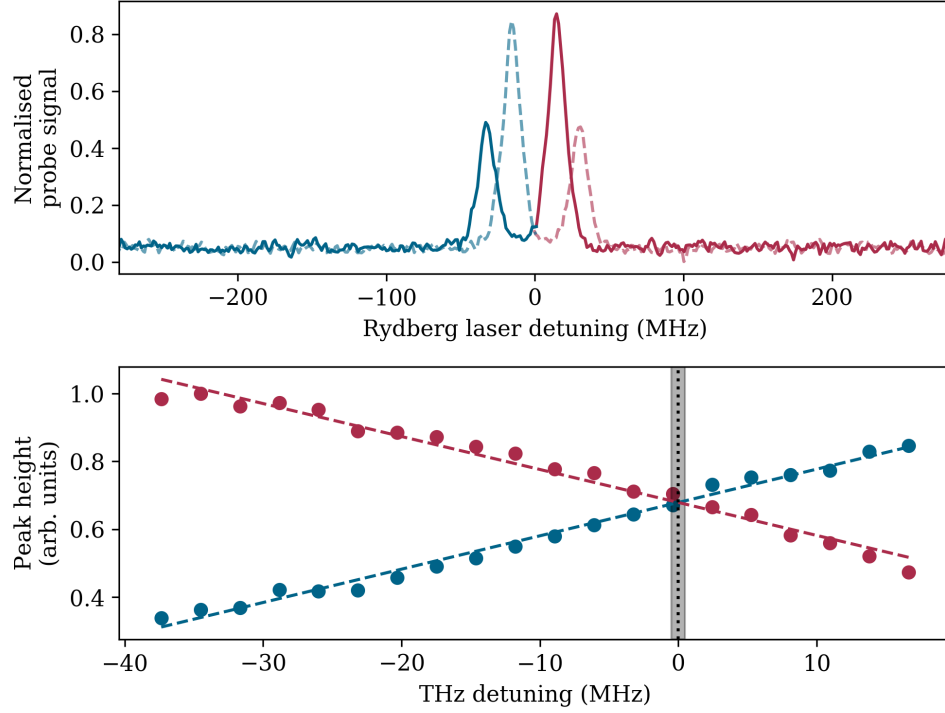
Figure 4.4: **Dependence of lineshape on THz detuning.** *Top:* Examples of the Rydberg signal with an applied THz field that is approximately 17 MHz above (solid line) and below (dashed line) resonance. When the THz field is resonant with the centre of the transition we expect the height of the two Autler-Townes peaks to be equal, when the THz field is detuned we see clear asymmetry in the peaks. Note that in both cases the signals are normalised such that the peak height in the absence of the THz field is unity. *Bottom:* We measure the height of the left-hand (blue) and right-hand peak (red) and plot them as a function of THz detuning. By fitting straight lines to these points we can find the resonant transition frequency as the point at which the lines intersect to within 0.5 MHz. In this example we measure the resonant frequency of the $21P_{1/2} \rightarrow 22S_{1/2}$ transition to be 646.5794 ± 0.0005 GHz, indicated by the vertical dotted line.
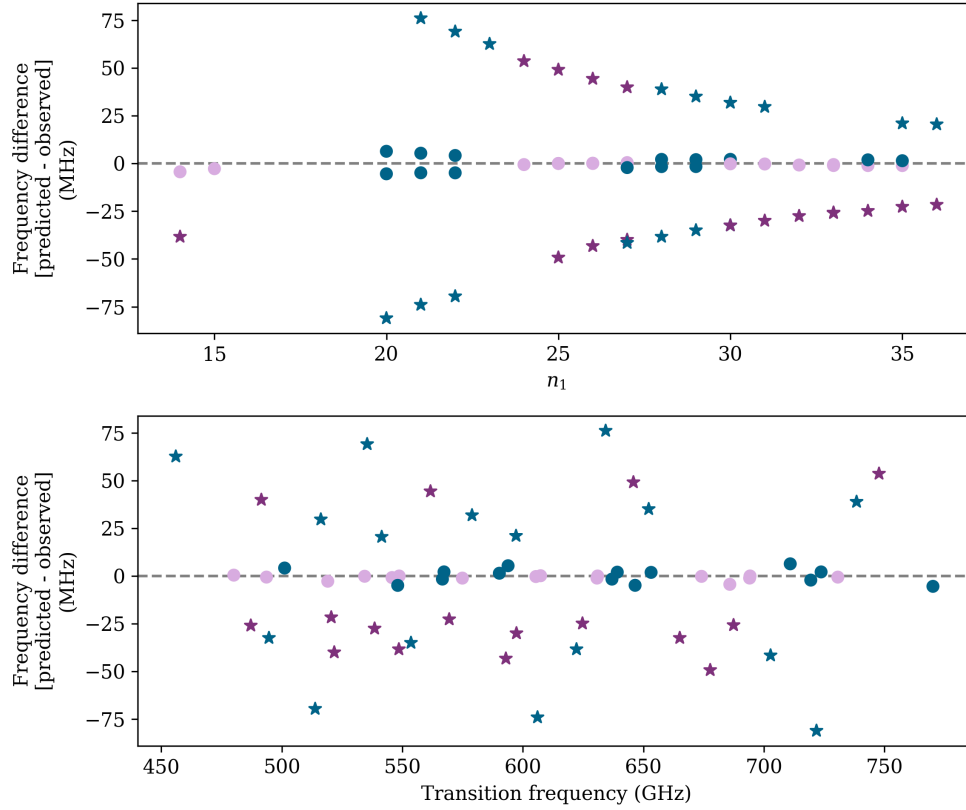
Figure 4.5: **Difference between calculated and measured THz transition frequencies.** Calculated minus observed transition frequencies for a range of THz transitions as a function of n_1 (*top*) and transition frequency (*bottom*). The shape identifies the initial state (circles indicate transitions from a $P_{1/2}$ state, stars represent those from $P_{3/2}$) while the final state in the transition determines the colour (blue for transitions to $S_{1/2}$ states, light and dark purple for transitions to $D_{3/2}$ and $D_{5/2}$ respectively). For transitions from $P_{1/2}$ (circles) there is little discrepancy between theory and experimentally measured frequency, and no dependence on n_1. For transitions from $P_{3/2}$ (stars) there is a greater discrepancy that increases as n_1 decreases. There is very little correlation with the final state of the transition (colour of the points).

to the energy difference through

$$\omega_0 = \frac{e}{h} \left(E_2 - E_1 \right) \tag{4.4.4}$$

$$= ecR_\infty \left(\frac{1}{(n_1 - \delta_{l_1,j_1}(n_1))^2} - \frac{1}{(n_2 - \delta_{l_2,j_2}(n_2))^2} \right). \tag{4.4.5}$$

where $\delta_{l,j}(n)$ is the quantum defect which can be parametrised as

$$\delta_{l,j}(n) = \delta_0 + \frac{\delta_2}{(n-\delta_0)^2} + \frac{\delta_4}{(n-\delta_0)^4} + \frac{\delta_6}{(n-\delta_0)^6} + \dots \tag{4.4.6}$$

where the values for $\delta_{0,2,4,\dots}$ are distinct for different values of l and j. Due to the dependence of the quantum defect on n, any inaccuracies are more evident at lower principal quantum numbers. We can see from these equations that the most likely source of this discrepancy is in the values of the quantum defects used within `ARC`. These are not calculated but are instead taken from values reported in literature.

The most recent and commonly used measurements of the quantum defects in Cs were made in 1987 by Weber & Sansonetti [85]. They only directly measure values for the quantum defects of the $n\mathrm{S}_{1/2}$, $n\mathrm{P}_{1/2}$ and $n\mathrm{D}_{5/2}$ states, and reference data from Goy et al. [86] for calculation of the $n\mathrm{D}_{3/2}$ quantum defects, and data from Sansonetti & Lorenzen [87] for calculation of the $n\mathrm{P}_{3/2}$ quantum defects. The most recent direct measurements of the quantum defects of the $n\mathrm{P}_{3/2}$ and $n\mathrm{D}_{3/2}$ states in Cs were made by Lorenzen & Niemax in 1984 [88]. This means that there is no single reference for accurate values of the quantum defects for all of the values of l and j up to $n\mathrm{D}_{5/2}$. The values used by `ARC` are taken from [85] for the $n\mathrm{S}_{1/2}$, $n\mathrm{P}_{1/2}$ and $n\mathrm{D}_{5/2}$ states, and from [88] for the $n\mathrm{P}_{3/2}$ and $n\mathrm{D}_{3/2}$ states.

We use our measured transition frequencies to extract measurements of the quantum defects in Cs without relying on any data from other sources. Usually the way to do this is to consider 2-photon transitions between states with the same value of l and j, thereby having only one quantum defect as a variable in the fitting at a time [86, 89]. We can apply this method to our data by considering pairs of transitions that have a single state in common. For example the $22\mathrm{P}_{3/2} \rightarrow 22\mathrm{S}_{1/2}$ and the $22\mathrm{P}_{3/2} \rightarrow 23\mathrm{S}_{1/2}$ transitions have the same initial state and are both to an $\mathrm{S}_{1/2}$ state, meaning they could be used to calculate the frequency of the $22\mathrm{S}_{1/2} \rightarrow 23\mathrm{S}_{1/2}$ transition. However choosing transitions that fulfil this criteria reduces our useable

data considerably and since it means that for some quantum defects we have only 3 points with which to perform a fit, it was decided that this was not the optimum method here. For further details and discussion about the drawbacks of applying this method to our data, see Appendix B. Instead we take a more 'brute force' approach, and optimise the values of all of the quantum defects simultaneously. We use equations 4.4.5 and 4.4.6 as a theoretical model to predict the transition frequencies. We then vary the values of $\delta_{0,2,4}$ to minimise the difference between the predicted and measured transition frequencies. To do this we use a least-squares minimisation built into the Python `curvefit` package. Table 4.1 shows a comparison of our optimised values of the coefficients from equation 4.4.6 to those from the above literature sources. Although the values of the quantum defects for the $n\mathrm{P}_{3/2}$ and $n\mathrm{D}_{3/2}$ series are not directly quoted in [85], the authors note that these values can be extracted using the measured fine structure intervals from other literature sources ([86] for the P intervals and [87] for the D intervals). Details of the method used to extract values of the quantum defects from these fine structure intervals can be found in Appendix B. Values calculated in this way are indicated by (*) in Table 4.1.

We find that our values for the coefficients $\delta_{0,2,4}$ mostly agree with the values reported in [85] within error, but in contrast to the work presented in [85] our measurements do not rely on data from any other sources. The difference between the transition frequencies calculated using the values in Table 4.1 and our measured frequencies are shown in Figure 4.6. As in Figure 4.5 the shape of the points identifies the initial state (circles indicate transitions from a $\mathrm{P}_{1/2}$ state, stars represent those from $\mathrm{P}_{3/2}$) while the final state in the transition determines the colour (blue for transitions to $\mathrm{S}_{1/2}$ states, light and dark purple for transitions to $\mathrm{D}_{3/2}$ and $\mathrm{D}_{5/2}$ respectively). In the upper plots there is clearly structure in the differences between the calculated and measured frequencies, and the frequencies for certain low-n transitions differ by hundreds of MHz (or tens of GHz in the first plot). In contrast the lower plot showing the frequency differences using our optimised values for the quantum defects exhibits no clear structure.

		Goy et al. [86]	Lorenzen & Niemax [88]	Weber & Sansonetti [85]	This work
	δ_0	4.049325(15)	4.049353	4.04935665(38)	4.049356(5)
$S_{1/2}$	δ_2	0.246(5)	0.2381	0.237704	0.2381(11)
	δ_4	n/a	0.24688	0.255401	0.01(14)
	δ_0	3.59156(3)	3.591486	3.59158950(58)	3.591596(7)
$P_{1/2}$	δ_2	0.371(4)	0.380223	0.360926	0.360(3)
	δ_4	n/a	-0.64771	0.41905	0.4(5)
	δ_0	3.55906(3)	3.55896	3.5590713(2)*	3.559078(6)
$P_{3/2}$	δ_2	0.374(4)	0.392469	0.37306(7)*	0.371(2)
	δ_4	n/a	-0.67431	0.405(4)*	0.4(4)
	δ_0	2.47536(2)	2.475456	2.4754682(3)*	2.475462(7)
$D_{3/2}$	δ_2	0.555(6)	0.00932	0.004367(4)*	0.008(4)
	δ_4	n/a	-0.43498	-0.343(1)*	$-0.5(6)$
	δ_0	2.466210(15)	2.466309	2.46631524(63)	2.466305(8)
$D_{5/2}$	δ_2	0.067(5)	0.014964	0.013577	0.021(3)
	δ_4	n/a	-0.45828	-0.37457	$-1.3(4)$

Table 4.1: **Comparisons of the values of the quantum defects in Cs.** The values of the coefficients used to calculate the quantum defect (as in equation 4.4.6) given in various literature sources and those measured in this work. Uncertainties are reproduced from literature where available. The quoted uncertainties in our measurements are the 1σ standard errors obtained from the fitting algorithm used. Values indicated by (*) are calculated using fine structure interval data as outlined in Appendix B.

4.5 Conclusion

In this chapter we used Rydberg electrometry across a wide frequency range (450 GHz - 800 GHz) to measure the power output of our THz source as a function of frequency. These measurements were compared to previous data and found to have similar structure, but with some discrepancies. It would be helpful to identify more transitions located at points of greatest discrepancy and take more measurements to establish the origin of this difference. As we are unsure as to the methods used to collect the previous data, we cannot draw too many comparisons between the outcomes.

We also used the Autler-Townes splitting of the Rydberg signal by an applied THz field to establish the resonant frequency of the THz transition. We found that in some cases the measured frequency differed from that predicted by `ARC` by up to 80 MHz. This difference was hypothesised to arise from inaccuracies in the values of the quantum defects used in the calculation of the transition frequencies. We were able to use this model to extract new values of the quantum defects in Cs and found that these values reproduce our measurements more accurately. To further investigate the validity of these new measurements it would be useful to see how well they reproduce values of other measured transition frequencies. However this would require extensive literature searches and compiling of data, and is beyond the discussion presented here. These measurements of the quantum defects represent the only complete set of measurements that do not rely on any other sources of data. They are also the only example of quantum defects measured using THz frequency fields.
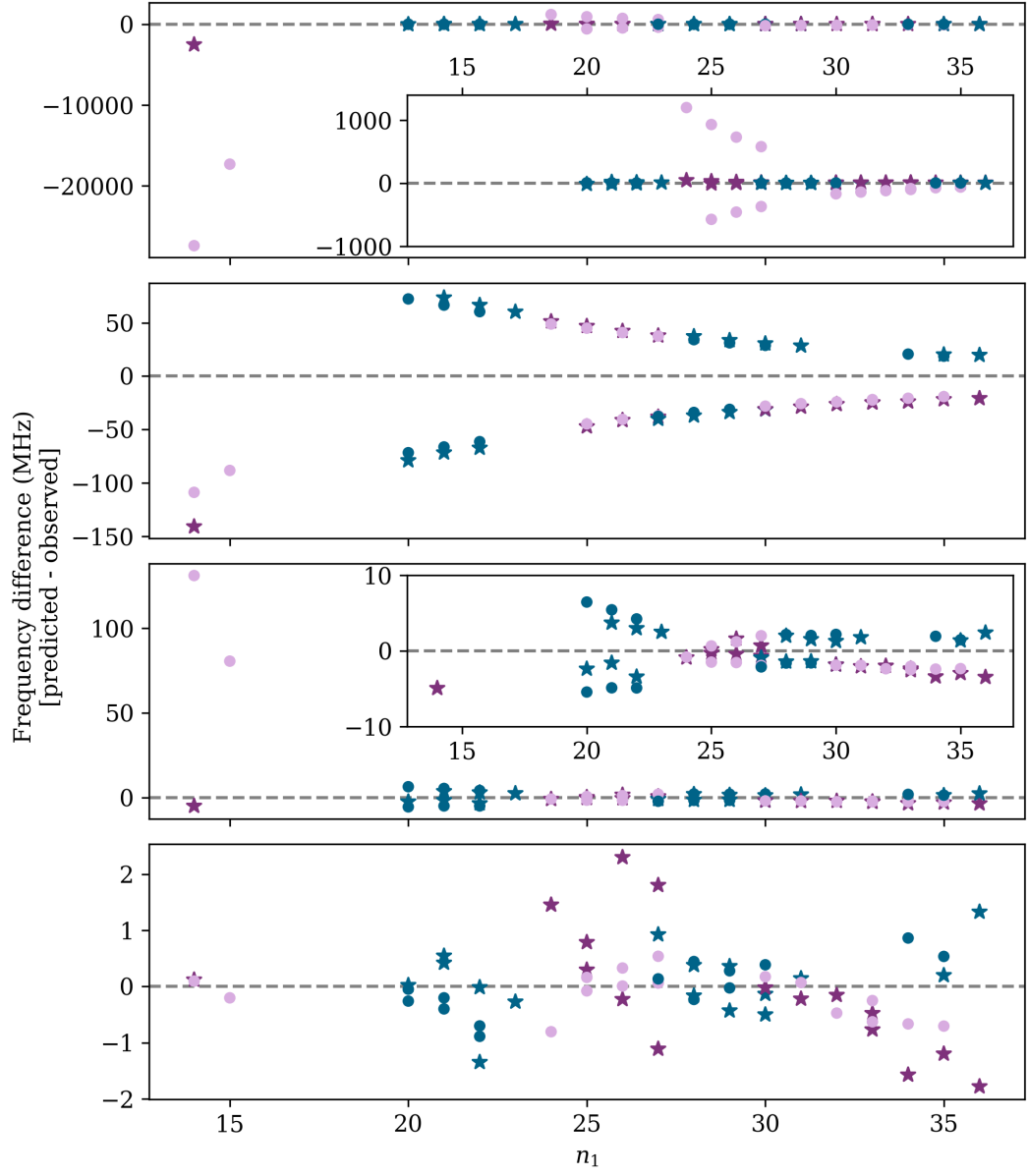
Figure 4.6: **Comparison of different quantum defect values.** Plots of the difference between our measured transition frequencies and those calculated using quantum defect values from the literature sources given in Table 4.1. From top to bottom: Goy et al. [86], Lorenzen & Niemax [88], Weber & Sansonetti [85], the values of the quantum defects measured in this work. As in Fig. 4.5, the colours/shapes of the points correspond to the initial/final states in the transition. Note the changing scale of the y axes.

Chapter 5

Rydberg Fluorescence

In this chapter, we look in detail at the radiative decay processes in a thermal Rydberg vapour and how this informs our choice of states for atom-based THz imaging. We present high-resolution fluorescence spectra from a gas of thermal Cs atoms excited to Rydberg states via resonant driving. We describe a simple model for simulating the spectral emission of a thermal Rydberg vapour and show that it agrees with measured spectra for two Rydberg states coupled by a THz field. This model enables us to better understand the dynamics of the system by providing information on which atomic transitions lead to strong emission. We also discuss features of the measured fluorescence spectra that are not replicated by the model. We investigate the temperature dependence of the emitted fluorescence in the presence of the THz field, and the effects of varying the THz detuning. Again we discuss features that are not able to be simulated by the simple model.

5.1 Introduction

In the previous chapter we used the principle of Rydberg electrometry to measure the field strength of an applied THz field. To model this process we could use the optical Bloch equations to predict the transmission of one of the driving fields and use this to understand the behaviour of the atoms. Unfortunately this approach gives little insight into the photons emitted by the atoms and does not take into account the probabilistic nature of emission processes. Observing the properties of the photons

emitted through spontaneous decay can provide insight into the dynamics of the atomic system. For example, emitted fluorescence can be used to observe optical bistability [90,91] and study phase transitions [18,92,93]. Measuring the statistics of emitted fluorescence is also vital in the verification of Rydberg atom single-photon sources [94,95].

Previous work has shown that Rydberg atoms can be used to image the spatial distribution of an applied THz field through the observation of optical fluorescence [51]. Atoms excited to a Rydberg state using IR lasers, as described in Chapter 3, can decay by emitting photons at visible wavelengths. Since the branching ratios and selection rules differ between Rydberg states, the wavelength of the emitted photons can be used as an indication of the population in a particular state. In this previous work a two-photon Raman transition was used to transfer atomic population into a final THz-coupled Rydberg state without populating an intermediate Rydberg state. In this case fluorescence is only emitted from regions where the THz field is present, thus all of the collected fluorescence can be interpreted as an image of the THz field. One drawback of using a Raman transition in which both the final excitation laser and the THz field are detuned by hundreds of MHz is that the efficiency of the population transfer to the THz coupled state is vastly reduced, meaning higher laser and THz powers are required than in the case of resonant excitation.

In order to minimise the laser and THz power requirements for a full 2D THz imaging system we consider a scheme that uses resonant driving fields to address atomic transitions, meaning that two Rydberg states are populated during the process. While this allows for a greater population transfer to the final Rydberg state, both Rydberg states decay by emitting visible fluorescence so the ability to distinguish between the fluorescence from nearby Rydberg states becomes important. In order to select the best pair of Rydberg states for THz imaging from the hundreds of available transitions we need to be able to predict the fluorescence spectrum from any given Rydberg state with reasonable accuracy.

In this chapter we first describe a simple model for simulating the fluorescence emitted from a Rydberg atom vapour, and show that this model replicates many of the features seen in measured spectra. We also look at possible explanations for

differences between the results of the model and the measured spectra. We then describe how this model can be used to predict the optimum states for use in an atom-based THz imaging system. We go on to look in detail at the behaviour of the spectral emission with varying temperature and THz detuning, and highlight some interesting features that are not predicted by the simple model.

5.2   Modelling Fluorescence Spectra

When considering the coherent dynamics of an atom-light system we can make use of the optical Bloch equations as outlined in Chapter 2 and solve them numerically to predict the response of the system. However in order to predict the fluorescence emitted by a gas of Rydberg atoms we need to consider the probabilistic nature of the decay processes within the atom. In the absence of blackbody radiation (i.e. at $0\,\mathrm{K}$) an excited atom can only undergo decays to states that are lower in energy, and so while complex it would be possible to consider all possible decay pathways with their individual probability and characteristic wavelength and arrive at a model fluorescence spectrum. However for a system at finite temperature an atom has the possibility of absorbing a blackbody photon and thus undergoing a transition to a state which is higher in energy. This means that from the initial Rydberg state there is an essentially infinite range of possible transitions that an atom can undergo, and so mapping out each allowed decay pathway becomes impossible.

In order to model this complex system we employ a Monte-Carlo simulation of atomic decay from any given Rydberg level. We begin to model the system by first creating a look-up table of the transition probabilities for all possible transitions within the atom, up to a value of principal quantum number n higher than that of the original state. This allows the cumulative density function (CDF) to be calculated for all transitions out of a given state so that decay pathways can be chosen based on a random number selection. We then record the wavelengths of photons emitted through spontaneous emission until the atom reaches its ground state. This process is then repeated and a histogram of emitted wavelengths is recorded. While this model is able to include blackbody-induced transitions between states, it is not

able to account for effects such as collisional population transfer within the vapour. For the calculations of transition probability and wavelength we again make use of `ARC` [14].
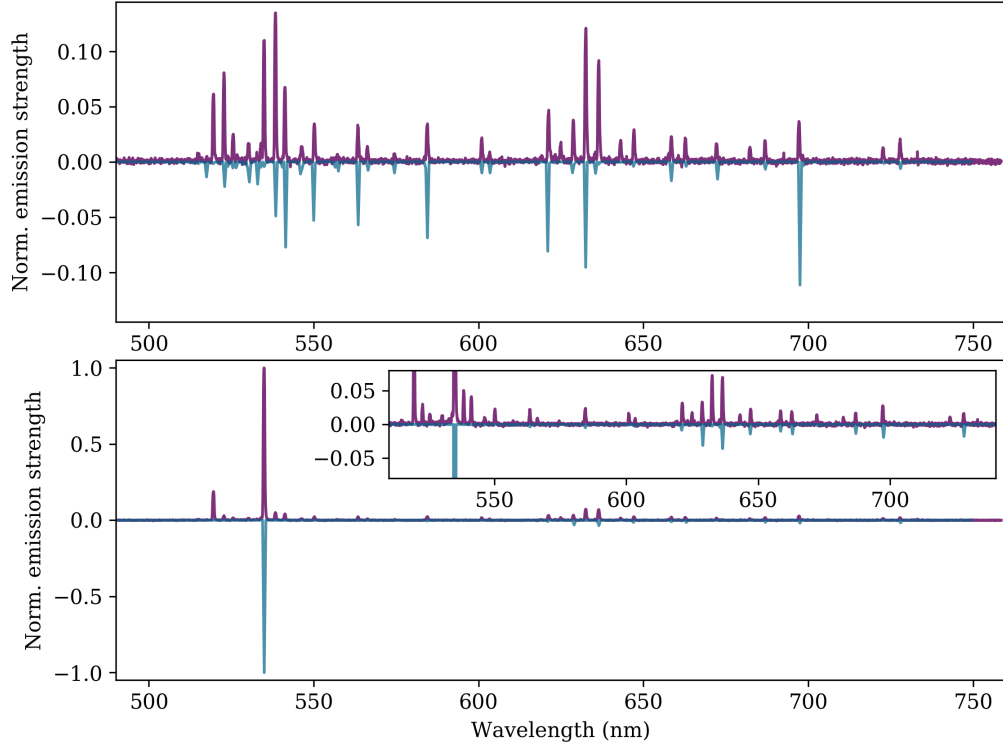
Figure 5.1: **Comparison between measured emission spectra and those predicted by the simple model.** Measured (purple) and simulated (blue) emission spectra from the $14P_{3/2}$ 'THz off' state (*top*) and the $13D_{5/2}$ 'THz on' state (*bottom*). The y axis is normalised to the largest peak, that at $535\,\text{nm}$ in the 'THz on' spectrum. Note the difference in the y axis between the two plots. The inset is included to show the deviation between the data and the model for the weak spectral lines.

Before we use this model to predict the fluorescence spectrum of arbitrary Rydberg states we verify that the results it gives are correct. To do this we use the $14P_{3/2}$ and $13D_{5/2}$ states, which we will refer to as the 'THz off' and 'THz on' states respectively. The atoms are excited to the $14P_{3/2}$ state using a 3-step laser excitation as described in Chapter 3, from there population can be transferred to the $13D_{5/2}$ state via the application of a resonant THz field. For an atomic vapour in

each of these states we use a spectrometer to collect the fluorescence emitted by the atoms, and compare these measured spectra to the ones predicted by our model. We only consider the visible fluorescence (470 nm to 750 nm) and use a shortpass filter to block out any scattered light from the infrared excitation lasers. Further experimental details can be found in Chapter 3. Figure 5.1 shows the measured (purple) and simulated (blue) emission spectra from both the $14P_{3/2}$ ('THz off') and the $13D_{5/2}$ ('THz on') states. The amplitude of the spectra have been normalised to the strongest emission line, that at 535 nm in the 'THz on' case. The 'THz off' spectrum (Fig. 5.1, *left*) comprises many emission lines of comparable strength across the visible band. The wavelengths of many of these emission lines are well reproduced by the simple Monte-Carlo model, however the model fails to accurately predict their relative emission strengths. The strongest emission lines are in the green and red, leading to the vapour appearing orange in colour. The 'THz on' spectrum (Fig. 5.1, *right*) exhibits a strong emission peak at 535 nm corresponding to the $13D_{5/2} \rightarrow 6P_{3/2}$ decay pathway, which is reproduced by the model. However the second largest peak at 520 nm does not appear in the simulated emission spectrum. Even modifying the model to account for the fact that not all of the population will be transferred from the $14P_{3/2}$ into the $13D_{5/2}$ state by the THz field does not explain the origin of this strong emission at 520 nm.
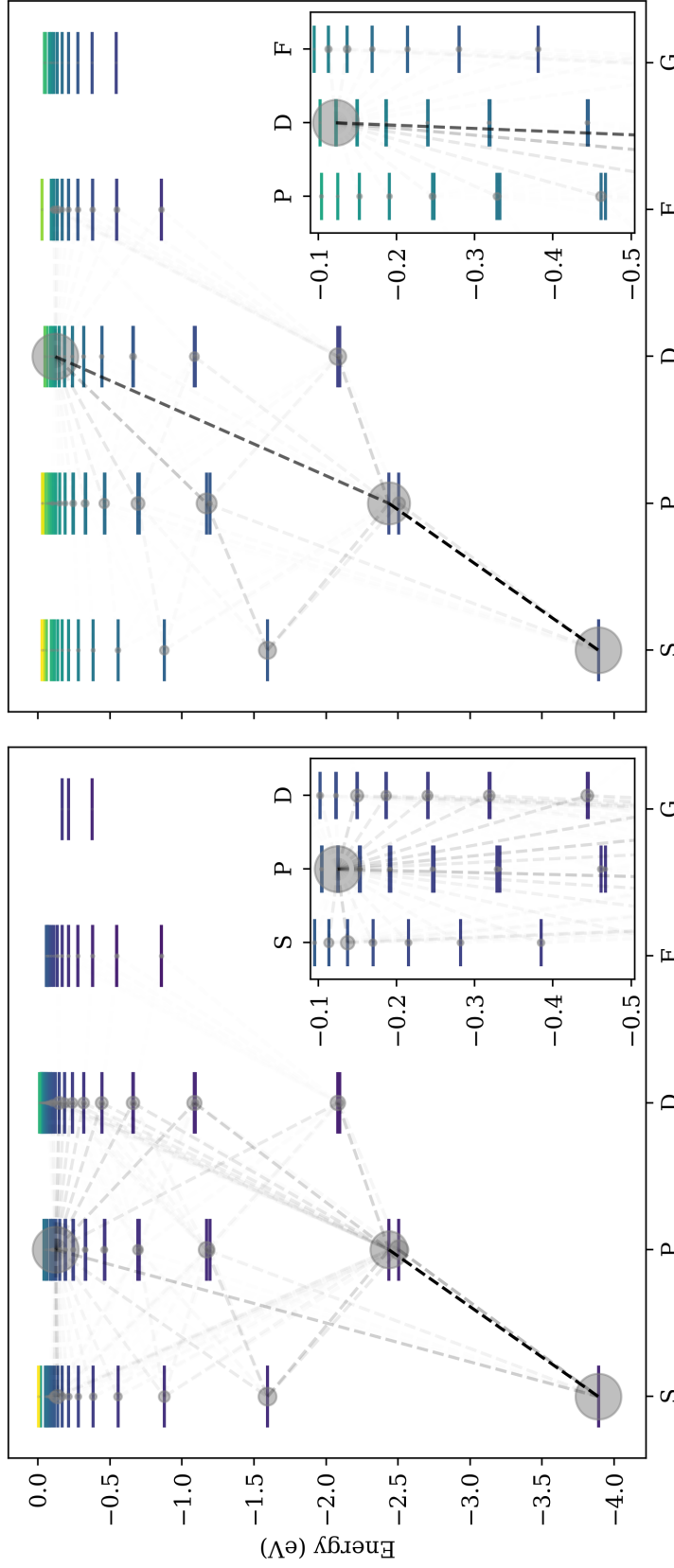
Figure 5.2: **Simulated atomic decay pathways.** Maps of the atomic decays occurring in the Monte-Carlo model for the $14P_{3/2}$ 'THz off' state (*left*) and the $13D_{5/2}$ 'THz on' state (*right*). The horizontal lines represent atomic states featuring in the simulation, the dashed lines represent transitions between states leading to emitted photons. The opacity of the lines represents the probability of the transition occurring, darker lines indicate higher probabilities. The size of the shaded circles represents the percentage of atomic population passing through a particular state, the largest being the initial and final states. The insets in each plot show the transfer of the population from the initially excited states to nearby states, including some states of higher energy.

The contrasting structures of these two spectra can be understood by considering how the atomic population moves between states. We use our model to extract 'which path' information about which transitions have taken place in each iteration, as seen in Fig. 5.2. Here the horizontal lines represent the atomic states that occur in the simulated decay process. The size of the shaded circles corresponds to the fraction of population that passes through that state, the largest being at the initial and final atomic states. The dashed lines represent atomic transitions with the opacity of the line indicating the probability of the transition occurring. In the 'THz off' spectrum we see many emission lines of similar intensity across multiple visible wavelengths. We see that this arises from the fact that there are many transitions occurring with similar probability and the atomic population becomes distributed amongst many different states before returning to the ground state. This is easily seen in Fig. 5.2 (*left*) as the many dashed lines of similar opacity. Note that the strong transition between the ground and first excited state emits photons at $852\,\text{nm}$ and hence is not captured by the spectrometer. In contrast, for the 'THz on' case we see one dominant decay pathway ($13\text{D}_{5/2} \rightarrow 6\text{P}_{3/3}$) corresponding to the strong emission at $535\,\text{nm}$. While there are alternative decay pathways these have a lower probability of occurring and hence result in weaker emission lines in the spectrum. Again the strong transition between the ground and first excited state at $852\,\text{nm}$ is not captured by the spectrometer.
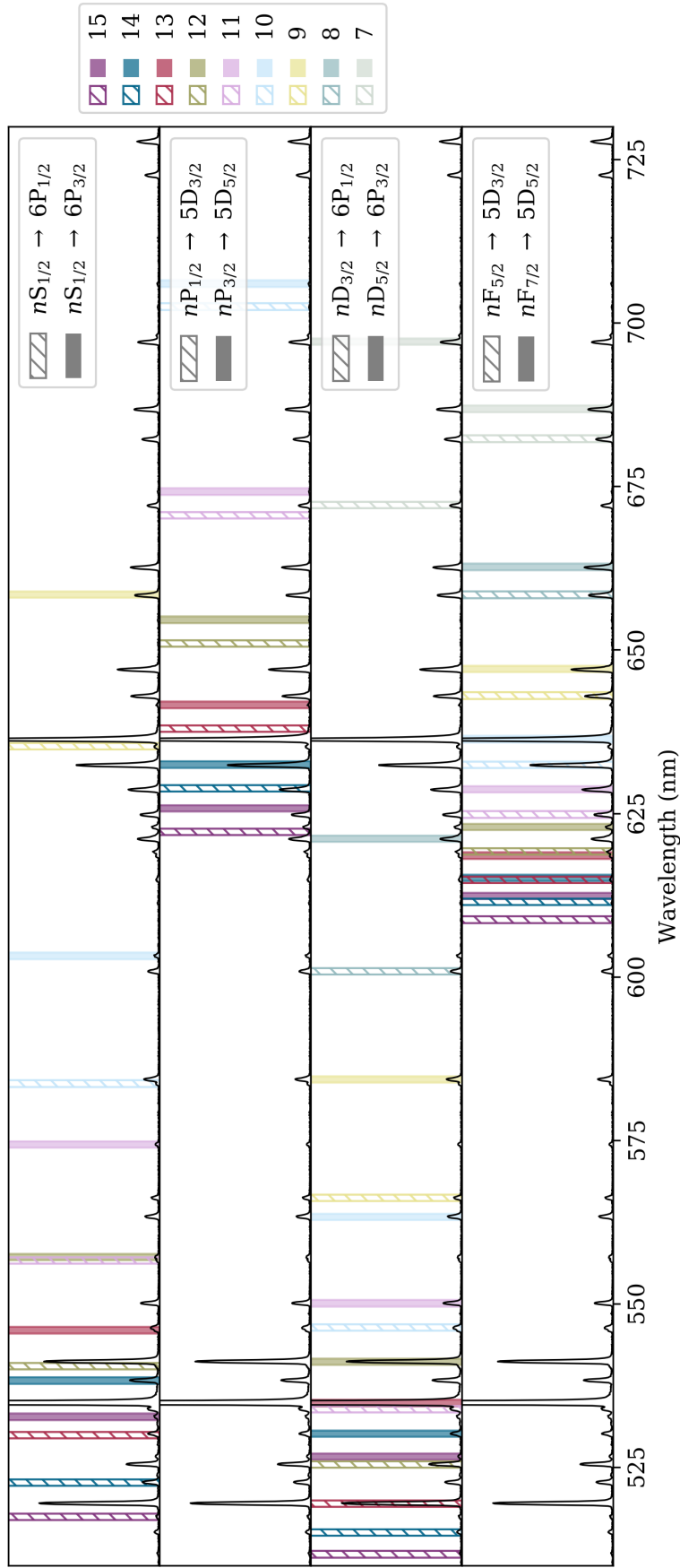
Figure 5.3: **Identifying fluorescence lines by spectral series.** The wavelengths of fluorescence lines for decays from each of the S, P, D and F series are shown as shaded regions. The colours correspond to the principal quantum number n of the decaying state. An example measured fluorescence spectrum ($13D_{5/2}$ taken at $50\,°C$) is shown for reference. In each plot the solid shading represents emission lines arising from decays to higher lying fine structure states while the hatching represents decays to lower energy fine structure states.

To better understand the deviation of the measured spectra from the model we identify peaks in the measured spectra based on their underlying decay pathway, and group them by spectral series (S, P, D etc.). Figure 5.3 shows the wavelength at which we expect peaks corresponding to decays from each spectral series, the colour denotes the principal quantum number n of the initial state. In each plot the solid shaded regions indicate decays between higher energy fine structure states, the hatched regions indicating decays between lower lying fine structure states. Note that most of the peaks in the measured spectrum are accounted for. From this we can identify that the peak at 520 nm that is not predicted in the model arises from the $13D_{3/2} \rightarrow 6P_{1/2}$ decay. The $13D_{3/2}$ state is not populated directly by resonant driving but it is likely that spin-changing collisions occur within the vapour causing the $13D_{5/2} \rightarrow 13D_{3/2}$ transfer [13,96,97].

5.3   Selecting the Optimum Transition for THz Imaging

For the purposes of a THz imaging experiment the parameter of interest is the contrast between the fluorescence emitted by two Rydberg states that can be coupled by a THz field. Ideally we want to be able to use a narrowband filter to select a fluorescence line that is predominantly due to decay from the THz-coupled Rydberg state ('THz on') and remove unwanted background fluorescence from the initial Rydberg state ('THz off'). We also want to have a relatively high probability of emitting a photon at the target wavelength to give a good THz-to-optical conversion efficiency. Our simple model enables us to extract both of these important parameters without experimentally exploring the many hundreds of possible THz transitions available in caesium.

5.3.1   Figure of Merit

In order to evaluate the potential of different transitions for THz imaging we need to establish a figure-of-merit (FoM) that we can extract from the Monte-Carlo model.

When taking images we measure the 'THz on' minus the 'THz off' fluorescence signal, $f_{\text{on}} - f_{\text{off}}$, within a fixed wavelength range of the peak 'THz on' emission wavelength. This width corresponds to being able to choose a narrowband filter around our wavelength of interest allowing us to remove background fluorescence at wavelengths other than the target signal wavelength. We will refer to photons within this wavelength range of interest as signal photons. The total fluorescence signal from the vapour $f \propto n_{\text{on}}p_{\text{on}} + n_{\text{off}}p_{\text{off}}$ where $n_{\text{off,on}}$ is the number of atoms in the 'THz off' and 'THz on' states respectively (the initial and final Rydberg states) and $p_{\text{off,on}}$ are the probabilities of a signal photon being emitted by atoms in these states. Let N be the total number of Rydberg atoms in the vapour such that $N = n_{\text{off}} + n_{\text{on}}$. In the absence of the THz field, we assume all atoms are in the 'THz off' state so the fluorescence signal is given by

$$f_{\text{off}} = n_{\text{off}}p_{\text{off}} = Np_{\text{off}}. \tag{5.3.1}$$

When the THz field is applied, some of the atoms will be transferred to the 'THz on' state and the fluorescence signal will be given by

$$f_{\text{on}} = n_{\text{off}}p_{\text{off}} + n_{\text{on}}p_{\text{on}} \tag{5.3.2}$$

$$= (N - n_{\text{on}})p_{\text{off}} + n_{\text{on}}p_{\text{on}}. \tag{5.3.3}$$

We can then write our measured signal as

$$f_{\text{on}} - f_{\text{off}} = p_{\text{off}}(N - n_{\text{on}}) + n_{\text{on}}p_{\text{on}} - Np_{\text{off}} \tag{5.3.4}$$

$$= n_{\text{on}}p_{\text{on}} - n_{\text{on}}p_{\text{off}} \tag{5.3.5}$$

$$= n_{\text{on}}(p_{\text{on}} - p_{\text{off}}). \tag{5.3.6}$$

This indicates that our eventual measured signal will be proportional to the number of atoms in the 'THz on' state n_{on} multiplied by the difference in probabilities $p_{\text{on}} - p_{\text{off}}$ of emitting a signal photon from the two states. Hence we choose the $p_{\text{on}} - p_{\text{off}}$ quantity from the model as our FoM when deciding on which states will be suitable for imaging. The dependence on n_{on} indicates that we also need to consider the amount of population that can be transferred by the THz field. Assuming we are always in the strongly damped regime (where the damping rate is much larger

than the driving field Rabi frequency) we expect $n_{\text{on}} \propto \Omega_{\text{THz}}^2$ where Ω_{THz} is the Rabi frequency of the THz field [58] [eqn. 9.57]. Hence n_{on} (and therefore $f_{\text{on}} - f_{\text{off}}$) will depend on the square of the dipole matrix element of the THz transition $\mathbf{d}_{\text{off}\to\text{on}}^2$ and linearly on the power of the THz field P_{THz}. This agrees with our measurements of fluorescence signal with power in Chapter 6. This relationship allows us to use our fluorescence model along with knowledge of the dipole matrix elements and information about the power output of our THz source to predict the signal strength of any given transition and hence choose the best pair of states for THz imaging.

Figure 5.4 shows an example of using the Monte-Carlo model to find the best THz transition for imaging in the frequency range of our THz source. The predicted fluorescence signal is found by multiplying the FoM from the fluorescence simulation by the square of the dipole matrix element of the THz transition $\mathbf{d}_{\text{off}\to\text{on}}^2$. Although there are 388 transitions in the frequency range of the THz source, Fig. 5.4 shows that most of them will produce negligible signals for imaging. For the transitions that will give good signal levels, we also need to consider the dipole matrix element of the $7\text{S}_{1/2} \to \text{THz}_{\text{off}}$ transition, as this will affect the total number of atoms in the 'THz off' state and hence the total number of atoms available for the THz transition. Assuming a constant laser power the number of atoms in this state will be proportional to the square of the dipole matrix element $\mathbf{d}_{7\text{S}_{1/2}\to\text{THz}_{\text{off}}}^2$, represented by the colour of the scatter points in Fig. 5.4. The final parameter to consider is the THz power available at the transition frequency. Once this is taken into account we find two viable imaging transitions with high predicted signal levels and dipole matrix elements; the $14\text{P}_{3/2} \to 13\text{D}_{5/2}$ transition at $550\,\text{GHz}$ and the $13\text{P}_{3/2} \to 12\text{D}_{5/2}$ transition at $750\,\text{GHz}$. We predict that these two transitions would give similar signal levels for the same applied THz power, however as can be seen from the dashed line in Fig. 5.4, the output of our THz source at $750\,\text{GHz}$ is negligible. The size of the points represents the total predicted signal level, given by $\mathbf{d}_{7\text{S}_{1/2}\to\text{THz}_{\text{off}}}^2 \mathbf{d}_{\text{off}\to\text{on}}^2 (p_{\text{on}} - p_{\text{off}}) \times P_{\text{THz}}$. From this we predict that the $14\text{P}_{3/2} \to 13\text{D}_{5/2}$ transition will give the largest total signal, around 7 times greater than the next best transition. This optimum imaging transition will be used for the rest of the work in this thesis.
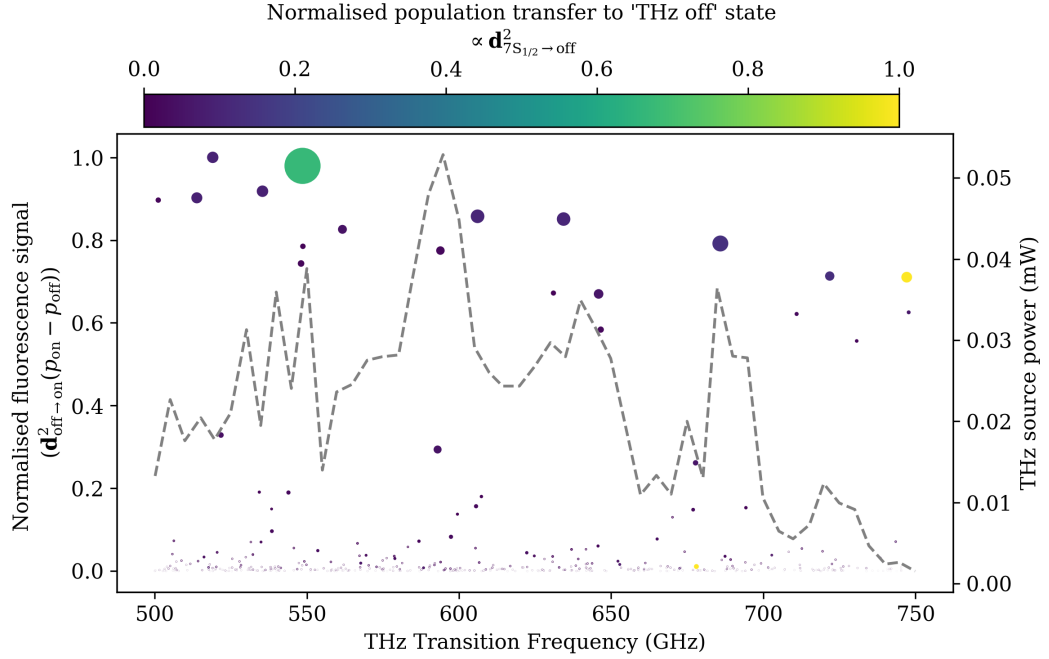
Figure 5.4: **Evaluation of THz transitions for imaging.** Using the model we can predict the figure-of-merit (FoM) for all transitions in the range of our THz source and compare them. The scatter points represent the frequency of the transition against its predicted fluorescence signal strength ($\mathbf{d}^2_{\text{off}\to\text{on}}(p_{\text{on}} - p_{\text{off}})$). The colour of the points is related to the square of the dipole matrix element of the transition to the initial Rydberg state $\mathbf{d}^2_{7\text{S}_{1/2}\to\text{THz}_{\text{off}}}$, giving an idea of how much population can be transferred to the 'THz off' state for a fixed laser power. The dashed line indicates the relative power of our THz source as a function of frequency. The size of the points represents the total predicted signal ($\mathbf{d}^2_{7\text{S}_{1/2}\to\text{THz}_{\text{off}}}\mathbf{d}^2_{\text{off}\to\text{on}}(p_{\text{on}} - p_{\text{off}}) \times P_{\text{THz}}$). We conclude from this that the best transition for imaging is the $14\text{P}_{3/2} \to 13\text{D}_{5/2}$ transition at $550\,\text{GHz}$.

5.4 Evolution of Fluorescence with Temperature

In order to gain further insight into atomic processes that contribute to the emitted fluorescence, we investigate the temperature dependence of the emission lines by recording fluorescence spectra at varying cell temperatures. We expect the strength of each line to increase with temperature due to the increasing atomic number density in the vapour. This will affect the strength of all lines equally, regardless of their origin. There may also be increased contributions from blackbody radiation which would affect lines differently depending on their underlying decay pathways. We can simulate the effect of increasing temperature by calculating a revised table of transition rates for each temperature in question, and then multiplying the simulated spectra by the corresponding number density. When we do this we find negligible variation due to the differing blackbody spectrum as the considered temperature range is relatively small.

Once the origins of the peaks have been identified (as in Fig. 5.3), we examine their temperature dependence by extracting the peak height for varying vapour temperatures between 35 °C and 75 °C. We then plot these peak heights as a function of temperature and group them by spectral series in Figure 5.5. The datapoints represented by dots are those in the 'THz on' spectrum, the crosses represent peaks in the 'THz off' spectrum. When considering the spectra in the presence of the THz field, we have to consider the possibility that not all of the population will be transferred to the 'THz on' state. This means there could still be spectral lines arising from atoms decaying out of the 'THz off' state.
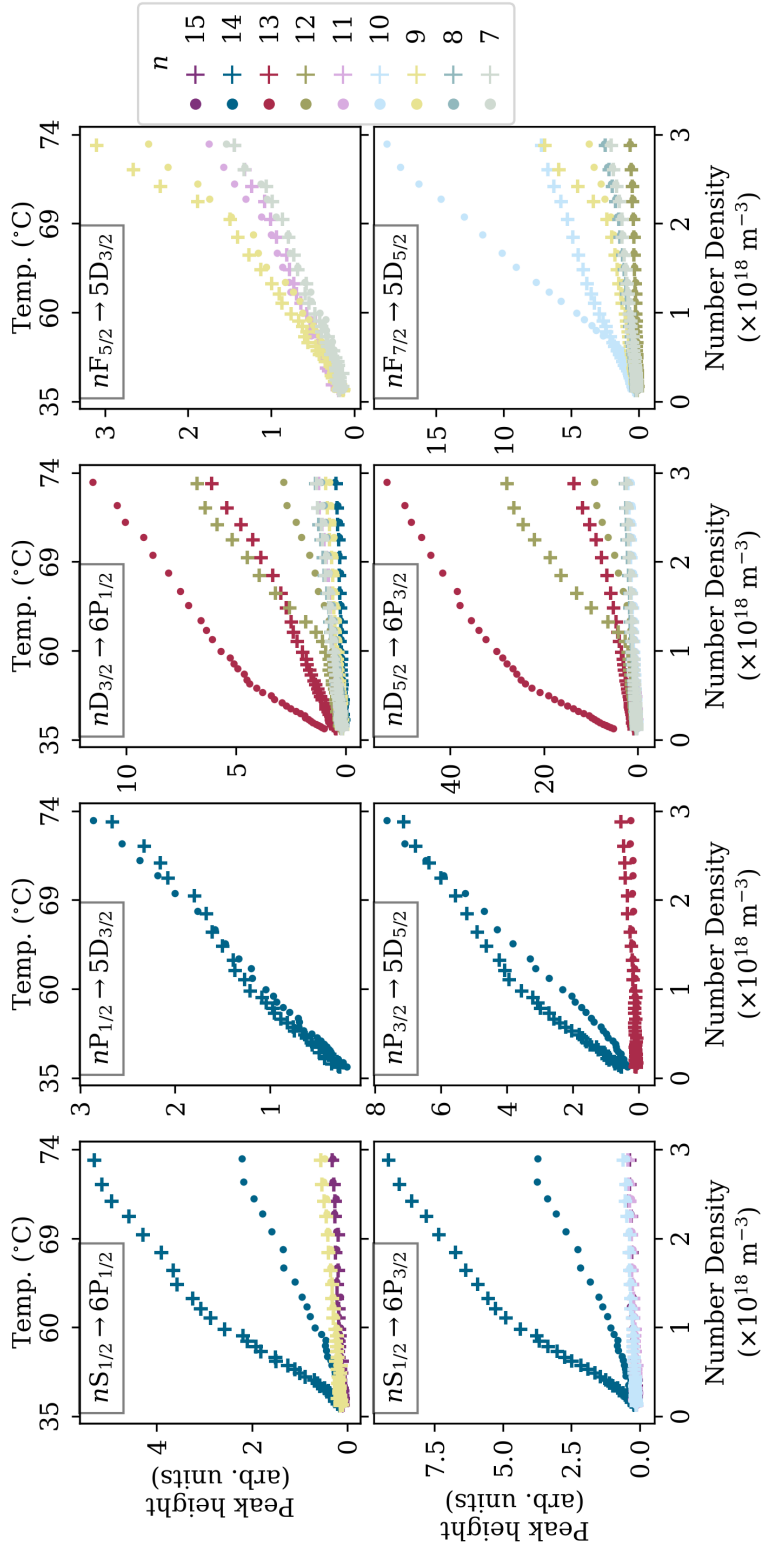
Figure 5.5: **Fluorescence emission as a function of temperature and number density.** The height of the peaks identified in Fig. 5.3 are plotted as a function of temperature (atomic number density). The dots correspond to peaks in the spectrum from the 'THz on' state, the crosses are for those in the 'THz off' spectrum. Decay pathways that are unresolved in Fig. 5.3 are omitted here for clarity. We do however include decays from the 14P states as we expect decays on these channels to be stronger than others at these wavelengths.

S Series ($nS_{1/2} \rightarrow 6P_{1/2,3/2}$)

For the S series (first column, Fig. 5.5) the dominant decays are from the $14S_{1/2}$ state (dark blue), both with and without the THz field. We see more decays from this state in the 'THz off' case, possibly because more population is available to undergo the $14P_{3/2} \rightarrow 14S_{1/2}$ transition. In this case there appears to be two regimes above and below an atomic number density of $1 \times 10^{18}\,\mathrm{m^{-3}}$, at which point the rate of increase slows. We also see some decays out of the other $nS_{1/2}$ states which increase linearly with number density as expected.

P Series ($nP_{1/2,3/2} \rightarrow 5D_{3/2,5/2}$)

The dominant decay in the P series is from the initially populated $14P_{3/2}$ state, although we see stronger decay from the $14P_{1/2}$ state than predicted. This is possibly due to the effect of collisions that are not included in the model. While the peak height in the 'THz on' case is linear with number density, the 'THz off' case again seems to exhibit two separate regimes. One would expect to see more decay from the 14P states in the absence of the THz field as population is prepared in this state, however at a number density of $2 \times 10^{18}\,\mathrm{m^{-3}}$ we see more decays out of these states when the THz field is on.

D Series ($nD_{3/2,5/2} \rightarrow 6P_{1/2,3/2}$)

The dominant decay in the D series is from the 13D states. This is expected in the presence of the THz field which transfers population into the $13D_{5/2}$ state. Collisional transfer could then lead to the population of the $13D_{3/2}$ state and subsequent decay from here. We also see more decays from these 13D states in the 'THz off' case than is predicted by the model. The $14P_{3/2} \rightarrow 13D_{5/2}$ transition and the subsequent decay from the $13D_{5/2}$ state are key to our THz imaging scheme and the unpredicted decay on this channel is unfortunate as it means that the measured contrast will be lower than calculated. We also see an interesting dependence of decay from the 12D states (green points) on temperature. At a number density of around $1 \times 10^{18}\,\mathrm{m^{-3}}$ we see a sharp turn-on in decays from these levels, the rate of which is sustained.

This behaviour is not predicted at any point by the model, and so is not due to an interaction with blackbody radiation.

F Series $(n\text{F}_{5/2,7/2} \rightarrow 5\text{D}_{3/2,5/2})$

Again most of the decays from the F states are predicted to occur from lower lying nF levels, with all of the lines increasing proportional to atomic number density. However in the presence of the THz field we see far more decay on the $10\text{F}_{7/2} \rightarrow 5\text{D}_{5/2}$ transition than is predicted by the model. At number densities greater than $2 \times 10^{18}\,\text{m}^{-3}$ this line becomes the second strongest line in the spectrum, overtaking that from the $13\text{D}_{3/2}$ decay. We also see a sharp turn-on for decays out of the 9F states, again at number densities of $2 \times 10^{18}\,\text{m}^{-3}$. Looking at the simulated 'which path' information (as in Fig. 5.2) we can see that the most probable route from a 14P state to a 9F state is via a 12D state, so it is interesting that it is these two sets of states that exhibit turn-on features.

The fact that many fluorescence lines exhibit temperature dependent behaviour that is not predicted by the simple Monte-Carlo model leads us to conclude that it is not simply the change in the blackbody spectrum that is driving these changes. One possible mechanism is that the increased number density leads to plasma formation within the vapour. The local electric field generated could then cause Stark mixing of the states leading to a change in emitted fluorescence. While the turn-on of certain decay pathways could be due to cooperative behaviour and a superradiant cascade, we are working at much lower number densities than in works that have previously observed this behaviour [92], and we do not see any suppression of other decay pathways as would be expected for superradiance. Another possibility is that state-mixing collisions occur within the vapour causing population transfer to states that are not coupled by the dipole operator [13,96,97].
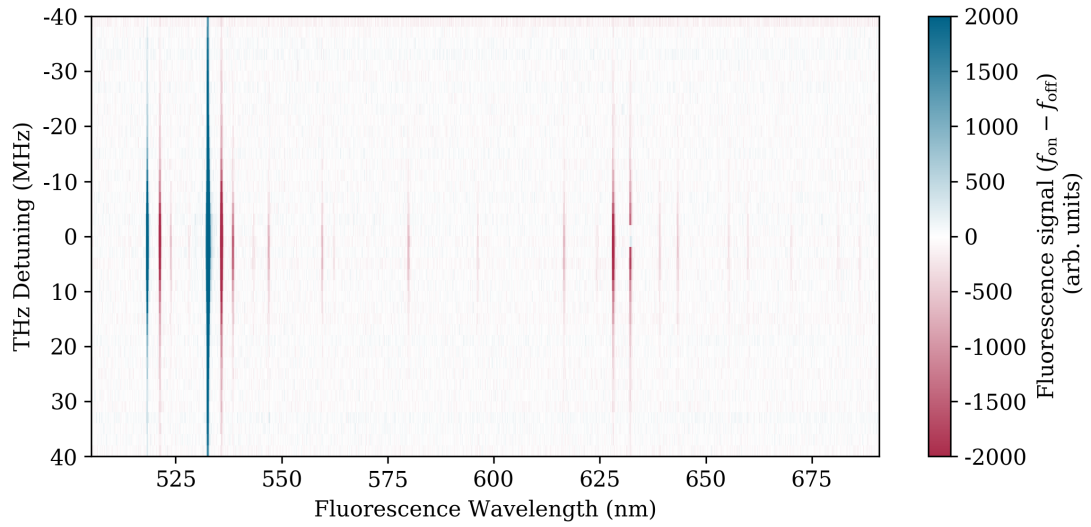
Figure 5.6: **Evolution of fluorescence with THz detuning.** The fluorescence signal $(f_{\mathrm{on}} - f_{\mathrm{off}})$ as a function of THz detuning for a cell temperature of 56 °C. The blue regions indicate fluorescence lines that increase in the presence of the THz field, whereas the red regions are lines that are suppressed. The fluorescence at 635 nm, corresponding to the $10F_{7/2} \rightarrow 5D_{5/2}$ decay, exhibits an increase in a narrow frequency region around zero detuning.

5.5 Evolution of Fluorescence with THz Detuning

In this section we vary the detuning of the THz field and investigate the effect on the fluorescence signal $f_{\mathrm{on}} - f_{\mathrm{off}}$, as shown in Fig. 5.6. The blue shaded regions indicate wavelengths at which the total fluorescence signal is positive as the THz field is tuned through resonance, and the red shaded regions correspond to wavelengths at which fluorescence is suppressed and the fluorescence signal is negative. The fluorescence wavelengths that exhibit the greatest enhancement when the THz field is resonant are 535 nm and 520 nm, corresponding to the strongest emission lines in the 'THz on' spectrum (decay from the 13D states). The emission lines that are actively suppressed when the THz field is on resonance correspond to those that appear in the fluorescence spectrum from the 'THz off' state but not in the spectrum from the 'THz on' state. This suppression is due to population being transferred out of the $14P_{3/2}$ state by the resonant THz field.

The fluorescence at around 635 nm, corresponding to the $10F_{7/2} \rightarrow 5D_{5/2}$ decay,
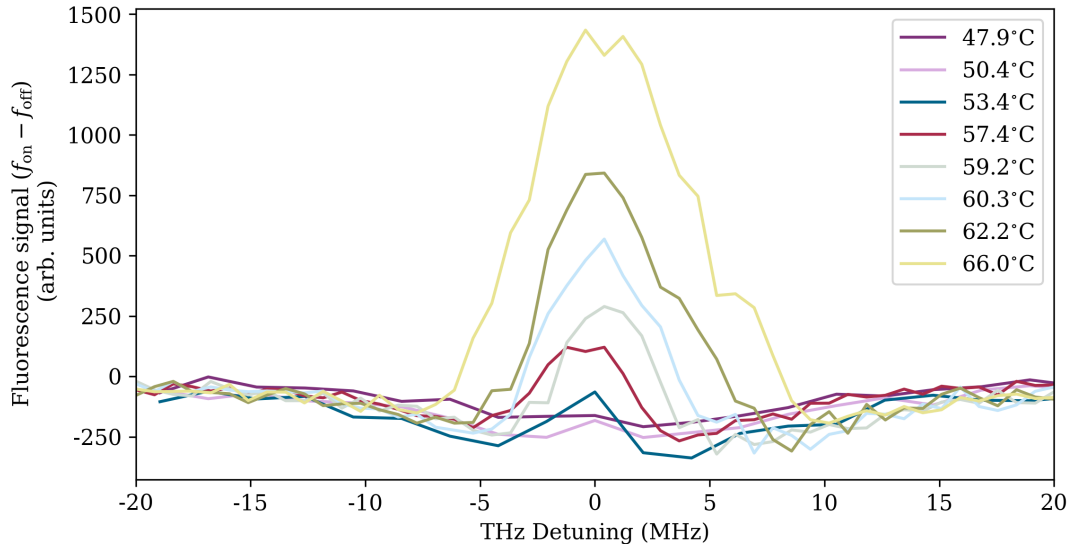
Figure 5.7: **Evolution of the fluorescence from the 10F$_{7/2}$ state as a function of temperature.** The fluorescence signal between 633 nm and 637 nm, identified as being due to the 10F$_{7/2} \rightarrow$ 5D$_{5/2}$ transition, is plotted as a function of THz detuning for varying cell temperatures. At a cell temperature of 54°C we see the emergence of a feature around zero THz detuning which increases with temperature.

exhibits interesting temperature dependent behaviour. Figure 5.7 shows the change in fluorescence from this state as a function of THz detuning and temperature. For cell temperatures below 50 °C the fluorescence in this wavelength region decreases as the THz field is tuned to be resonant (purple lines, Fig. 5.7), however as we increase the cell temperature we see a sharp increase in fluorescence in a narrow THz frequency range around zero detuning. This feature is much narrower than other fluorescence lines with a FWHM of < 10 MHz. If we continue to increase the temperature we see a greater increase in fluorescence and the feature broadens. No other fluorescence lines exhibit this frequency dependent behaviour between 35 °C and 70 °C. Above 70 °C we see the emergence of similar behaviour at 632 nm, possibly corresponding to decay from the other 10F state. This is inconclusive however as this line is unresolveable from fluorescence caused by the 14P$_{3/2} \rightarrow$ 5D$_{5/2}$ transition which we would expect to be stronger.

5.6   Conclusion

This chapter motivated the need to be able to predict fluorescence spectra from many different Rydberg states and presented a simple Monte-Carlo model allowing us to do so. We highlighted the ability of the model to predict the strongest fluorescence lines from a Rydberg state but showed that there are processes leading to emission at wavelengths not predicted by the simple model. We described how the model allowed us to select the THz transition that would give the best signal for THz imaging, the $14P_{3/2} \rightarrow 13D_{5/2}$ transition at $550\,\text{GHz}$. We also performed a study of the emitted fluorescence as a function of vapour temperature, and found effects that could not be replicated by the Monte-Carlo approach. Previous work [92] indicated the presence of cooperative behaviour at high number densities which modified the spectrum of the observed fluorescence. While this effect may account for the anomalous lines seen in our measured spectra, our Rydberg atom density and driving intensity is much lower than in works where these phenomena were observed. These anomalous lines could be caused by varying electric fields in the vapour due to plasma formation but investigating this hypothesis further would require significant modifications to the vapour cell design and so is left as a topic for future experiments. The deviations from the model could also arise due to collisional processes, and while the model could be adapted to include these it would require significant modifications and extensions.

Chapter 6

THz Imaging

In this chapter we describe how we make use of the caesium Rydberg atom system outlined in Chapter 3 to perform high speed 2D THz imaging. We characterise the spatial and temporal resolution of the imaging system and measure the minimum detectable power. We also discuss some of the problems and limitations of this technique and highlight future improvements.

6.1 Introduction

Since the seminal work of Hu & Nuss in 1995 [98] imaging using THz wavelengths has been of interest to researchers. The ability of THz radiation to pass through many dielectric materials such as paper, cloth and plastics makes it an ideal tool for many applications such as security screening [28] and non-destructive testing [32,99], while the fact that it is non-ionising means that it has potential for use in biomedical settings [29, 31]. However compared to optical and IR frequencies there is relatively little technological development in the THz band. Advances that have been made have led to imaging systems that are too slow or too low resolution to be widely useful in practical settings [25, 30].

As we explored in Chapter 1, Rydberg atoms have been shown to be sensitive detectors to radiation in the microwave [15] and THz [18] frequency ranges. While the experiments described in these works can be used to image the incident fields [16,17], the images are built up pixel by pixel and so acquisition is a lengthy process. Other
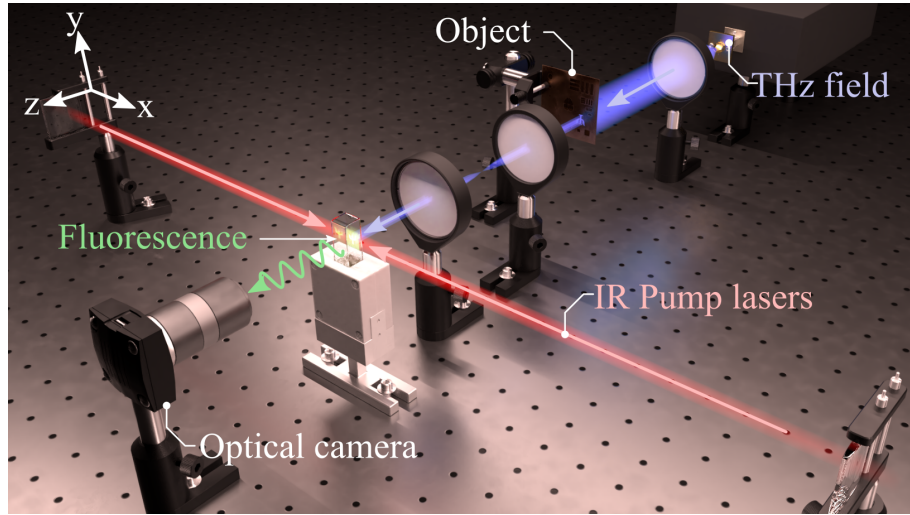
Figure 6.1: **THz imaging using atomic vapour.** A 3D render of the THz imaging set-up described in Chapter 3 and used in this chapter. Infrared pump lasers form a sheet of Rydberg atoms within the vapour cell. The THz field passes through an object which is imaged onto the atoms using Teflon lenses. Interaction of the THz field with the excited atoms leads to the emission of green fluorescence which is captured using an optical camera. Fig. from [53] courtesy of A. MacKellar.

attempts at using Rydberg atoms to image THz fields involved using a Rydberg atom photocathode [24] but again this method could not demonstrate high spatial or temporal resolution.

Recently Rydberg atoms in a room temperature vapour were used to perform THz-to-optical conversion [51] and thus image an incident THz field. This method was able to demonstrate sub-wavelength resolution in the near field and do so in real time. In this chapter we build on this previous demonstration and extend it to a full 2D imaging system with potential practical applications. We show that this new far-field atom-based imaging system has near diffraction-limited spatial resolution and is capable of video capture at kHz frame rates.

6.2 Basic Principles

The principle of operation is to use the atomic system described in earlier chapters to perform THz-to-optical frequency conversion, converting THz radiation into

optical photons that can be detected on any optical camera. The electric dipole transitions between neighbouring Rydberg states of alkali atoms lie in the THz frequency range [13] and have very large dipole moments resulting in a high probability of interaction with a resonant THz field.

In Chapter 5 we described the principle of using the difference in fluorescence emitted by two Rydberg states to determine whether a THz field was present. We also defined a figure-of-merit for choosing a 'good' pair of states with which to perform THz imaging. This led us to conclude that the $14P_{3/2} \rightarrow 13D_{5/2}$ transition at $0.55\,$THz would be optimum for our system, hence this transition is used throughout this and subsequent chapters. Figure 6.2 shows the measured fluorescence spectra from the $14P_{3/2}$ (dotted purple line) and the $13D_{5/2}$ states (solid blue line). The strongest optical emission from the THz-coupled $13D_{5/2}$ state is at $535\,$nm corresponding to the $13D_{5/2} \rightarrow 6P_{3/2}$ decay, hence we choose a narrowband filter centred on $535\,$nm to isolate fluorescence on this channel. The transmission of the selected filter is shown by the shaded region in Figure 6.2. By using this filter we get a twofold increase in our background subtracted signal. For each THz photon absorbed by the system we have a 52.4% chance of emitting a signal photon at $535\,$nm, allowing us to perform THz-to-optical conversion with reasonable efficiency.

We create a practical $1\,$cm^2 THz imaging sensor using our atomic THz-to-optical conversion process by forming a 2D sheet of excited atoms onto which a THz field image can be projected. The experimental details of this configuration can be seen in Figure 6.1 and are described fully in Chapter 3. The fluorescence emitted by atoms in the region of overlap between the excitation lasers and the THz beam is re-imaged onto an optical camera, providing an image of the incident THz field in a single shot. The versatility of this approach means that any optical camera can be employed, and can easily be substituted into the system.

6.3   Characterisation

In order to establish how well our atomic-vapour based THz imaging scheme performs and compare it to other methods we characterise the important aspects of the
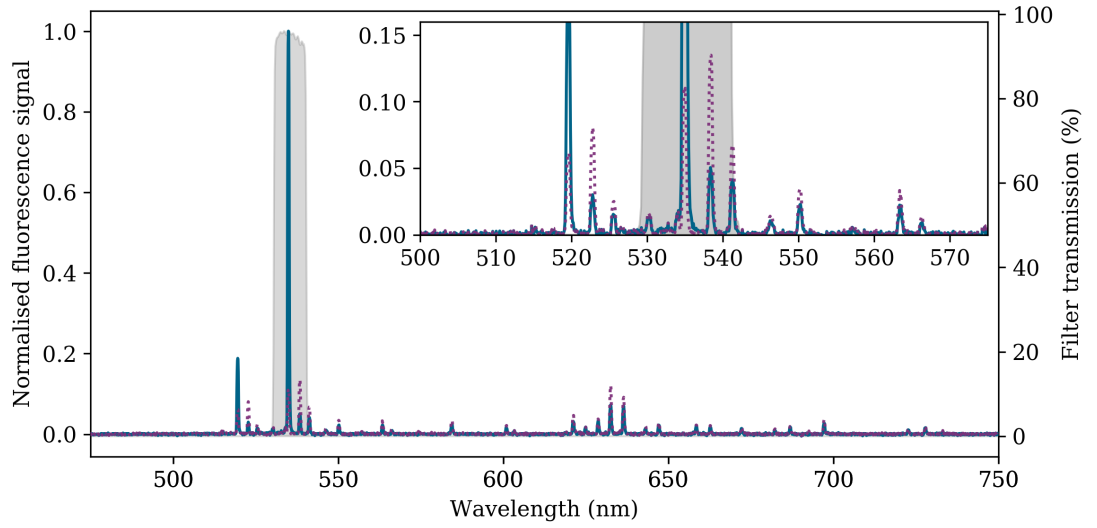
Figure 6.2: **Transmission of the narrowband optical filter.** The measured fluorescence spectrum from the $14P_{3/2}$ ('THz off') and $13D_{5/2}$ ('THz on') states (dotted purple and solid blue lines respectively). The transmission of the narrowband filter used to isolate the signal photons at $535\,\mathrm{nm}$ is shown as the grey shaded region. The inset shows the region of filter transmission in detail.

system. These include measuring the spatial and temporal resolution, establishing the minimum detectable power and measuring the linewidth of the vapour response.

6.3.1   Spatial Resolution

To ascertain the spatial resolution of the system we image a metallic 'test card' comprising apertures of varying sizes and shapes (see Fig. 6.3, *centre*). Images of a $0.50\,\mathrm{mm}$ diameter pinhole and 'Ψ'-shaped aperture are shown both as true-colour unprocessed photographs taken with a DSLR camera and as false-colour filtered images taken with the Andor iXon. By considering the image of the $0.50\,\mathrm{mm}$ diameter pinhole to be the point spread function (PSF) of the system we are able to compare the performance to that of an ideal imaging system. Since the diameter of the pinhole is sub-wavelength, we assume that it can be treated as a point source and hence that the intensity I at a radial distance r from the centre will be given by an Airy pattern [66] [eqn. 5.18],
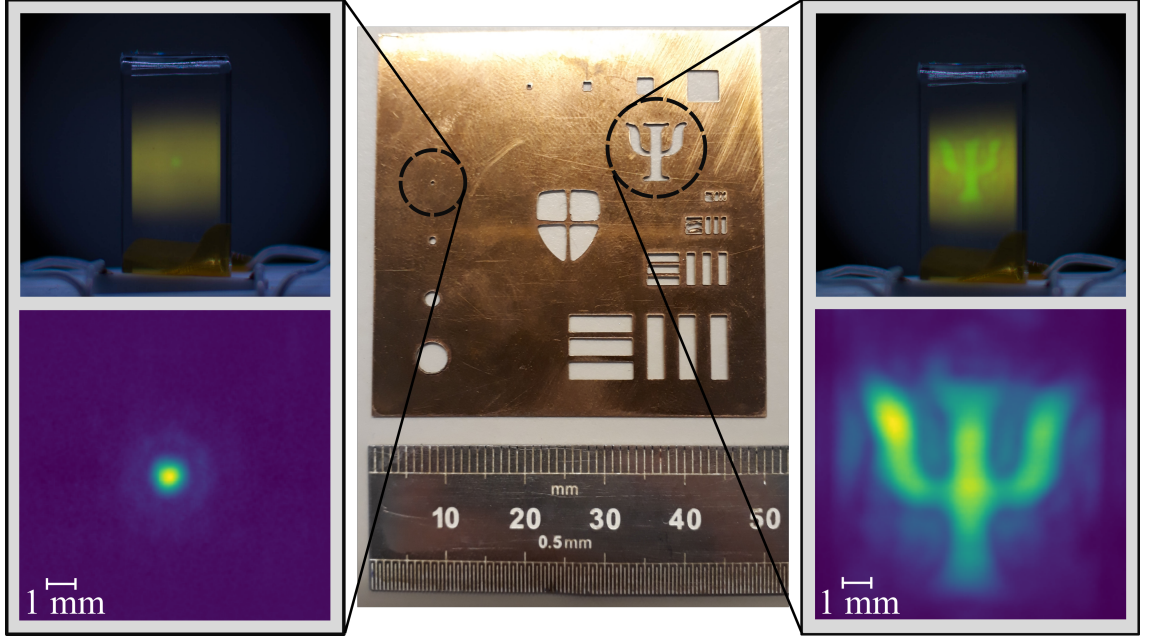
Figure 6.3: **Demonstration of spatial resolution.** A metal mask (*centre*) is placed in the object plane of the system. To the left and right are true colour images taken with a DSLR camera (*above*) and false colour images taken with the Andor iXon (*below*) for a 0.50 mm diameter pinhole (*left*) and a 'Ψ'-shaped aperture (*right*).

$$I(a) = I_0 \left(\frac{2J_1(a)}{a} \right)^2, \tag{6.3.1}$$

where $J_1(x)$ is the Bessel function of the first kind and

$$a = \frac{\pi r}{\lambda N}. \tag{6.3.2}$$

Here λ is the wavelength of the imaging light, equal to 0.55 mm and N is the f-number of the imaging system. The factor I_0 defines the maximum intensity at the centre of the image. We calculate the f-number of our THz lens system using

$$N = \frac{f}{D}, \tag{6.3.3}$$

where f is the focal length of the lens and D is its effective aperture. For our Teflon lenses, $f = 75$ mm and $D = 50$ mm, giving us an f-number of $N = 1.5$. We normalise both the real and ideal unaberrated PSF such that the total power in each image is equal. These images are shown in the central panels of Fig. 6.4. We then perform a
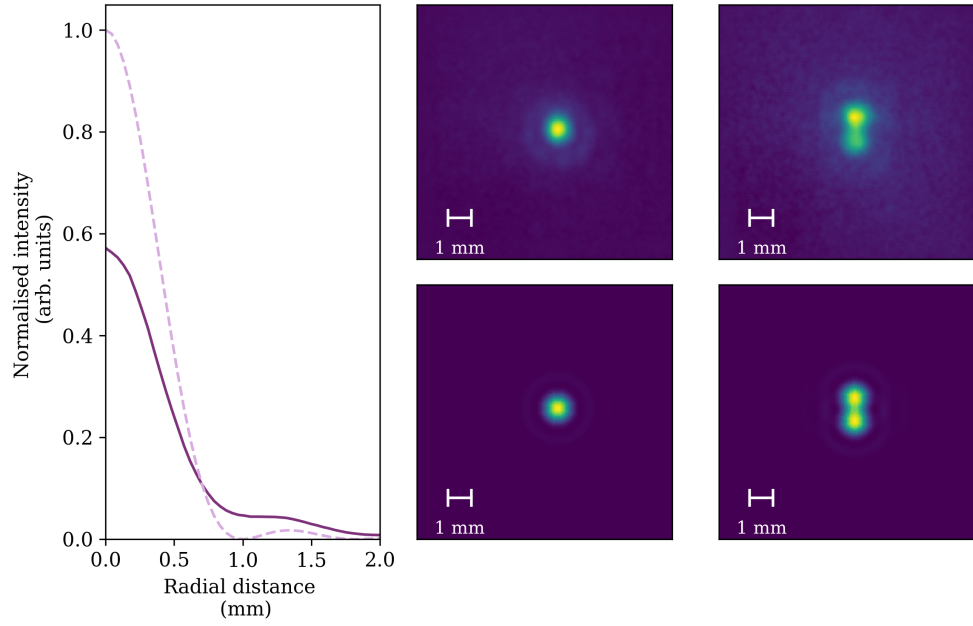
Figure 6.4: **Strehl Ratio and Rayleigh criterion.** *Left:* Intensity distribution of our measured PSF (dark purple solid line) and an ideal PSF (light purple dashed line) from which we measure a Strehl ratio of 0.57. *Centre:* Measured (*top*) and simulated (*bottom*) images of a single 0.50 mm diameter pinhole, from which the intensity distributions are obtained. *Right:* Measured (*top*) and simulated (*bottom*) images of two 0.50 mm diameter pinholes separated by 1.00 mm.

radial average about the point of peak intensity, the results of which are plotted on the left hand side of Fig. 6.4. By calculating the ratio of the maximum peak heights we extract a Strehl ratio for our system of 0.57, indicative of a moderately aberrant system. We posit that these aberrations arise from the simple design of the THz lenses used.

Another measure of the resolving power of a system is to consider the Rayleigh criterion, that two Airy patterns of equal intensity are 'just resolved' when the maximum of one lies over the first minimum of the other [66]. The first minimum of the function in equation 6.3.1 is given by the first zero of the Bessel function at $a = 3.8317$, giving a peak to minimum distance of $r = 1.01$ mm. This means that our system should be able to resolve two point sources separated by 1.00 mm. We demonstrate this ability by imaging a mask comprising two 0.50 mm diameter pinholes separated by 1.00 mm (Fig. 6.4, *right*). The resulting image (*top*) closely re-
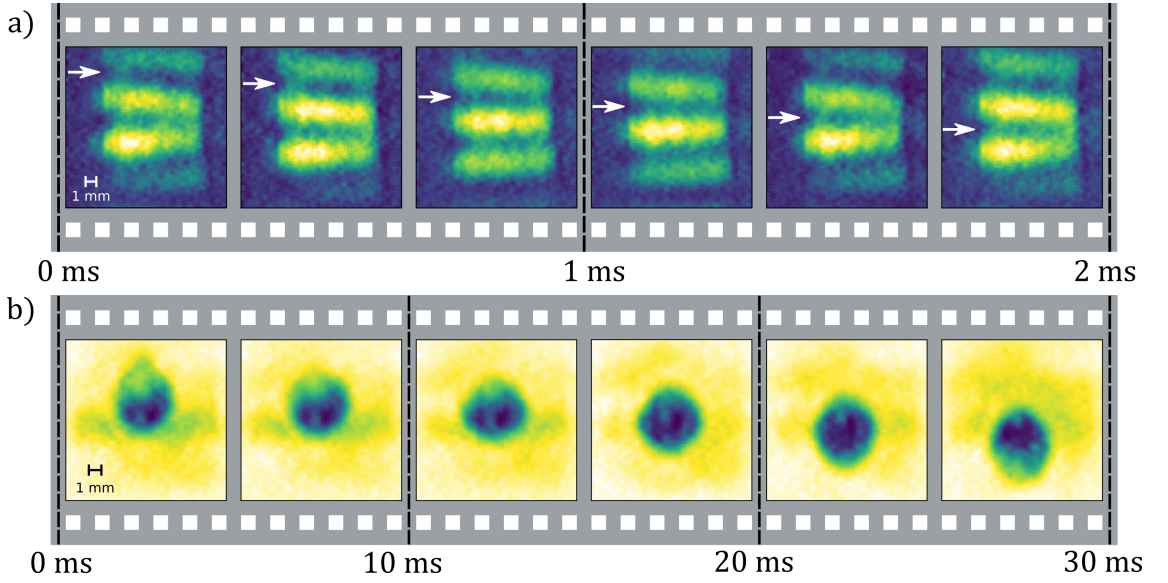
Figure 6.5: **Ultra-high-speed THz video.** (a) Subsequent frames from a THz video of an optical chopper wheel rotating at 700 rpm, imaged at a frame rate of 3 kHz. The white arrow is added to highlight the movement of one spoke of the wheel between frames. (b) A significantly slower frame rate of 500 Hz is sufficient to capture the dynamics of a water droplet in free fall shortly after being released from a burette, every fourth frame of which is shown here. Figure taken from [53]

sembles the simulated image (*bottom*) in which the two distinct apertures are clearly resolved, providing an upper bound of 1.00 mm on the system's spatial resolution.

6.3.2 Temporal Resolution

To illustrate the high speed capabilities of this technique we demonstrate THz imaging of dynamical processes at frame rates up to 3 kHz, two orders of magnitude faster than the current state of the art [50]. Here, we use the high-speed Photron FAST-CAM to capture videos of a water droplet in free fall at a frame rate of 500 Hz and a rotating optical chopper wheel at 3 kHz. Frames from each video are presented in Fig. 6.5. Although the frames in Fig. 6.5(b) were taken at a frame rate of 500 Hz, only every fourth frame is shown to illustrate the changing shape of the water drop in free fall captured in the video. To improve image clarity we perform post-processing on the captured frames, details of which were outlined in Chapter 3.

The ultimate limit on the speed of this system will be set by the lifetime of the

atomic state used which in this case is 0.8 µs. Once an atom absorbs a THz photon it will remain in the THz-coupled excited state for an average of 0.8 µs before it decays back to the ground state, during which time the atom is not sensitive to any further incoming THz photons. This essentially sets the 'relaxation time' of the system; any changes in the THz field that happen over timescales less than an atomic lifetime will not be detected by most of the atoms in the vapour. While the atomic lifetime puts an upper limit on the framerate of 1 MHz, in reality we are limited by the sensitivity of the optical camera used to record the fluorescence. The FASTCAM used in this work is capable of recording at framerates of more than 10 kHz but it is not designed for low-light environments. This means that as we increase the framerate we have very few counts on the camera per frame and our signal to noise ratio is reduced to unusable levels. We recorded THz videos up to framerates of 6 kHz but at this speed our effective SNR was only 2.

6.3.3   Sensitivity

We characterise the detector sensitivity by measuring the minimum detectable power (MDP); the minimum THz power at which the resulting fluorescence signal is reliably detectable above the noise. We use the Andor iXon to record a series of images both with and without the THz field for varying THz powers. As in Chapter 5 we define the signal as the pixel value resulting from fluorescence in the presence of the THz field minus that from background fluorescence in the absence of the THz field, $f_{\mathrm{on}} - f_{\mathrm{off}}$. For a typical (40×40) µm^2 pixel close to the centre of the image, this signal and its uncertainty is plotted against the incident THz power in Fig. 6.6. In order to calculate the THz power incident on a single pixel we assume that the THz beam is a perfect Gaussian, and that all the lenses are positioned at their focal lengths. To find the power incident on the light sheet we first find the power incident on the circle circumscribed around the area of the light sheet. Assuming the light sheet is a square with sides of 10.0 mm in length, this circle has radius $r = 5\sqrt{2}$ mm. For a Gaussian beam with waist ω, the fractional power P transmitted through an aperture of radius r is given by

$$P = 1 - e^{\frac{-2r^2}{\omega^2}}. \tag{6.3.4}$$
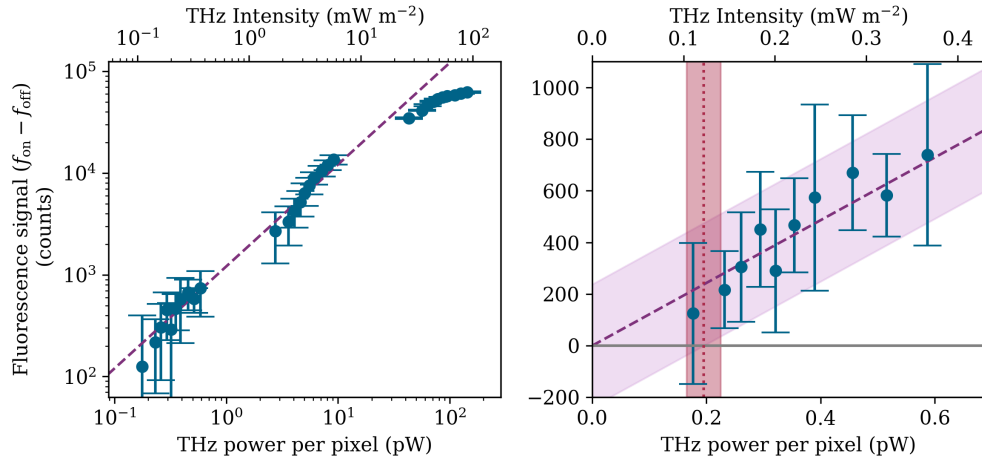
Figure 6.6: **Minimum Detectable Power.** (a) The fluorescence signal $f_{\mathrm{on}} - f_{\mathrm{off}}$ (blue circles) as a function of incident THz power for a total integration time of $1\,\mathrm{s}$. The linear trendline is extrapolated from that in (b) to highlight the saturation point at THz powers above $20\,\mathrm{pW}$ per pixel. (b) Plotting the measured fluorescence signal at low THz powers (blue circles), we can map the linear response of the system (purple dashed line) plus its associated uncertainty (purple shaded region) to the point at which the fluorescence signal is no longer reliably detectable (dotted red line), at $(190 \pm 30)\,\mathrm{fW}$ per $(40 \times 40)\,\mathrm{\mu m}^2$ pixel for a $1\,\mathrm{s}$ integration time.

Assuming that the beam has radius $11.1\,\mathrm{mm}$ (see Chapter 3) and is perfectly centred on the light sheet, we find that 55.6% of the total THz power is incident within this circle. It then follows that 63.7% of this incident power falls within the area of the light sheet. We measure the maximum output power of the THz source to be $17\,\mathrm{\mu W}$ at $0.55\,\mathrm{THz}$, from which we find that a maximum of $6.02\,\mathrm{\mu W}$ is incident over the area of the light sheet. In the images used the light sheet covers 904×904 pixels, meaning that the power incident on the area covered by each pixel is $7.37\,\mathrm{pW}$. For the image analysis the images were binned into 4×4 superpixels, increasing the maximum power per pixel by a factor of 16 to $118\,\mathrm{pW}$.

We find the system responds linearly for THz powers up to around $20\,\mathrm{pW}$ per $(40 \times 40)\,\mathrm{\mu m}^2$ pixel, as indicated by the dashed line in Fig. 6.6 (*left*). Above this power the system experiences saturation and we observe a smaller increase in signal for a given increase in THz power, seen as the deviation from the linear trend at

high THz powers. We determine the MDP by considering the signal in the region of lowest incident THz power where the response is linear, shown in Fig. 6.6 (*right*). The purple dashed line is a linear fit to the datapoints, with the uncertainty shown by the purple shaded region. From this we find an MDP of $(190 \pm 30)\,\mathrm{fW}$ per pixel for a 1 second exposure time (red dotted line and shaded region). At exposure times of over $0.5\,\mathrm{s}$ the fluorescence signal saturates the camera, so to obtain an integration time of 1 second we average over 5 frames, each with an exposure of $200\,\mathrm{ms}$. At this exposure time we are working within the shot-noise limited regime of the camera where the recorded pixel value scales linearly with exposure time, and the uncertainty is proportional to the square root of this pixel value [100]. In this way the MDP of our system scales inversely with the square root of the total integrated exposure time used, resulting in an MDP of $(190 \pm 30)\,\mathrm{fW\,s^{-1/2}}$ per $(40 \times 40)\,\mathrm{\mu m^2}$ pixel. Alternatively this MDP can be expressed as a minimum detectable THz intensity of $(0.12 \pm 0.02)\,\mathrm{mW\,m^{-2}s^{-1/2}}$.

6.3.4 Linewidth

Since the atomic transition addressed by the THz field is narrowband we expect the system to have a similarly narrowband response. We can measure the linewidth of the response in two ways, either by looking at the fluorescence on the camera through the narrowband optical filter, or by recording the entire fluorescence spectrum on the spectrometer and integrating over the filter width. To determine the linewidth of the response using the spectrometer we illuminate the atoms uniformly with the THz field and record fluorescence spectra at various values of THz detuning, as in Fig. 5.6. We then extract the total signal $(f_{\mathrm{on}} - f_{\mathrm{off}})$ within the optical filter transmission window, which in this case is $(535 \pm 6\,\mathrm{nm})$. This method is slow as each recorded spectrum requires several seconds of integration time. We repeat the procedure but instead capture the fluorescence emitted from the light sheet on the iXon camera and look at the total recorded pixel count as a function of THz detuning. This method is quicker as each shot only requires a few milliseconds of integration time. We see that both methods agree, and from this we extract a FWHM of $(14.0 \pm 0.4)\,\mathrm{MHz}$.
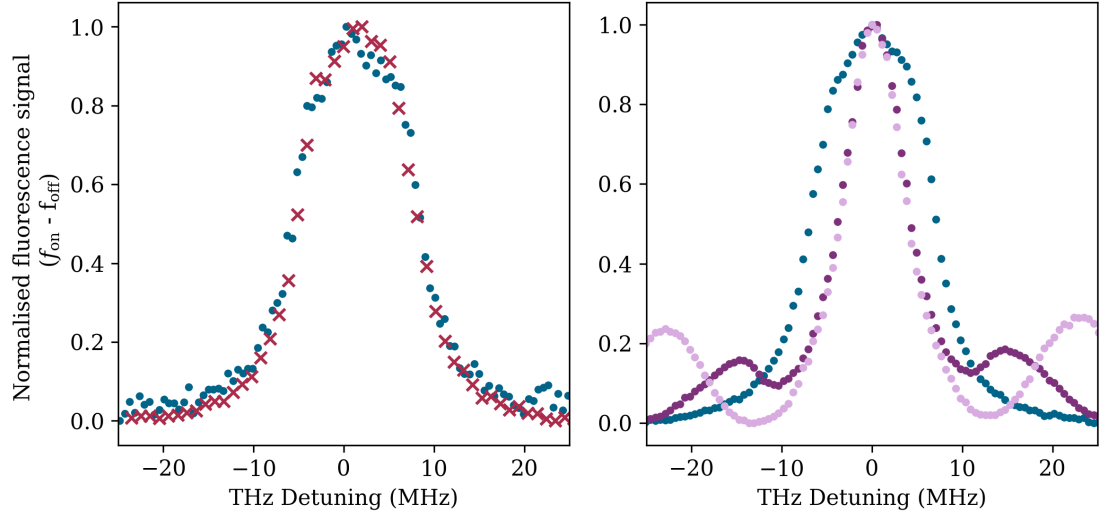
Figure 6.7: **Linewidth of the fluorescence response.** *Left:* The normalised fluorescence signal as a function of THz detuning taken with both the camera (blue dots) and spectrometer (red crosses). From this we extract a FWHM of (14.0 ± 0.4) MHz. The structure at the top likely comes from unresolved hyperfine structure. *Right:* Variation of the fluorescence response lineshape with magnetic field. The data show the fluorescence as a function of THz detuning for low (dark purple) and high (light purple) applied magnetic fields. The blue dots show the lineshape in standard operating conditions with no applied field. Note that each dataset has been individually normalised.

There is structure seen around zero THz detuning for both the data taken with the camera and spectrometer, indicating it is a real feature and not an effect caused by the method of data acquisition. This could result from unresolved hyperfine structure of the Rydberg state. To investigate this further a magnetic field was applied to the vapour cell and the measurements repeated (Fig. 6.7, *right*). To vary the magnetic field seen by the atoms a weak permanent magnet was placed at two different distances away from the cell. Although the absolute size of the magnetic field applied was not measured, we clearly see that the increasing field changes the feature from a single peak into three separately resolved peaks. In the case of higher field (light purple datapoints) we see that the separation of the outer features is greater than in the lower field case (dark purple datapoints). The exact explanation behind this behaviour is unclear and more quantitative work is required to establish whether this splitting is due to Zeeman splitting of one of the states involved in the fluorescence emission. Once properly quantified this effect could provide a means with which to narrow the linewidth over which the fluorescence is observed, or to perform magnetic field sensitive measurements.

6.4   Issues Encountered

The main difficulty encountered when working with this imaging system was that of interference caused by stray THz reflections propagating back though the cell and interacting with the vapour. These reflections originated from surfaces such as the insides of the glass vapour cell itself so were impossible to eliminate entirely. These interference effects can be seen as stripes or distortions in some images. To minimise this effect the vapour cell was placed at a slight angle to the incoming THz beam so that any reflections from the cell walls would not directly interfere with the incoming beam.

When imaging using the system, the exact position of the focal plane was hard to accurately measure so the object was translated along the axis of THz propagation until the optimum position was found. Whilst doing this, the contrast in the resulting images was observed to oscillate dramatically. Figure 6.8 shows this effect
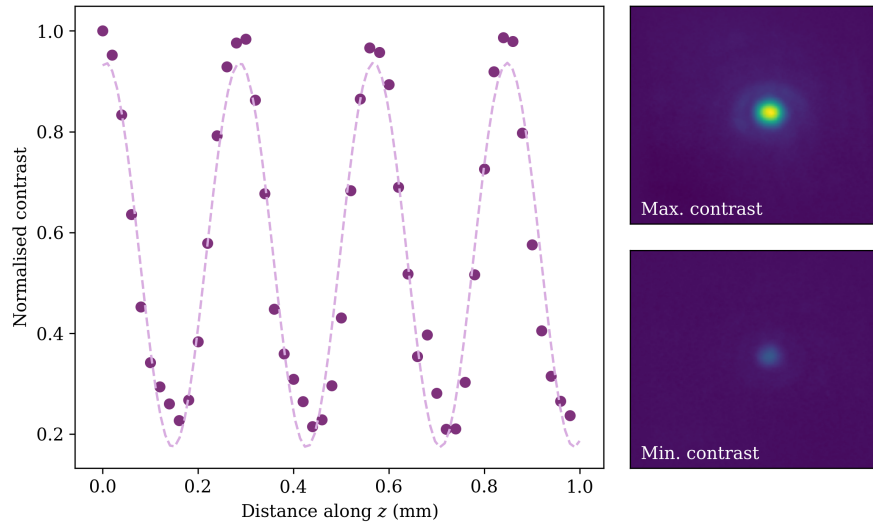
Figure 6.8: **Oscillating contrast in THz images.** *Left:* Measured contrast within an image is plotted as a function of the object's position on the z axis. The dashed line is a fit to the datapoints, giving a period of approximately $\lambda_{\mathrm{THz}}/2$. *Right:* Examples of a high contrast (*top*) and low contrast (*bottom*) image, corresponding to the first and ninth datapoint respectively.

as the single pinhole mask is translated in the z direction (along the axis of THz propagation). For each image the contrast is extracted by measuring the difference between the maximum and minimum pixel values. This contrast is then plotted as a function of object position along the z axis. Fitting a $\sin^2$-like function to these datapoints shows that the period of these oscillations is $0.28\,\mathrm{mm}$ which is approximately $\lambda_{\mathrm{THz}}/2$. This suggests that a THz standing wave is being formed somewhere in our imaging system, affecting the contrast of the images. This effect is difficult to remove as anti-reflection coatings are not commonplace for this wavelength so cannot be used on our optics. The effect was minimised by finding an object position with high contrast within the focal plane of the imaging system.

The output from the THz source is linearly polarised in the vertical (y) direction with a purity of 1:10 [68]. Normally the polarisation is not something that we need to consider when performing imaging experiments, however in certain cases it has noticeable effects. One example in which we are able to see the effect of the THz polarisation on the images is when imaging a sub-wavelength metallic slit. In Fig. 6.9

we show images of a narrow metallic slit of dimensions $200\,\mu\text{m} \times 14\,\text{mm}$ taken with the THz polarisation and slit at different orientations. In the top left and bottom right images the slit is aligned perpendicular to the polarisation of the E-field out of the THz source, and in these cases the slit is clearly visible in the images. However if either the slit or the THz source is rotated by $90°$ in the xy plane the slit is no longer imaged (top right and bottom left panels). When the slit was aligned perpendicular to the E-field we were able to observe THz transmission through slits of width $< \lambda/10$, however if the slit was aligned such that it was parallel to the E-field then we were only able to see transmission through slits of width $> \lambda/2$. Although a full investigation into this effect is beyond the scope of this thesis, we note that these observations are in agreement with previous studies [101, 102] into light transmission through sub-wavelength apertures. In these studies they state that there exists a cut-off width of $\lambda/2$ for fields polarised parallel to a narrow aperture, below which light will not propagate through the aperture. Since this size limit of $250\,\mu\text{m}$ is much smaller than the current resolution of our imaging system ($1.0\,\text{mm}$) we do not anticipate that this polarisation dependent effect will limit the quality of the images taken.

Motional Blurring Effects

Throughout this chapter we have assumed that the fluorescence emitted by the atoms gives us an exact image of the incident THz field. This assumes that the atoms do not move between absorbing a THz photon and emitting a signal photon. However since we are working in a thermal vapour this is obviously not the case; the atoms will be constantly moving within the cell. By having the excitation lasers in a counterpropagating geometry we should be performing Doppler selection to some extent in the x direction (i.e. selecting atoms with $v_x \approx 0$). This will not be the case for the y direction and hence could result in blurring of the images due to atoms moving between being excited and decaying. As seen in Chapter 2, Cs atoms in a thermal vapour will have a most probable velocity given by

$$v_p = \sqrt{\frac{2kT}{m}} \qquad\qquad (6.4.5)$$
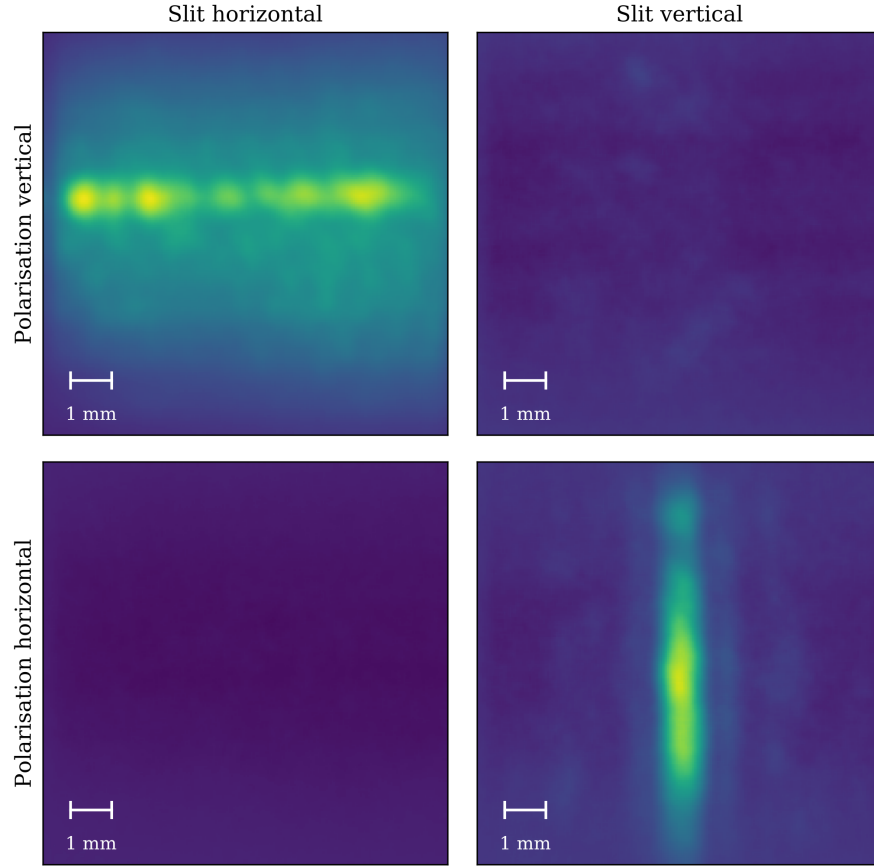
Figure 6.9: **Effects of THz polarisation on imaging.** Images of a $200\,\mu\text{m}$ wide metallic slit taken with the slit both parallel and perpendicular to the polarisation of the THz source. When the slit is perpendicular to the direction of polarisation (top left and bottom right) the slit is imaged successfully. When they are parallel the slit is not imaged (top right and bottom left).

where k is the Boltzmann constant, T is the temperature of the ensemble in Kelvin and m is the mass of a Cs atom. At our usual operating temperature of $60\,°\text{C}$ $v_p \approx 200\,\text{ms}^{-1}$. For the THz transition used here $(14\text{P}_{3/2} \rightarrow 13\text{D}_{5/2})$, our signal photons come from the $13\text{D}_{5/2} \rightarrow 6\text{P}_{3/2}$ decay which has a spontaneous transition rate of $6.8 \times 10^5\,\text{s}^{-1}$. This allows us to estimate that an atom will travel an average distance of $300\,\mu\text{m}$ between absorbing a THz photon and emitting a signal photon. While this distance is smaller than our current resolution limit of $1.0\,\text{mm}$ it is of the same order of magnitude, and due to the distributions of both the speed and the lifetime across different atoms there may be a significant number of higher speed or

longer lived atoms that travel much further between absorbing a THz photon and emitting a signal photon, thus leading to greater image blurring than in the average case. In order to ascertain at what point this 'motional blurring' effect will limit our resolution we perform Monte-Carlo simulations of the 2D sheet of atoms used to form the THz image. In the simulation we look at a worst case scenario, one in which we have no Doppler selection so the atoms have both horizontal and vertical velocity components. We do not however consider the z component of the velocity, for simplicity we adopt a 2D approach. The atoms are initialised in an ideal 2D 'image' and the simulation is run for 10 atomic lifetimes at which point most of the atoms have decayed. The v_x and v_y velocity components of each atom are chosen at random from a Maxwell-Boltzmann distribution of velocities and the time to decay is determined by comparison of the atomic lifetime to a random number. For simplicity we make a number of assumptions in this model; we constrain the atoms to remain within the $10\,\mathrm{mm} \times 10\,\mathrm{mm}$ imaging area throughout the simulation, if they reach the boundary they are assumed to undergo perfect elastic collisions with the cell wall which do not alter the state of the atom. We also assume that after the initialisation we have switched off all driving fields so that once an atom has decayed it cannot be re-excited and emit a second signal photon.

The left-hand panel of Figure 6.10 shows an example of an ideal image of a grid of sharp lines, each of width $0.5\,\mathrm{mm}$ which corresponds to a spatial frequency of 1 line pair per millimetre (lppmm). The right-hand panel shows the resulting image after the atomic motion simulation for a vapour at $60\,°\mathrm{C}$ and an atomic lifetime of $1.5\,\mathrm{\mu s}$. This feature size was chosen to be just below the limit of our current imaging resolution and the lifetime is the reciprocal of the $13\mathrm{D}_{5/2} \rightarrow 6\mathrm{P}_{3/2}$ transition rate. We calculate the Michelson contrast [103]

$$c_\mathrm{M} = \frac{I_\mathrm{max} - I_\mathrm{min}}{I_\mathrm{max} + I_\mathrm{min}}, \qquad (6.4.6)$$

where $I_\mathrm{max,min}$ are the maximum and minimum signal values respectively. At this lifetime and feature size we see that the contrast is reduced slightly to 0.96 and the sharp features at the edges of the bars become rounded. This indicates that at this spatial frequency and atomic lifetime motional blurring does not limit the resolution of the system.
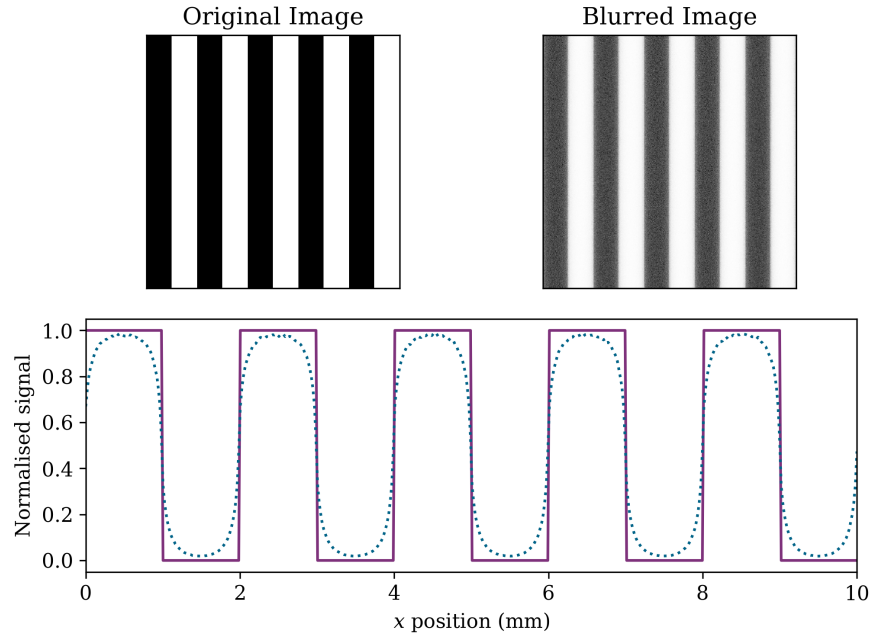
Figure 6.10: **Simulation of blurring due to atomic motion.** Top left and right are examples of an ideal image before the simulation and the resulting image after the blurring simulation. Each bright/dark strip is 0.5 mm wide corresponding to a spatial frequency of 1 line pair per mm. The lower plot shows the result of summing the pixels in the vertical direction, showing the effect that the blurring has on both the amplitude and shape of the features in the image. The resulting Michelson contrast here is 0.96 indicating that motional blurring should not limit imaging of objects this size.

We can use this simulation to predict the effects of motional blurring for different imaging parameters. Figure 6.11 shows the simulated contrast for a range of spatial frequencies and atomic lifetimes. The results of the simulation indicate that for our current atomic lifetime of 1.5 μs our contrast will be reduced by half for spatial frequencies higher than 3 line pairs per mm, limiting the ability to image features smaller than 0.2 mm in size. Since this is well below the resolution limit set by our current wavelength and lens system, motional blurring was not considered to be an issue. However future experiments and applications may rely on imaging at higher THz frequencies at which point the shorter wavelength may mean that motional blurring must be taken into account. For example if we wish to image at 1.1 THz

using the $12P_{3/2} \rightarrow 11D_{5/2}$ transition the lifetime is reduced by approximately half, so our motion-limited resolution will be improved.
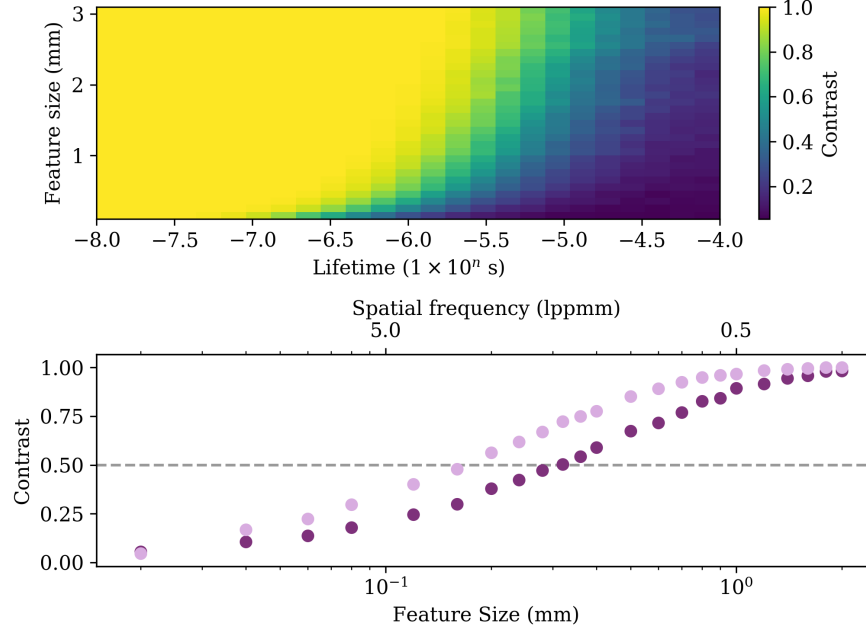
Figure 6.11: **Predicting contrast from motional blurring simulation.** *Top:* Image contrast as a function of feature size and atomic lifetime for a vapour temperature of 60 °C. *Bottom:* Contrast as a function of feature size and spatial frequency for an atomic lifetime equal to 1.5 µs (dark purple), equivalent to that in our current system. The contrast drops below 0.5 for spatial frequencies higher than 3.0 lppmm, indicating motional blurring will impact our ability to image features smaller than 300 µm. For a lifetime of 0.8 µs (light purple) the contrast drops below 0.5 for features smaller than 160 µm.

6.5   Future Improvements

Despite already demonstrating significant improvements in speed and sensitivity over other THz imaging systems, many relatively simple adjustments could be made to improve performance further. For example, image quality could be improved by reducing the interference patterns caused by reflections of the THz field within the cell through making the cell thinner (<200 µm) and adding a THz anti-reflection coating.

Furthermore, the image resolution could be increased by using a more sophisticated THz lens system, or by imaging using higher THz frequencies through the choice of an appropriate atomic transition from the wide range available [51]. Using the model developed in Chapter 5 we can easily predict which transitions will be good for imaging at higher THz frequencies. We have identified the $12P_{3/2} \rightarrow 11D_{5/2}$ transition at 1.1 THz as a good candidate for imaging and anticipate that the use of a higher frequency (and hence a shorter wavelength) will increase our spatial resolution. The THz sensor area could be extended by using a larger vapour cell to enable formation of a larger sheet of excited atoms, however increased laser powers would be required to maintain laser beam intensity over a larger area. We noted earlier that the response time of this system is ultimately limited by the lifetime of the atomic state used, which here is 0.80 µs. Using exposure times of this order of magnitude would mean the majority of atoms had not decayed from the previous frame and hence a rapidly changing field would not be imprinted into optical fluorescence. Our full-field approach enables the system to be used for capturing high-speed video of THz fields, potentially up to MHz frame rates with a suitable optical camera. As the Photron high-speed camera currently used is not designed for low-light applications, we are limited in this work to frame rates less than 4 kHz; a more sensitive camera would increase the maximum frame rate of the system. We estimate that only 0.4% of the emitted fluorescence is collected by the current 1 inch lens on the camera, therefore a larger optical lens allowing for greater collection efficiency would also allow for increased frame rates. The wide range of THz frequency transitions within caesium and other alkali metal atoms means that this system could be extended to operate at multiple THz frequencies simultaneously, allowing for 'multicoloured' THz imaging. This could enable spectroscopic information to be collected about a sample alongside transmission images.

6.6   Reflection Mode Imaging

All of the work described thus far has been performed in transmission mode, where the THz field passes through an object and the resulting transmitted field is imaged
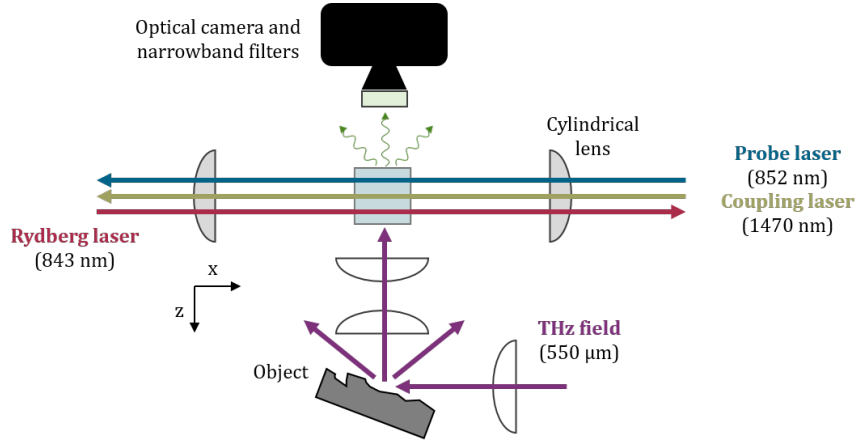
Figure 6.12: **Experimental layout for reflection mode imaging.** The colli-
mated THz field is now incident on the target object at an angle and the diffuse
scatter is imaged onto the atomic vapour through Teflon lenses. The optical camera
captures the fluorescence from the vapour from the opposite side to which the THz
is incident.

onto the vapour. For some applications however it would be more useful to image
the THz field scattered from the surface of an object. We will refer to this as
reflection mode imaging. Figure 6.12 shows the changes made to the experimental
layout in order to capture images in reflection mode. The THz beam is now incident
on the object at an angle after passing through a collimating Teflon lens. The
diffuse scatter of the THz field from the surface of the object is then imaged onto
the light sheet. Again images of the optical fluorescence are captured from the
opposite side of the vapour cell to which the THz beam is incident. Proof of principle
demonstrations of imaging in reflection mode were performed with our system, and
we show that we are able to detect small amounts of THz light scattered in a diffuse
way from textured surfaces. Figure 6.13 shows two examples of objects and their
THz reflection images; Fig 6.13(a) shows optical (*left*) and THz (*right*) images of an
embossed plastic grid, while Fig. 6.13(b) shows the threaded part of an M6 bolt. In
both cases the raised parts of the objects appear brighter than the recessed sections
in the THz images. This method did prove to be technically more challenging than
transmission mode imaging for a number of reasons, hence why most of the work was
done in transmission. Not only is the alignment more difficult than in transmission
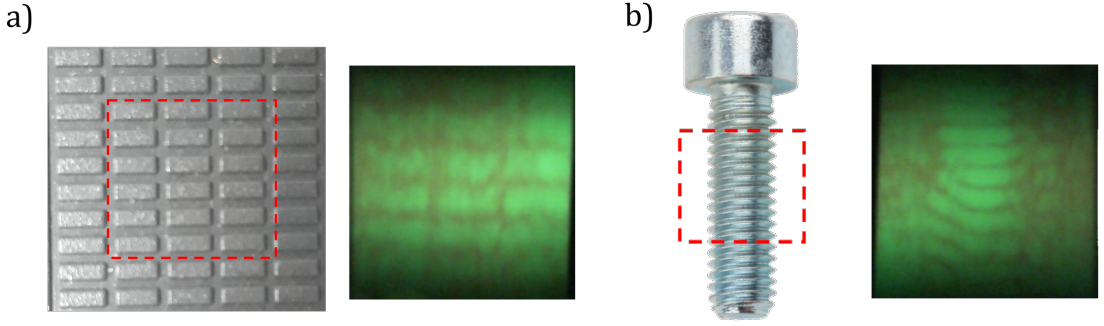
Figure 6.13: **Examples of images captured in reflection mode.** Optical (*left*) and THz (*right*) images of (a) an embossed plastic grid, and (b) the thread of an M6 bolt captured in reflection mode. In both cases the raised sections appear as bright regions in the THz images. The red dashed squares on the optical images indicate the area shown in the THz image.

mode, more THz power is needed as much of the scattered field is lost before it can interact with the vapour. The depth of field of the THz lens system is very shallow, so features are only imaged from a single plane. This limits the usefulness as objects with a more complex 3D structure are not fully captured.

6.7 Conclusion

In this chapter we outlined how we make use of the principle of THz-to-optical conversion in an atomic vapour to perform 2D THz imaging at unprecedented speeds. We detailed methods used to characterise our imaging system and showed that for our $1\,\mathrm{cm}^2$ sensor we have a $1.0\,\mathrm{mm}$ spatial resolution and the ability to capture video at 3000 frames per second. We measured a FWHM linewidth of $(14.0 \pm 0.4)\,\mathrm{MHz}$ and determined the minimum THz intensity detectable by the system to be $(0.12 \pm 0.02)\,\mathrm{mW\,m^{-2}s^{-1/2}}$. We also explored some of the issues encountered in working with this imaging system such as THz interference and blurring due to the motion of the atoms. We briefly demonstrated imaging in reflection mode as opposed to transmission mode which may be more useful for certain applications. Whilst we highlighted simple modifications which could be made to improve the

performance of the system, the figures of merit reported here have enabled THz imaging of dynamical processes at rates not previously possible by any other method. We predict that the versatility and sensitivity of this atom-based THz imaging technique will produce a disruptive impact on fields as diverse as biological imaging and production-line quality control [26, 27, 30].

Chapter 7

Applications of THz Imaging

In this chapter we detail some proof-of-principle experiments performed to showcase the potential real-world applications of our atom-based THz imaging technique. While not all of the experiments described here directly take advantage of the speed of the system, they are meant as a first demonstration of the types of things that this system could be used for. They focus mostly on non-destructive testing (NDT) applications in manufacturing and food processing.

7.1 Introduction

THz imaging has the potential to be useful in a wide range of practical applications [26]. Its ability to pass through many dielectric materials means it is of interest on production lines as a method of performing non-destructive testing (NDT) of products [104, 105]. For example it is of interest for the inspection of wind turbine blades [106] and functional coatings [99]. High-resolution THz imaging has also previously been used to identify counterfeit integrated circuits [107]. One area that would benefit from the commercialisation of THz imaging is the food processing industry [108, 109], with applications ranging from contaminant detection and package integrity inspection to water content monitoring. However the current low rate of image acquisition is often cited as a barrier to the uptake of THz imaging technology in this area.

7.2 Beam Profiling

The spatial output of many THz sources, particularly quantum cascade lasers, can be highly irregular and hard to estimate without direct measurement [110, 111]. There are ongoing efforts to find ways of making the emission more uniform which requires the ability to image the far-field intensity of the beam. Currently these studies are performed using imaging techniques that are far from real-time such as systems employing Golay cells [112] or pyroelectric detectors [113]. We can take advantage of the real-time nature of our imaging system and use it as a THz beam profiling camera to look at the shape of the THz beam as it propagates through beam-shaping elements such as lenses. Many of the beam-shaping optics used in the THz frequency range are very basic and are not optimised to reduce aberration in the same way as optical elements for the visible and IR bands. Since optical elements for use in the THz frequency range can be 3D printed [114, 115] or machined from materials such as Teflon they can be designed and manufactured in-house. While this opens an avenue to a wide range of possibilities, any newly made optical designs need to be carefully characterised to ensure they are performing as expected. The atom-based THz imaging system described in the previous chapter enables us to easily characterise optical elements produced in-house.

Figure 7.1 shows an example of using our imaging system to examine the effect of a small (1" diameter) almost hemispherical Teflon lens on the THz beam and identify any aberrations. The lens was illuminated with a collimated THz beam and translated in the z direction thus changing the distance between the lens and the plane of the atoms used in imaging. The images clearly show a bright central spot surrounded by rings whose size and intensity change with the distance z. This indicates that the small lens induces spherical aberration [66][pg. 99]. The vertical fringes in the images are as a result of interference between the forward propagating THz field and its reflection from the inner wall of the vapour cell.

If a cross-section of each of the images shown in Figure 7.1 is plotted as a function of lens position we see the evolution of the propagating THz field. As can be seen in Figure 7.2 the lens has a short focal length ($\approx 20\,\mathrm{mm}$ from the plane surface). We also see fringing and interference effects downstream of the lens, possibly due to

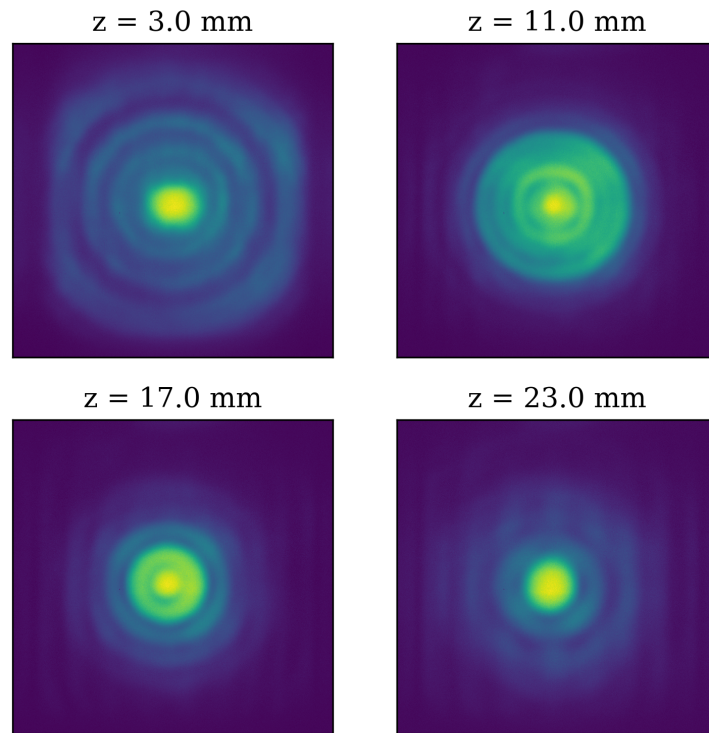Figure 7.1: **THz beam shape after a small Teflon lens.** Images of the THz field after passing through a small (1" diameter) hemispherical Teflon lens at varying distances along the propagation direction. The images show a central brighter focal spot surrounded by rings, indicative of spherical aberration. The vertical stripes seen in the images are a result of interference between the forward-propagating and reflected THz field.
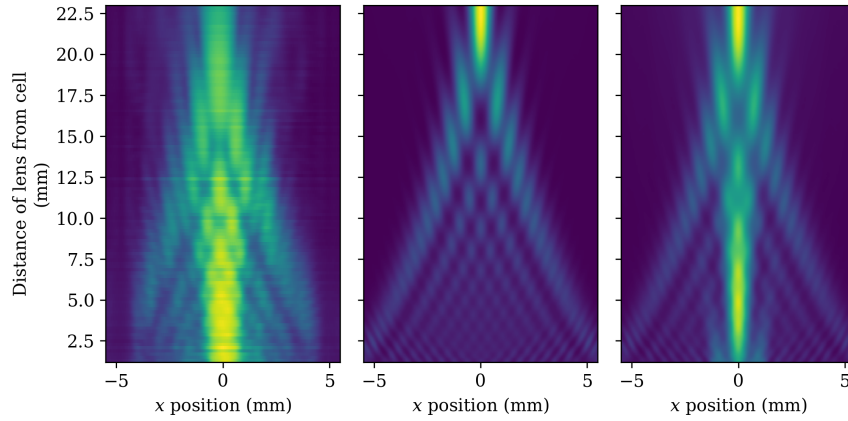
Figure 7.2: **Characterisation of a small Teflon lens.** Data (*left*) and simulations (*centre & right*) of the amplitude of the THz field downstream of a 1" diameter Teflon lens. The simulation shown in the central panel neglects any reflections of the THz field within the cell and is clearly not a good visual match to the data. In the simulation shown in the right hand panel this back-reflection is included, resulting in an image that more closely resembles the data. Note that the measured profiles are truncated at $x = \pm 5\,\text{mm}$ due to the walls of the glass vapour cell.

the THz beam being 'clipped' by the edges of the lens which causes diffraction rings to form around the central spot. These rings change in intensity and radius as the lens is moved. In order to understand to what extent these effects and aberrations are due to the characteristics of the lens we perform a simulation of the THz field propagating through a lens with the same dimensions and compare the results to our measured beam profiles. The simulation is a simple Fourier propagation model using the angular spectrum method [66], the results of which are plotted in the central and right-hand panels of Figure 7.2. In the simulation plotted in the central panel we have neglected any reflection of the THz field from the walls of the vapour cell. It is clear that this does not reproduce what we see in the measured profiles. If we assume that 50% of the THz field is reflected off the wall within the vapour cell (as in the simulation shown in the right-hand panel of Figure 7.2) then the simulation more closely resembles what we see in the data. The fringes that we see in our recorded THz images match those seen in the simple model, indicating that they are due to the characteristics of the lens and not to do with our method of

THz imaging. The recorded focus of the THz beam does appear to be larger than the simulation would suggest, and the cause of this discrepancy is not identified.

7.3   Food Production Monitoring

One major sector in which there is potential for THz imaging systems to be implemented is in food production and processing [108,109]. Currently quality monitoring is done offline as it is slow, so a high-speed imaging system has the potential to be integrated into existing production lines and reduce costly waste due to failed quality checks [116]. Unfortunately it is hard to gather many details of testing methods currently in use as companies are reluctant to reveal this kind of information. While THz imaging will only ever be useful for products with a low water content there is still plenty of scope within this area for it to be a valuable tool. Previous studies have demonstrated the ability of CW THz imaging to inspect dry food products such as chocolate and nuts [117–119] but even those described as high-speed provide very limited time resolution. While some commercial line-scanning THz imaging systems [120] offer speeds of up to 5000 lines per second, their spatial resolution is too low ($> 1\,\mathrm{mm}$) to be of use in many food-based applications. There is still a considerable gap in the market for a high-speed high-resolution THz imaging system.

7.3.1   Safety

There have been many reported incidents of non-metallic contaminants (e.g. glass fragments) being concealed within food products which have then been distributed to customers. This obviously has the potential to cause harm so is an eventuality that companies are keen to avoid [121]. For example in early 2016 Mars had to recall products due to contamination with plastic, leading to an estimated cost of £1.8m in lack of sales [122]. A brief look at the Food Standards Agency (FSA) 'Food Alerts' webpage [123] reveals 10 cases of product recalls due to foreign body contamination in the UK in the first 6 months of 2020, one of which again involved Mars' products. Currently used systems include metal detectors, optical camera systems, magnetic resonance imaging, ultrasound and X-rays [124]. X-ray and metal detectors are the
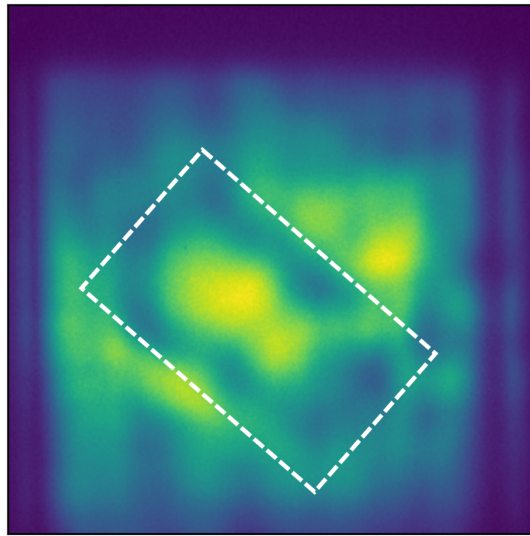
Figure 7.3: **Detection of Teflon fragment within chocolate.** A THz image of a piece of milk chocolate, within which a $1\,\text{mm} \times 2\,\text{mm}$ Teflon fragment has been embedded. The boundary of the Teflon fragment, highlighted by the white dashed line, can be seen in the THz image despite not being visible on the surface of the chocolate.

most commonly used online methods of foreign body detection in food production, but they are by no means ideal solutions [121, 125]. The obvious issue with metal detection systems is that they can only ever identify metal contaminants so glass, plastic and other non-metallic hazards can go undetected. X-ray inspection can identify a variety of physical contaminants including metal, glass, rubber, stone and some plastics, but systems carry the inherent increased risks associated with the need for high voltages to generate X-rays. X-ray inspection systems also have difficulty in detecting and imaging certain low-density contaminants including paper, cardboard, low density plastics and stone.

To demonstrate how THz imaging could be implemented to identify foreign bodies in foods we embedded a small fragment of Teflon ($1\,\text{mm} \times 1\,\text{mm} \times 2\,\text{mm}$) in a piece of milk chocolate of approximate dimensions $30\,\text{mm} \times 20\,\text{mm} \times 10\,\text{mm}$. The Teflon was placed into the melted chocolate which was then allowed to set such that the Teflon was not visible on the surface of the chocolate. Since chocolate has a relatively low water content it is almost transparent to THz radiation [126]. This

allows any foreign bodies to be easily detected in transmission imaging mode, including non-metallic ones, providing they have a different refractive index to that of the chocolate. Figure 7.3 shows a THz image of the small piece of Teflon within the block of chocolate. The edges of the Teflon fragment are clearly visible in the centre of the image, allowing it to be located within the larger chocolate block.

7.3.2   Product Quality

Products within visibly opaque packages are hard to assess for quality and damage, but companies are keen to ensure that their product reaches customers in optimum condition. For instance in the pharmaceutical industry tablet size and uniformity is of the utmost importance [127]. To this end we demonstrate using our THz imaging system to identify a damaged sweetener tablet from within its paper packet. Since the area of interest is larger than our imaging area the object was manually translated in the xy-plane and the individual images combined in post-processing to make a larger image. Figure 7.4 shows optical (*left*) and THz images (*right*) of two sweetener tablets within visibly opaque paper packets. From the optical image it is impossible to identify any difference between the two samples. However from the THz images it is clear that the tablet in the top packet is whole and undamaged as it appears as a dark circular region approximately 5 mm in diameter on the THz image. The tablet in the lower packet has been crushed so no longer appears as a uniform circle, instead appearing as a powder that has fallen to the corner of the packet. Note that since the area of interest was larger than the sensor size of our THz imaging system (1 cm^2) the object was translated in the imaging plane and multiple images taken. The periodic lines in the THz images presented here are from the way these multiple images were combined after capture and are not real features in the THz field. This technique could also be used to detect whether a packet site was empty, for example in inspections of tablets in blister packs in the pharmaceutical industry. It is not useful however if the product is packaged entirely in a material that is opaque to THz radiation such as metal foil.
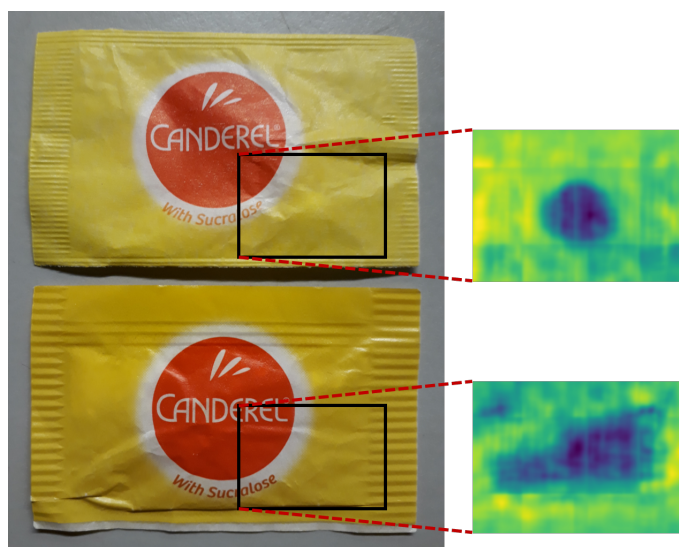
Figure 7.4: **THz imaging for product quality control.** The optical image (*left*) shows two similar opaque paper packets containing sweetener tablets, the insets (*right*) show areas of the packets that have been imaged using our THz imaging system. The sweetener within the paper can be seen as darker regions on the THz images. The upper image shows a whole sweetener tablet of around 5 mm in diameter, while the bottom image shows little structure indicating that the tablet has been crushed within the packet. This is not easily discernible from the packets' exterior.

Figure 7.5: **Inspection of printed circuit boards (PCBs).** Optical *(left)* and THz images *(right)* of copper tracks in a custom PCB. The digits are all 4 mm high with 0.5 mm thick lettering. The copper tracks are visible as darker regions in the THz images when imaged through the surrounding resin board.

7.4   Other NDT Applications

THz imaging could also be applied to non-destructive testing in other manufacturing and processing areas to assess quality and detect faults. For example it is of interest for the detection of voids and cracks in composite materials used in the aerospace industry and for the inspection of paint and other functional coatings [99]. High-resolution THz imaging has been used to image the insides of microprocessors and integrated circuits [98,107] since THz passes freely though the outer insulating plastic. Similarly THz could be used to inspect tracks of printed circuit boards (PCBs) for damage. Figure 7.5 shows an optical image (left) and THz images (right) of sections of a custom-made PCB with tracks laid in the shape of numbers. While the tracks are visible in the optical image as regions of a slightly lighter colour, they are not visible from the other side of the PCB. In the THz images the 0.0356 mm thick copper tracks (in the shape of the digits 1, 2 and 3) are easily imaged through the 1.6 mm thick resin core (KB-6167F) and appear as darker regions in the THz image. Again, whilst this demonstration did not directly take advantage of the speed of our system, it is trivial to see how this could be implemented in a high-speed production line. At our current resolution it is not possible to identify any small defects in the tracks, but we anticipate that with improved resolution imperfections could be identified.
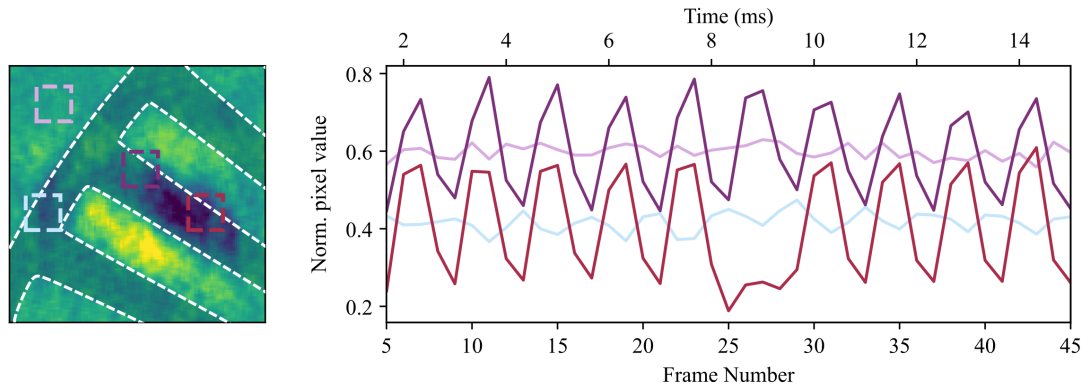
Figure 7.6: **High-speed defect identification.** A chopper wheel rotating at 750 rpm is imaged at a frame rate of 3 kHz. The left-hand image shows an example frame with the shape of the wheel added as a guide to the eye. In this image we identify 4 regions of interest, outlined by the 4 coloured squares. For each frame we average over these regions of interest and look at the time evolution of the values (*right*). From this we can see that a defect occurs between frames 25 and 30.

7.4.1   High-Speed NDT

To briefly demonstrate the ability of the system to identify defects at high speeds, we use the example of imaging an optical chopper wheel with 60 spokes rotating at 750 rpm (similar to that in Figure 6.5). Between two spokes of the wheel we attach a piece of metal foil which extends from the centre of the wheel almost to the outer edge. The left hand panel of Figure 7.6 shows an example frame from the recording, taken at 3000 frames per second. In this image we identify 4 regions of interest, as indicated by the dashed squares. For each of these regions we plot the evolution of the average pixel value over time, as in the right hand panel of Figure 7.6. For the regions located on the edge and outside of the wheel (light blue and light purple respectively) we see little change in the pixel value between frames. However for the regions located along a spoke of the wheel the pixel values oscillate as the wheel rotates. The period of these oscillations is 1.3 ms which is consistent with a wheel of 60 spokes rotating at 750 rpm. However between frames 25 and 30 we see that the periodicity of these oscillations is interrupted for the region of interest close to the centre of the wheel (defined by the red square). This is caused by the piece of
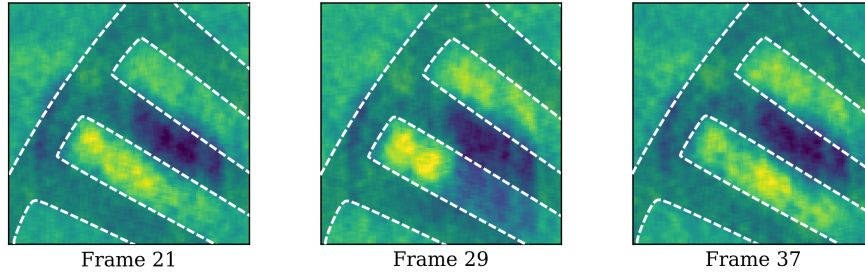
Figure 7.7: **Identifying defects in an optical chopper wheel.** Example frames from a 3 kHz video of an optical chopper wheel rotating at 750 rpm. An outline of the shape of the wheel has been added as a guide to the eye. In the left and right images the gaps between the spokes are clear, as indicated by the bright regions. In the central image however there is a dark region between the spokes, indicating the presence of the metal foil.

foil breaking the rotational symmetry of the wheel. Figure 7.7 shows some example frames from around the point at which the defect was identified. Inspecting these frames allows us to clearly see the piece of metal foil between the spokes extending outwards from the centre of the wheel. This is seen as the dark region between the spokes in the central panel of Figure 7.7 (Frame 29). While this is a trivial example, it indicates the potential of this system for fault finding on high-speed production lines. While a single-point detector would be able to identify the change in periodicity it would not enable this analysis to be performed for multiple regions of interest simultaneously.

7.5   Conclusion

In this chapter we have presented examples of proof-of-principle experiments designed to highlight the usefulness of THz imaging in a variety of settings. These demonstrations included identifying the location of a foreign bodies in food and imaging the copper tracks in PCBs. We also showed how our system could be used as a THz beam profiling tool to characterise the effect of optics on the THz field. This application will be important in the next chapter when we design and

characterise Teflon phase plates for creating THz vortex beams. While the studies presented in this chapter were qualitative more than quantitative, they have succeeded in capturing the interest of companies from different sectors with a view to developing this technology further. The ultimate aim would be to produce a compact turn-key system that could easily be integrated into a wide variety of industrial sectors and settings.

Chapter 8

Characterisation of THz Vortex Beams Created Using Spiral Phase Plates

In this chapter we demonstrate the use of phase plates to create arbitrary THz vortex beams with both azimuthal l and radial phase p. We image the resulting intensity patterns using the atomic THz imaging system described in Chapter 6. We characterise the beams by imaging their intensity after passing through a plano-convex lens oriented both parallel and tilted with respect to the phase plate. This allows us to directly ascertain both the sign and magnitude of the azimuthal phase. We also show that while these beams are similar to Laguerre-Gauss beams they behave in subtly different ways.

8.1 Introduction

There is growing interest in using THz radiation for short-range free-space communication networks due to its inherent high frequency and ability to pass through common construction materials. One way of encoding information into free-space beams is to make use of beams with helical wavefronts, so-called 'vortex beams' [128]. These vortex beams carry orbital angular momentum (OAM) equal to $\hbar l$ per photon where l is referred to as the topological charge of the beam. Since there are theo-

retically an infinite number of OAM eigenstates available, this allows the possibility of base-N encoding per photon. There have also been studies suggesting that these modes are more resistant to turbulence [129] which is an important consideration for any practical free-space communications network. The usage of THz vortex beams for communications relies on the ability to both create and read-out a beam with unique topological charge reliably and at high speeds.

Previous works have created THz vortex beams by using spiral phase-plates [130,131], helical axicons [132], V-shaped antenna structures [133], polarizing optical elements [134] and THz spatial light modulators [135]. Static optical elements such as phase plates and helical axicons present a relatively easy way to create and manipulate arbitrary THz vortex beams. The comparatively long wavelengths of the THz frequency range (between $0.1\,\mathrm{mm}$ and $1\,\mathrm{mm}$) means that elements can be fabricated from materials such as Teflon or Tsurupica using standard workshop CNC milling machines since the precision of these machines enables the creation of sub-wavelength structures. High-resolution 3D printing also offers the ability to create these static elements in the THz range [132]. This eliminates the need for the more challenging etching or lithography techniques used to create phase plates for optical wavelengths [136].

Often beams carrying OAM are interpreted in terms of Laguerre-Gauss (LG) modes. These are a series of eigenmodes of the paraxial Helmholtz equation with complex field amplitude u described by [137]

$$
\begin{aligned}
u_{pl}(r,\phi,z) = &\frac{C}{(1+z^2/z_R^2)}^{1/2} \left(\frac{r\sqrt{2}}{\omega(z)}\right)^l L_p^l\left(2\frac{r^2}{\omega(z)^2}\right)\exp\left(-\frac{r^2}{\omega(z)^2}\right) \\
&\times \exp(-il\phi)\exp\left(\frac{-ikr^2z}{2(z^2+z_R^2)}\right)\exp\left(i(2p+l+1)\tan^{-1}(z/z_R)\right).
\end{aligned}
\tag{8.1.1}
$$

Here r and ϕ are radial and azimuthal coordinates, $\omega(z)$ is the beam radius at distance z from the beam waist, z_R is the Rayleigh range, C is a constant and $L_p^l(\dots)$ is the associated Laguerre polynomial.

From this equation we see that beams are characterised by two integer indices; the azimuthal phase (sometimes called the topological charge) l and the radial phase p. While many methods have been shown to create THz beams with azimuthal phase $l \neq 0$, no work has yet been done on creating THz beams with both $l \neq 0$ and $p \neq 0$.

This radial index could offer another orthogonal axis on which to encode information in vortex beams [138].

8.2 Phase Plate Design

The principle of a phase plate is to use a transparent material of varying thickness to impart a phase shift to a transmitted beam. The thickness of the material required to impart a 2π phase shift $h_{2\pi}$ is given by

$$h_{2\pi} = \frac{\lambda}{\Delta n} \tag{8.2.2}$$

where λ is the wavelength of the field and Δn is the change in refractive index at the material interface. Our phase plates are made from Teflon, which at the wavelength of 550 µm used in this work has a refractive index of $n = 1.44$ [67]. Hence a thickness of 1.24 mm is needed to impart a 2π phase shift to the transmitted THz field. The phase profile $\phi_{l,p}(r, \theta)$, and therefore the thickness profile required to create arbitrary vortex beams can be found by looking at the phase terms in equation 8.1.1. It is related to the radial and azimuthal coordinates of the plate (r, θ) through [139]

$$\phi_{l,p}(r, \theta) = \theta l + \pi H[-L_p^{|l|}\left(2r^2/\omega_0^2\right)] \tag{8.2.3}$$

where $H[\ldots]$ is the Heaviside step function and ω_0 is the radius of the beam incident on the phase plate which in this work is equal to 5.55 mm. Examples of the phase plates are shown in Fig. 8.1, showing both the thickness of the Teflon and the phase profile of the plate. For $p = 0$, the phase plates consist of spirals of increasing thickness with a number of azimuthal discontinuities equal to the value of l. The plates with $p \neq 0$ have radial discontinuities in addition to the azimuthal thickness gradient, the positions of which are found as the zeros of the generalised Laguerre polynomial in equation 8.2.3. For the plates with non-zero l, the sign of l imparted to the beam can be altered by rotating the phase plate such that the beam propagates in the opposite direction through the plate, thus reversing the helicity of the wavefronts.
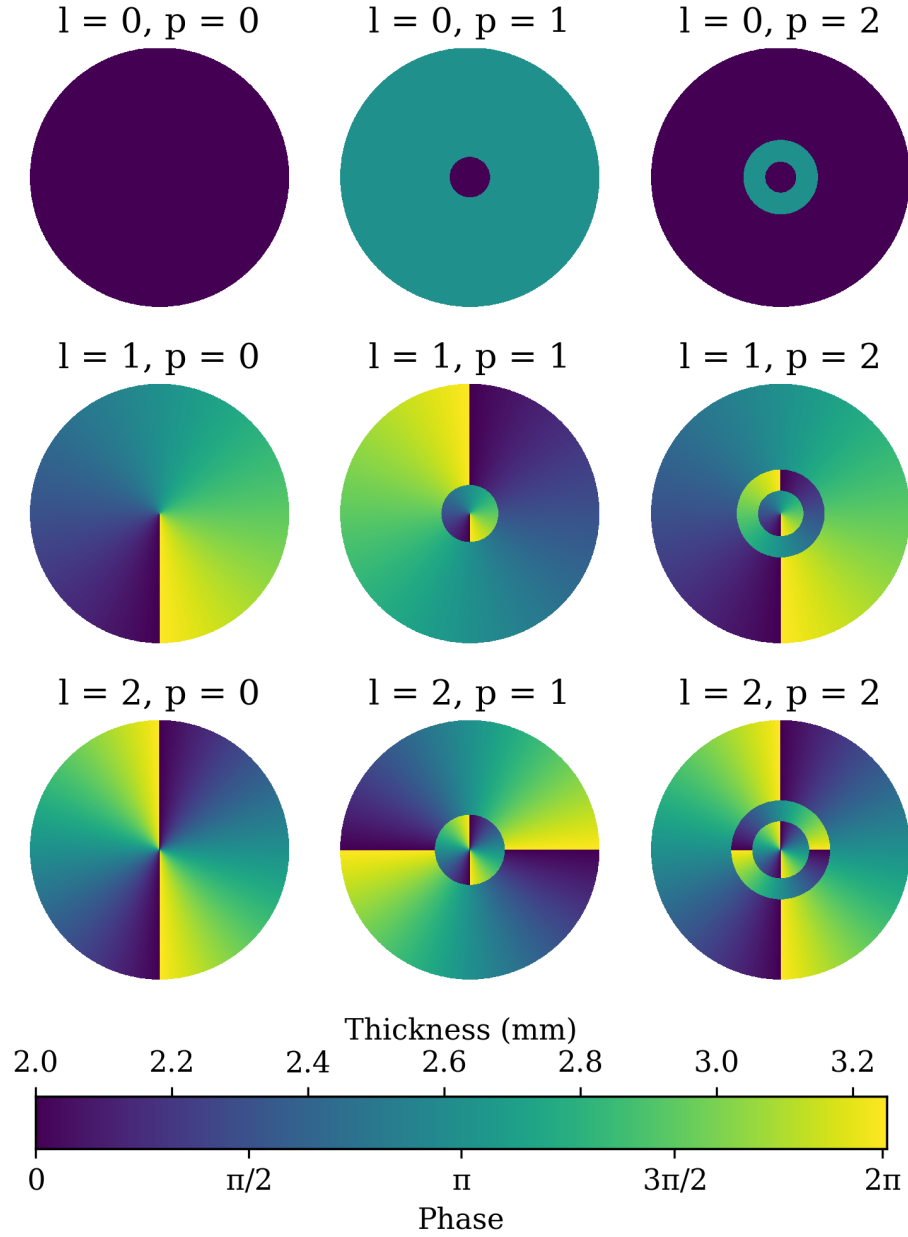
Figure 8.1: **Phase plate design for creating THz vortex beams.** The thickness (phase) profile of the 50 mm diameter Teflon plates used to create THz vortex beams, calculated using eqn. 8.2.3. The design frequency is 550 GHz, equal to that of the THz field used in the atomic imaging system. The plates for $p > 0$ are designed for a beam waist of 5.55 mm. Note that the constant minimum thickness of 2 mm is a result of manufacturing constraints and does not alter the phase profile.
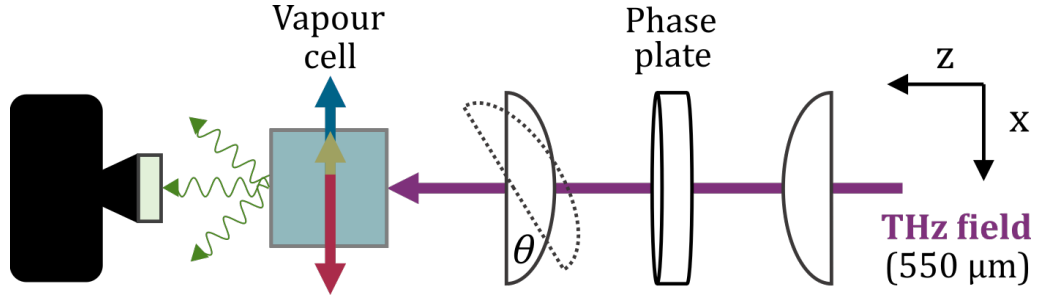
Figure 8.2: **Layout of THz optics used for creating and imaging THz vortex beams.** The experimental layout used to create THz vortex beams using spiral phase plates is similar to that used for the imaging in Chapter 6. The phase plates are placed at the centre of the collimated THz beam and focussed onto the atomic vapour using a second Teflon lens. This lens can be tilted with respect to the phase plate at an angle θ. The angle $\theta = 0°$ corresponds to the lens being parallel to the phase plate.

8.3 Imaging THz Vortex Beams

The experimental set up used to create and image the THz vortex beams is similar to that used for the imaging in Chapter 6 and is shown in Figure 8.2. The divergent THz beam passes through a Teflon lens with focal length $f = 75\,\text{mm}$ to give a collimated Gaussian beam with a $1/e^2$ radius of $\omega_0 = 5.55\,\text{mm}$. The phase plates are then placed in the centre of this collimated Gaussian beam, approximately $75\,\text{mm}$ from the first lens. The resulting beam then passes though a second $f = 75\,\text{mm}$ Teflon lens and is imaged at the focus. The final Teflon lens can be positioned parallel to the phase plate (solid lines, Fig. 8.2) or it can be tilted with respect to the phase plate (dashed lines, Fig. 8.2). We will refer to the image observed in the case of the parallel lens as the intensity pattern and the image produced by the tilted lens as the auto-interference pattern [140]. The theory behind the differences in the structure of these patterns is described in detail in [141]. In both cases the images are captured using the atom-based THz imaging system described in Chapter 6. The THz beam propagates perpendicular to the lasers used to create the light sheet and the atomic fluorescence is collected from the opposite side of the vapour cell to that on which the THz is incident.

8.3.1 Beams with $p = 0$

Images of the intensity patterns produced for beams with $p = 0$, $l = 1, 2, 3$ are shown in Fig. 8.3. The first row shows the beam intensity imaged using a lens parallel to the phase plate ($\theta = 0°$) for increasing values of l. As expected the intensity patterns for beams with $p = 0, l \neq 0$ have a 'donut-like' structure; a central vortex surrounded by a single ring, the radius of which is determined by the value of l. Since these intensity patterns are identical for $l = -l$ only the images for beams with positive values of l are shown. The lower two rows show the auto-interference patterns resulting from a lens tilt of $\theta \approx 30°$. These patterns not only display a number of dark fringes equal to the value of l, but also exhibit a 45° rotation in the imaging plane. The direction of this rotation depends on the sign of l, allowing this to be determined from the pattern. This rotation is not affected by the direction of tilt of the final Teflon lens which remained unchanged between rows two and three.

8.3.2 Beams with $p \neq 0$

Figure 8.4 shows the intensity patterns (top row) and auto-interference patterns (bottom row) for beams with $p = 1$, $l = 1, 2$ (first and second column respectively). The intensity patterns of beams with both $l \neq 0$ and $p \neq 0$ have a central vortex surrounded by a number of rings equal to $p + 1$. The radius of the rings is again determined by the value of l. Their auto-interference patterns exhibit orthogonal dark fringe patterns, with the number of fringes corresponding to the values of p and $p + |l|$ (shown in the second row of Fig. 8.4 by the white dashed and black dotted lines respectively). Again the rotation of these fringe patterns depends solely on the sign of the index l. As p increases the beams produced become larger and no longer fit within our $1\,\mathrm{cm}^2$ imaging area. As a result we see interference patterns at the edges of the image where the THz field is reflected from the walls of the glass cell containing the atomic vapour. These interference effects can be seen as vertical stripes at the edges of the images in Fig. 8.4, and is the reason why we were unable to image beams with $p > 1$ clearly.
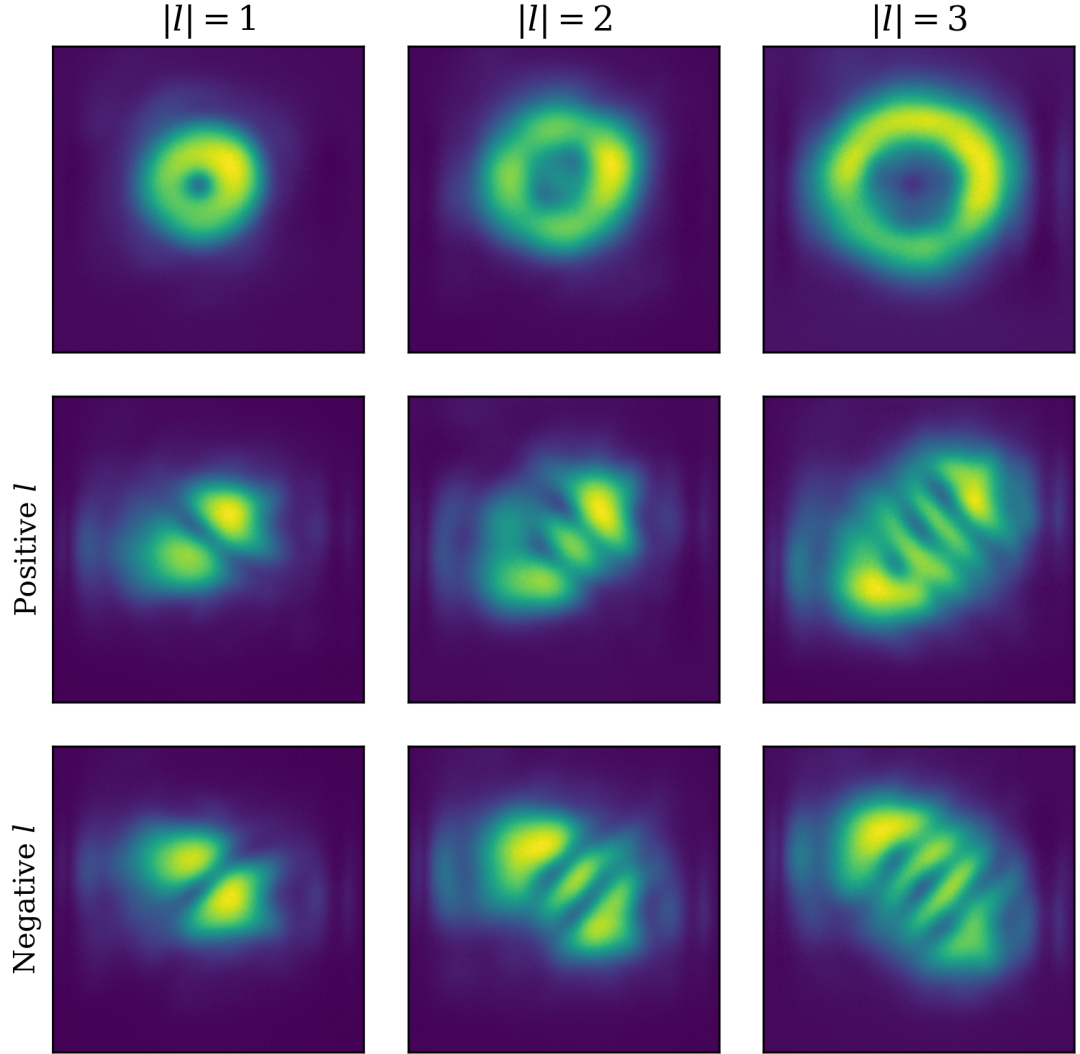
Figure 8.3: **Intensity and auto-interference patterns of THz vortex beams created using spiral phase plates.** Intensity patterns of beams with $p = 0$, $|l| = 1, 2, 3$. The top row shows the images produced when the second lens is parallel to the phase plate ($\theta = 0°$) while the second and third rows show the resulting intensity pattern for a lens tilt of $\theta \approx 30°$. Since the donut-like patterns are identical for $l = -l$, only the images for positive l are shown here. The second and third rows show the auto-interference patterns for positive and negative values of l respectively.
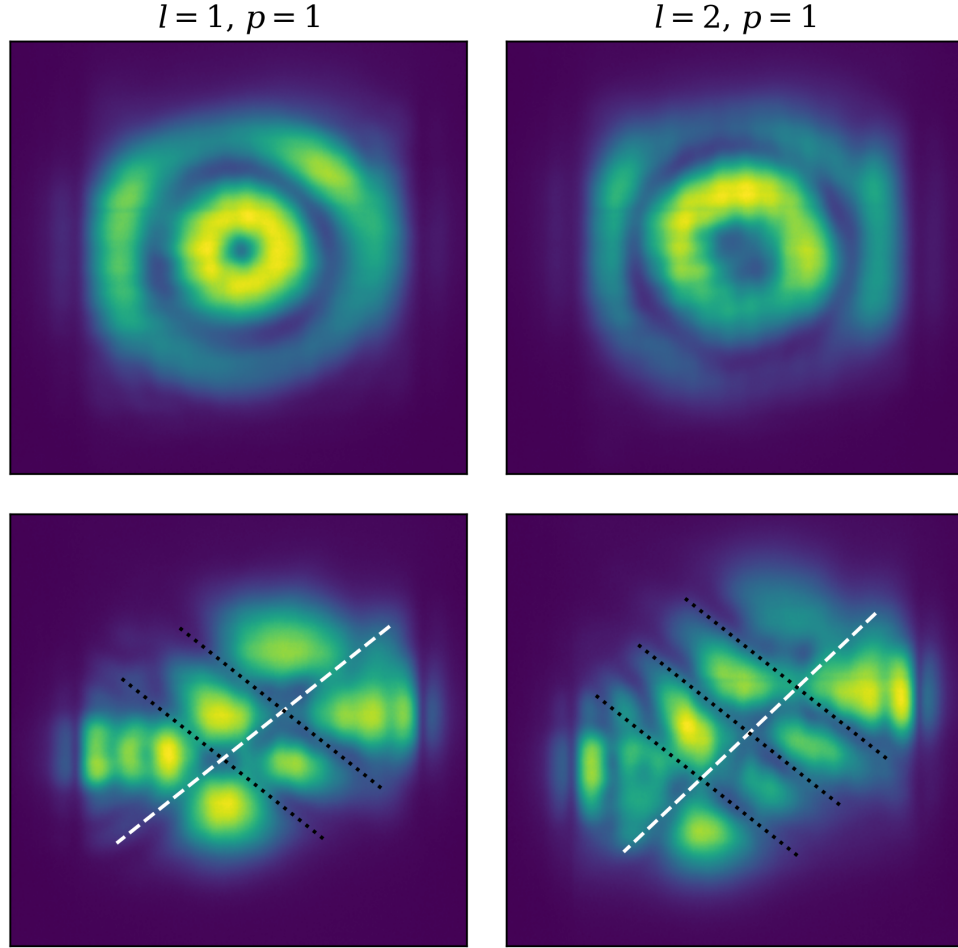
Figure 8.4: **Intensity and auto-interference patterns for beams with $l \neq 0$ and $p \neq 0$.** Intensity (top row) and auto-interference patterns (bottom row) for beams with $p = 1$, $l = 1, 2$ (left and right columns respectively). The white dashed and black dotted lines have been manually added to the auto-interference patterns to highlight the dark fringes from which we can extract the values of p and $p + |l|$. Only the auto-interference patterns for positive l values are shown here, those for negative l values would be tilted in the opposite direction with respect to the vertical.

8.3.3 Vortex Radius Scaling

In Figures 8.3 and 8.4 we see that the radius of the rings around the central vortex structure scales with the value of $|l|$. In the $p = 0$ case we can compare this measured radius to that predicted by the equation for LG beams. By setting $p = 0$ in equation 8.1.1 we can find an expression for the intensity distribution in the xy-plane I_l at a distance z along the propagation direction as [142]

$$I_l(r, \phi, z) = \frac{2}{w(z)^2 \pi |l|!} \left(\frac{\sqrt{2}r}{w(z)} \right)^{2|l|} \exp \left(-\frac{2r^2}{w(z)^2} \right). \tag{8.3.4}$$

Here r and ϕ are radial and angular coordinates, and $w(z)$ is the beam waist at position z. Note that this depends only on $|l|$ hence why the intensity patterns for l and $-l$ are identical. From this we find that the radius of maximum intensity $(r_{I_{\max}}(l))$ is given as

$$r_{I_{\max}}(l) = \sqrt{\frac{|l|}{2}} w(z) \tag{8.3.5}$$

which indicates that the radius of the ring should scale as $\sqrt{|l|}$. If we measure the radii of the intensity patterns produced by the spiral phase plates (top row, Fig. 8.3) we find that they scale linearly with $|l|$ such that $r_{I_{\max}}(l = 2) = 1.92 \times r_{I_{\max}}(l = 1)$ and $r_{I_{\max}}(l = 3) = 2.85 \times r_{I_{\max}}(l = 1)$. While this linear scaling is not what we would expect from pure LG modes, it has been observed previously in optical vortices created using spiral phase plates [143–145]. Here they find that the radius of maximum intensity scales as

$$r_{I_{\max}}(l) = a \left(1 + \frac{l}{l_0} \right) \tag{8.3.6}$$

where a and l_0 are constant factors related to characteristics of the system. This discrepancy in scaling comes about from the fact that the beams created by the phase plates are not pure LG modes but are instead a superposition of modes with different l and p. While the spiral phase plate can convert up to 78.5% of the input mode into the desired output mode [146], the fact that they do not produce pure LG modes mean that the resulting beams do not share the same scaling properties. These modified LG beams can be described as 'helical' beams as they still retain the helical wavefronts characteristic of LG beams [147]. Since it is difficult to determine

the exact composition of modes in our helical beams, we instead perform a numerical simulation to ascertain our expected intensity distribution. Since we image our beams after passing through a lens, the recorded intensity pattern will be related to the Fourier transform of the beam emerging from the phase plate. Numerical 2D fast-Fourier transforms of a Gaussian (LG_{00}) beam passing through phase plates with phase profiles given by equation 8.2.3 recovers the linear scaling of the vortex radius with l.

8.3.4   Combining Phase Plates

Because the Teflon phase plates are relatively low-loss we can combine them additively to form beams with the sum of the indices of the plates used. For example if we place the $l = 1$, $p = 0$ and the $l = 2$, $p = 0$ plates sequentially in the beam, the intensity pattern we see is equivalent to the $l = 3$, $p = 0$ case. This is shown in the left hand column of Figure 8.5. Similarly if we reverse the direction of the $l = 1$, $p = 0$ plate we get a beam equivalent to the $l = 1$, $p = 0$ case, as shown on the right hand side of Figure 8.5. In both cases the images created using multiple plates are not as clear as those created using a single plate of equivalent charge. This is due to the unwanted aberrations induced by each plate.

8.4   Discussion

Phase plates present an easy way to create and manipulate arbitrary vortex beams in the THz frequency range. By using a material with a low absorption coefficient in this frequency range such as Teflon ($\alpha = 0.2\,\text{cm}^{-1}$ at $550\,\text{GHz}$ [148]) we still achieve over 90% transmission, even for the thickest plates used in this work ($\approx 5\,\text{mm}$). If we were to use THz vortex beams for information transfer a method of quickly switching between values of l and p would be needed to achieve reasonable data transfer rates. Phase plates are however static optical elements and therefore the beams they create cannot be dynamically changed. Fast switching could be realised by using a spatial light modulator (SLM) or digital mirror device (DMD) to rapidly modify the helicity of the THz beam. The high-speed atom-based THz imaging

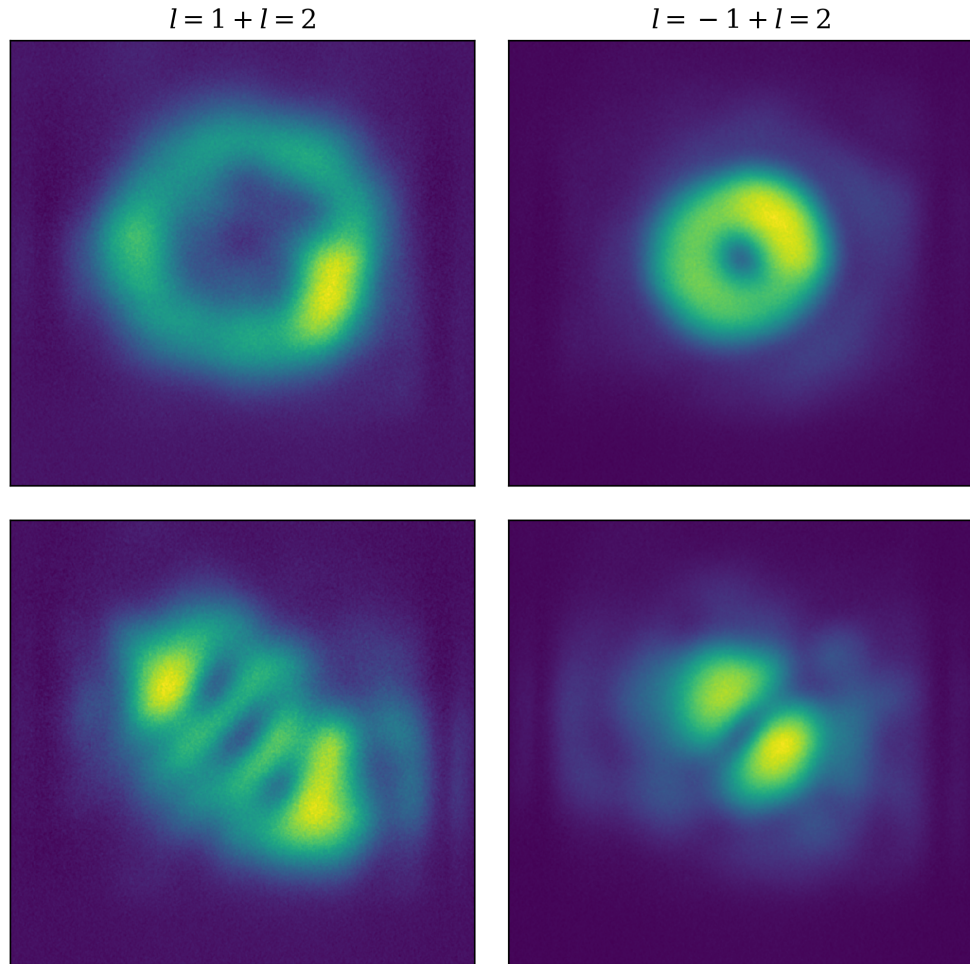Figure 8.5: **Combinations of phase plates.** Intensity (*top*) and auto-interference patterns (*bottom*) for LG beams produced by combining phase plates with $p = 0$, $l = 1$ and $p = 0$, $l = 2$. In the left hand column the plates were placed in the same direction, hence the resulting beam has $l = 3$. In the second column the $l = 1$ phase plate was reversed resulting in the final beam having $l = 1$.

system presented in Chapter 6 could then be used to image the intensity pattern and hence read out the encoded information at kHz rates.

Some of the images presented here include artefacts that are not due to the helicity of the beam induced by the phase plates. For example the fringes on the left and right hand edges of the images of the auto-interference patterns in Fig. 8.4 arise from reflections of the THz field inside the atomic vapour cell interfering with the incoming beam. This restriction imposed by the size of the vapour cell also explains the flattening of the edges of the rings in the intensity patterns in Fig. 8.4.

Throughout the work in this chapter we have assumed that the beam incident on the phase plate is a perfect Gaussian (LG_{00}) mode, however as has been stated in Chapter 3 the mode output by the THz horn has only 84% Gaussian mode content. As we do not know the mode content of the remaining 16% we cannot take these into consideration when designing the phase plates and performing numerical simulations. It is possible that these other modes in the initial beam contribute to the superposition of modes after the phase plates, further complicating the calculation of the scaling of the vortex radius. While it would theoretically be possible to create a pure Gaussian mode through spatial filtering of the THz beam, this would result in significant losses of power and reduce the signal to noise ratio (SNR) of the final images.

8.5 Conclusion

In this chapter we presented images of THz vortex beams created using Teflon phase plates. We created beams with both azimuthal l and radial phase index r and demonstrated using a tilted lens to create an auto-interference pattern, enabling us to read out both the sign and magnitude of l. We noted that the vortex radius did not scale with l as would be expected for pure LG modes and concluded that this was due to the phase plates creating a superposition of LG modes of different order. We also suggested ways in which the speed of our atom-based THz imaging system could be used in conjunction with THz vortex beams to perform THz free-space communications.

Chapter 9

Conclusion and Outlook

This thesis described the development and characterisation of a high-speed 2D THz imaging system using atomic vapour. The laser-excited atomic vapour acts as a THz-to-optical conversion medium, mapping an incident THz field onto green fluorescence that can be imaged with any optical camera. Demonstrations of some practical applications of this system were performed with a view to engaging in collaboration with industrial partners.

There are still unanswered questions pertaining to the interaction of the vapour with the THz radiation. For example as was discussed in Chapter 5 we have yet to establish the reason for the discrepancy between the measured and modelled fluorescence spectra. The model could be extended to include collisions causing transfer of population to states not coupled by electric dipole transitions but this would require significant modification. The impact of collisions with a buffer gas could be studied by repeating the measurements of the emitted fluorescence in vapour cells of differing background gas pressures.

There is much scope for improvement of the imaging system from many different angles, but the direction of these improvements would need to be application-focussed. For example, there is little point in investing time increasing the frame rate capabilities for an application that requires a higher spatial resolution. However there are some generic improvements that could be made in the near future. Throughout this thesis we used a very basic system of Teflon lenses to manipulate the THz field. By using a more sophisticated lens system comprising multiple

components we hope to reduce aberrations and improve the spatial resolution. Stabilisation of the final excitation laser to a stable reference cavity will reduce the noise on the fluorescence signal and improve the minimum detectable power of the system.

While the system presented here is far from a commercially viable product, we hope that the principle of using atoms to image THz fields provides the step forward that THz imaging requires to become widely used in many practical applications.

Bibliography

[1] C. S. Adams, J. D. Pritchard, and J. P. Shaffer, "Rydberg atom quantum technologies," *Journal of Physics B: Atomic, Molecular and Optical Physics*, vol. 53, p. 012002, Dec. 2019. [Cited on pages 1 and 2.]

[2] W. P. Schleich, K. S. Ranade, C. Anton, M. Arndt, M. Aspelmeyer, M. Bayer, G. Berg, T. Calarco, H. Fuchs, E. Giacobino, M. Grassl, P. Hänggi, W. M. Heckl, I.-V. Hertel, S. Huelga, F. Jelezko, B. Keimer, J. P. Kotthaus, G. Leuchs, N. Lütkenhaus, U. Maurer, T. Pfau, M. B. Plenio, E. M. Rasel, O. Renn, C. Silberhorn, J. Schiedmayer, D. Schmitt-Landsiedel, K. Schön-hammer, A. Ustinov, P. Walther, H. Weinfurter, E. Welzl, R. Wiesendanger, S. Wolf, A. Zeilinger, and P. Zoller, "Quantum technology: from research to application," *Applied Physics B*, vol. 122, p. 130, Apr 2016. [Cited on page 1.]

[3] D. Budker and M. Romalis, "Optical magnetometry," *Nature Physics*, vol. 3, pp. 227 EP –, Apr 2007. Review Article. [Cited on page 1.]

[4] A. Wickenbrock, F. Tricot, and F. Renzoni, "Magnetic induction measure-ments using an all-optical 87rb atomic magnetometer," *Applied Physics Let-ters*, vol. 103, no. 24, p. 243503, 2013. [Cited on page 1.]

[5] E. K. Dietsche, A. Larrouy, S. Haroche, J. M. Raimond, M. Brune, and S. Gleyzes, "High-sensitivity magnetometry with a single atom in a superposi-tion of two circular rydberg states," *Nature Physics*, 2019. [Cited on page 1.]

[6] Z.-K. Hu, B.-L. Sun, X.-C. Duan, M.-K. Zhou, L.-L. Chen, S. Zhan, Q.-Z. Zhang, and J. Luo, "Demonstration of an ultrahigh-sensitivity atom-

interferometry absolute gravimeter," *Phys. Rev. A*, vol. 88, p. 043610, Oct 2013. [Cited on page 1.]

[7] M. Kritsotakis, S. S. Szigeti, J. A. Dunningham, and S. A. Haine, "Optimal matter-wave gravimetry," *Phys. Rev. A*, vol. 98, p. 023629, Aug 2018. [Cited on page 1.]

[8] V. K. Shah and R. T. Wakai, "A compact, high performance atomic magnetometer for biomedical applications," *Physics in Medicine and Biology*, vol. 58, pp. 8153–8161, nov 2013. [Cited on page 1.]

[9] H. B. Dang, A. C. Maloof, and M. V. Romalis, "Ultrahigh sensitivity magnetic field and magnetization measurements with an atomic magnetometer," *Applied Physics Letters*, vol. 97, no. 15, p. 151110, 2010. [Cited on page 1.]

[10] R. J. Cooper, D. W. Prescott, P. Matz, K. L. Sauer, N. Dural, M. V. Romalis, E. L. Foley, T. W. Kornack, M. Monti, and J. Okamitsu, "Atomic magnetometer multisensor array for rf interference mitigation and unshielded detection of nuclear quadrupole resonance," *Phys. Rev. Applied*, vol. 6, p. 064014, Dec 2016. [Cited on page 1.]

[11] Rydberg Technologies. `https://www.rydbergtechnologies.com/`, 2020. Accessed: August 2020. [Cited on pages 2 and 38.]

[12] QuSpin. `https://www.quspin.com/`, 2020. Accessed: August 2020. [Cited on pages 2 and 38.]

[13] T. F. Gallagher, *Rydberg Atoms*. Cambridge Monographs on Atomic, Molecular and Chemical Physics, Cambridge University Press, 1994. [Cited on pages 2, 10, 12, 37, 60, 67, and 73.]

[14] N. Šibalić, J. Pritchard, C. Adams, and K. Weatherill, "Arc: An open-source library for calculating properties of alkali rydberg atoms," *Computer Physics Communications*, 2017. [Cited on pages 2, 7, 22, 37, 44, and 55.]

[15] J. A. Sedlacek, A. Schwettmann, H. Kübler, R. Löw, T. Pfau, and J. P. Shaffer, "Microwave electrometry with Rydberg atoms in a vapour cell using bright

atomic resonances," *Nature Physics*, vol. 8, pp. 819–824, Sept. 2012. [Cited on pages 2, 37, and 71.]

[16] H. Q. Fan, S. Kumar, R. Daschner, H. Kübler, and J. P. Shaffer, "Subwavelength microwave electric-field imaging using rydberg atoms inside atomic vapor cells," *Opt. Lett.*, vol. 39, pp. 3030–3033, May 2014. [Cited on pages 2, 37, and 71.]

[17] C. L. Holloway, J. A. Gordon, A. Schwarzkopf, D. A. Anderson, S. A. Miller, N. Thaicharoen, and G. Raithel, "Sub-wavelength imaging and field mapping via electromagnetically induced transparency and autler-townes splitting in rydberg atoms," *Applied Physics Letters*, vol. 104, no. 24, p. 244102, 2014. [Cited on pages 2, 37, and 71.]

[18] C. G. Wade, M. Marcuzzi, E. Levi, J. M. Kondo, I. Lesanovsky, C. S. Adams, and K. J. Weatherill, "A terahertz-driven non-equilibrium phase transition in a room temperature atomic vapour," *Nature Communications*, vol. 9, no. 1, p. 3567, 2018. [Cited on pages 2, 37, 53, and 71.]

[19] J. Schmidt, M. Fiedler, R. Albrecht, D. Djekic, P. Schalberger, H. Baur, R. Löw, N. Fruehauf, T. Pfau, J. Anders, E. R. Grant, and H. Kübler, "Proof of concept for an optogalvanic gas sensor for no based on rydberg excitations," *Applied Physics Letters*, vol. 113, no. 1, p. 011113, 2018. [Cited on page 2.]

[20] M. Kiffner, A. Feizpour, K. T. Kaczmarek, D. Jaksch, and J. Nunn, "Two-way interconversion of millimeter-wave and optical fields in rydberg gases," *New Journal of Physics*, vol. 18, p. 093030, sep 2016. [Cited on page 2.]

[21] T. Vogt, C. Gross, J. Han, S. B. Pal, M. Lam, M. Kiffner, and W. Li, "Efficient microwave-to-optical conversion using rydberg atoms," *Phys. Rev. A*, vol. 99, p. 023832, Feb 2019. [Cited on page 2.]

[22] J. P. Covey, A. Sipahigil, and M. Saffman, "Microwave-to-optical conversion via four-wave mixing in a cold ytterbium ensemble," *Phys. Rev. A*, vol. 100, p. 012307, Jul 2019. [Cited on page 2.]

[23] M. Drabbels and L. D. Noordam, "Infrared imaging camera based on a Rydberg atom photodetector," *Applied Physics Letters*, vol. 74, no. 13, p. 1797, 1999. [Cited on page 2.]

[24] A. Gürtler, A. S. Meijer, and W. J. van der Zande, "Imaging of terahertz radiation using a Rydberg atom photocathode," *Applied Physics Letters*, vol. 83, no. 2, p. 222, 2003. [Cited on pages 2 and 72.]

[25] S. S. Dhillon, M. S. Vitiello, E. H. Linfield, A. G. Davies, M. C. Hoffmann, J. Booske, C. Paoloni, M. Gensch, P. Weightman, G. P. Williams, E. Castro-Camus, D. R. S. Cumming, F. Simoens, I. Escorcia-Carranza, J. Grant, S. Lucyszyn, M. Kuwata-Gonokami, K. Konishi, M. Koch, C. A. Schmuttenmaer, T. L. Cocker, R. Huber, A. G. Markelz, Z. D. Taylor, V. P. Wallace, J. A. Zeitler, J. Sibik, T. M. Korter, B. Ellison, S. Rea, P. Goldsmith, K. B. Cooper, R. Appleby, D. Pardo, P. G. Huggard, V. Krozer, H. Shams, M. Fice, C. Renaud, A. Seeds, A. Stöhr, M. Naftaly, N. Ridler, R. Clarke, J. E. Cunningham, and M. B. Johnston, "The 2017 terahertz science and technology roadmap," *Journal of Physics D: Applied Physics*, vol. 50, no. 4, p. 043001, 2017. [Cited on pages 3, 5, and 71.]

[26] C. Jansen, S. Wietzke, O. Peters, M. Scheller, N. Vieweg, M. Salhi, N. Krumbholz, C. Jördens, T. Hochrein, and M. Koch, "Terahertz imaging: applications and perspectives," *Appl. Opt.*, vol. 49, pp. E48–E57, Jul 2010. [Cited on pages 3, 92, and 93.]

[27] P. Jepsen, D. Cooke, and M. Koch, "Terahertz spectroscopy and imaging: Modern techniques and applications," *Laser & Photonics Reviews*, vol. 5, no. 1, pp. 124–166, 2011. [Cited on pages 3 and 92.]

[28] J. F. Federici, B. Schulkin, F. Huang, D. Gary, R. Barat, F. Oliveira, and D. Zimdars, "Thz imaging and sensing for security applications-explosives, weapons and drugs," *Semiconductor Science and Technology*, vol. 20, no. 7, p. S266, 2005. [Cited on pages 3 and 71.]

[29] R. M. Woodward, V. P. Wallace, R. J. Pye, B. E. Cole, D. D. Arnone, E. H. Linfield, and M. Pepper, "Terahertz pulse imaging of ex vivo basal cell carcinoma," *Journal of Investigative Dermatology*, vol. 120, no. 1, pp. 72 – 78, 2003. [Cited on pages 3 and 71.]

[30] D. M. Mittleman, "Twenty years of terahertz imaging, invited," *Opt. Express*, vol. 26, pp. 9417–9431, Apr 2018. [Cited on pages 3, 5, 71, and 92.]

[31] B. S. Peter, S. Yngvesson, P. Siqueira, P. Kelly, A. Khan, S. Glick, and A. Karellas, "Development and testing of a single frequency terahertz imaging system for breast cancer detection," *IEEE Transactions on Terahertz Science and Technology*, vol. 3, pp. 374–386, July 2013. [Cited on pages 3 and 71.]

[32] S. Wietzke, C. Jördens, N. Krumbholz, B. Baudrit, M. Bastian, and M. Koch, "Terahertz imaging: a new non-destructive technique for the quality control of plastic weld joints," *Journal of the European Optical Society - Rapid publications*, vol. 2, no. 0, 2007. [Cited on pages 3 and 71.]

[33] S.-L. Chen, Y.-C. Chang, C. Zhang, J. G. Ok, T. Ling, M. T. Mihnev, T. B. Norris, and L. J. Guo, "Efficient real-time detection of terahertz pulse radiation based on photoacoustic conversion by carbon nanotube nanocomposite," *Nature Photonics*, vol. 8, p. 537, May 2014. [Cited on pages 4 and 5.]

[34] H. Guerboukha, K. Nallappan, and M. Skorobogatiy, "Toward real-time terahertz imaging," *Adv. Opt. Photon.*, vol. 10, pp. 843–938, Dec 2018. [Cited on page 4.]

[35] M. J. E. Golay, "The theoretical and practical sensitivity of the pneumatic infra-red detector," *Review of Scientific Instruments*, vol. 20, no. 11, pp. 816–820, 1949. [Cited on page 4.]

[36] Y.-S. Lee, *Principles of Terahertz Science and Technology*. Springer, 2009. [Cited on page 4.]

[37] P. Dean, M. U. Shaukat, S. P. Khanna, S. Chakraborty, M. Lachab, A. Burnett, G. Davies, and E. H. Linfield, "Absorption-sensitive diffuse reflection

imaging of concealed powders using a terahertz quantum cascade laser," *Opt. Express*, vol. 16, pp. 5997–6007, Apr 2008. [Cited on page 4.]

[38] N. Rothbart, H. Richter, M. Wienold, L. Schrottke, H. T. Grahn, and H.-W. Hubers, "Fast 2-d and 3-d terahertz imaging with a quantum-cascade laser and a scanning mirror," *IEEE Transactions on Terahertz Science and Technology*, vol. 3, pp. 617–624, 2013. [Cited on page 4.]

[39] C. M. Watts, D. Shrekenhamer, J. Montoya, G. Lipworth, J. Hunt, T. Sleasman, S. Krishna, D. R. Smith, and W. J. Padilla, "Terahertz compressive imaging with metamaterial spatial light modulators," *Nature Photonics*, vol. 8, pp. 605 EP –, Jun 2014. [Cited on page 4.]

[40] R. I. Stantchev, B. Sun, S. M. Hornett, P. A. Hobson, G. M. Gibson, M. J. Padgett, and E. Hendry, "Noninvasive, near-field terahertz imaging of hidden objects using a single-pixel detector," *Science Advances*, vol. 2, no. 6, 2016. [Cited on page 4.]

[41] R. I. Stantchev, X. Yu, T. Blu, and E. Pickwell-MacPherson, "Real-time terahertz imaging with a single-pixel detector," *Nature communications*, vol. 11, no. 1, pp. 1–8, 2020. [Cited on page 4.]

[42] A. W. Lee and Q. Hu, "Real-time, continuous-wave terahertz imaging by use of a microbolometer focal-plane array," *Opt. Lett.*, vol. 30, pp. 2563–2565, Oct 2005. [Cited on page 4.]

[43] A. W. M. Lee, B. S. Williams, S. Kumar, Q. Hu, and J. L. Reno, "Real-time imaging using a 4.3-thz quantum cascade laser and a 320×240 microbolometer focal-plane array," *IEEE Photonics Technology Letters*, vol. 18, pp. 1415–1417, July 2006. [Cited on page 4.]

[44] H. Qin, J. Sun, S. Liang, X. Li, X. Yang, Z. He, C. Yu, and Z. Feng, "Room-temperature, low-impedance and high-sensitivity terahertz direct detector based on bilayer graphene field-effect transistor," *Carbon*, vol. 116, pp. 760 – 765, 2017. [Cited on page 4.]

[45] D. Suzuki, S. Oda, and Y. Kawano, "A flexible and wearable terahertz scanner," *Nature Photonics*, vol. 10, pp. 809 EP –, Nov 2016. Article. [Cited on page 4.]

[46] M. A. Dem'yanenko, D. G. Esaev, B. A. Knyazev, G. N. Kulipanov, and N. A. Vinokurov, "Imaging with a 90 frames per s microbolometer focal plane array and high-power terahertz free electron laser," *Applied Physics Letters*, vol. 92, no. 13, p. 131116, 2008. [Cited on page 4.]

[47] F. Simoens and J. Meilhan, "Terahertz real-time imaging uncooled array based on antenna- and cavity-coupled bolometers," *Philosophical Transactions of the Royal Society of London A: Mathematical, Physical and Engineering Sciences*, vol. 372, no. 2012, 2014. [Cited on page 4.]

[48] S. Ariyoshi, C. Otani, A. Dobroiu, H. Matsuo, H. Sato, T. Taino, K. Kawase, and H. Shimizu, "Superconducting detector array for terahertz imaging applications," *Japanese Journal of Applied Physics*, vol. 45, 10 2006. [Cited on page 4.]

[49] M. Clerici, D. Faccio, L. Caspani, M. Peccianti, E. Rubino, L. Razzari, F. Légaré, T. Ozaki, and R. Morandotti, "Ccd-based imaging and 3d space–time mapping of terahertz fields via kerr frequency conversion," *Opt. Lett.*, vol. 38, pp. 1899–1901, Jun 2013. [Cited on page 5.]

[50] S. Fan, F. Qi, T. Notake, K. Nawata, Y. Takida, T. Matsukawa, and H. Minamide, "Diffraction-limited real-time terahertz imaging by optical frequency up-conversion in a dast crystal," *Opt. Express*, vol. 23, pp. 7611–7618, Mar 2015. [Cited on pages 5 and 77.]

[51] C. G. Wade, N. Šibalić, N. R. de Melo, J. M. Kondo, K. J. Weatherill, and C. Adams, "Real-time, near-field terahertz imaging with atomic optical fluorescence," *Nature Photonics*, vol. 72, pp. 40–43, 2017. [Cited on pages 5, 53, 72, and 89.]

[52] L. A. Downes, A. R. MacKellar, C. S. Adams, and K. J. Weatherill, "High-speed thz imaging for production line monitoring," in *2019 44th International*

Conference on Infrared, Millimeter, and Terahertz Waves (IRMMW-THz), pp. 1–2, 2019. [Cited on page 6.]

[53] L. A. Downes, A. R. MacKellar, D. J. Whiting, C. Bourgenot, C. S. Adams, and K. J. Weatherill, "Full-field terahertz imaging at kilohertz frame rates using atomic vapor," *Phys. Rev. X*, vol. 10, p. 011027, Feb 2020. [Cited on pages 6, 72, and 77.]

[54] C. Foot, *Atomic Physics*. Oxford Master Series in Physics, Oxford University Press, 2005. [Cited on pages 8, 9, 10, 11, 13, 15, and 21.]

[55] I. Georgescu, "Rubidium round-the-clock," *Nature Chemistry*, vol. 7, pp. 1034–1034, Dec 2015. [Cited on page 10.]

[56] S. H. Autler and C. H. Townes, "Stark effect in rapidly varying fields," *Phys. Rev.*, vol. 100, pp. 703–722, Oct 1955. [Cited on page 16.]

[57] P. M. Anisimov, J. P. Dowling, and B. C. Sanders, "Objectively discerning autler-townes splitting from electromagnetically induced transparency," *Phys. Rev. Lett.*, vol. 107, p. 163604, Oct 2011. [Cited on page 17.]

[58] M. Fox, *Quantum Optics: An Introduction*. Oxford Master Series in Physics, Oxford University Press, 2006. [Cited on pages 17, 37, and 62.]

[59] C. Cohen-Tannoudji, G. Grynberg, and J. Dupont-Roc, *Atom-Photon Interactions: Basic Processes and Applications*. New York: Wiley, 1992. [Cited on page 18.]

[60] J. Gea-Banacloche, Y.-q. Li, S.-z. Jin, and M. Xiao, "Electromagnetically induced transparency in ladder-type inhomogeneously broadened media: Theory and experiment," *Phys. Rev. A*, vol. 51, pp. 576–584, Jan 1995. [Cited on pages 18 and 20.]

[61] K. F. Riley, M. P. Hobson, and S. J. Bence, *Mathematical Methods for Physics and Engineering - 3rd Edition*. Cambridge University Press, 3 ed., 02 2006. [Cited on page 19.]

[62] D. A. Steck, "Cesium d line data." `http://steck.us/alkalidata`, November 2019. [Cited on pages 21, 23, and 140.]

[63] C. Carr, M. Tanasittikosol, A. Sargsyan, D. Sarkisyan, C. S. Adams, and K. J. Weatherill, "Three-photon electromagnetically induced transparency using Rydberg states," *Optics Letters*, vol. 37, no. 18, pp. 3858–3860, 2012. [Cited on page 23.]

[64] M. L. Harris, C. S. Adams, S. L. Cornish, I. C. McLeod, E. Tarleton, and I. G. Hughes, "Polarization spectroscopy in rubidium and cesium," *Phys. Rev. A*, vol. 73, p. 062509, Jun 2006. [Cited on pages 24 and 140.]

[65] C. Carr, C. S. Adams, and K. J. Weatherill, "Polarization spectroscopy of an excited state transition," *Opt. Lett.*, vol. 37, pp. 118–120, Jan 2012. [Cited on pages 24 and 140.]

[66] C. Adams and I. Hughes, *Optics F2f: From Fourier to Fresnel.* Oxford University Press, 2019. [Cited on pages 25, 74, 76, 94, and 96.]

[67] P. Lockhart, T. Ramotowski, and M. Rice, "Terahertz frequency optical properties of acoustic materials," *Polymer Testing*, vol. 34, pp. 140 − 145, 2014. [Cited on pages 26 and 107.]

[68] Virginia Diodes Inc., "Feedhorn summary." `https://www.vadiodes.com/images/AppNotes/VDI_Feedhorn_Summary_2020.05.04.pdf`, 2020. Accessed: August 2020. [Cited on pages 26 and 83.]

[69] A. Loot, "Pyandor." `https://github.com/ardiloot/PyAndor`, Jan. 2018. [Cited on page 30.]

[70] A. Poehlmann. `https://github.com/ap--/python-seabreeze`, May 2020. [Cited on page 30.]

[71] T. Bronger, G. Thalhammer, and M. Dartiailh. `https://github.com/pyvisa/pyvisa`, Aug. 2020. [Cited on page 30.]

[72] National Instruments. `https://github.com/ni/nidaqmx-python/`, Dec. 2017. [Cited on page 30.]

[73] A. Edelstein, M. Tsuchida, N. Amodaj, H. Pinkard, R. Vale, and N. Stuurman, "Advanced methods of microscope control using micro-manager software," *Journal of Biological Methods*, vol. 1, no. 2, 2014. [Cited on page 30.]

[74] A. Osterwalder and F. Merkt, "Using high rydberg states as electric field sensors," *Phys. Rev. Lett.*, vol. 82, pp. 1831–1834, Mar 1999. [Cited on page 37.]

[75] M. G. Bason, M. Tanasittikosol, A. Sargsyan, A. K. Mohapatra, D. Sarkisyan, R. M. Potvliege, and C. S. Adams, "Enhanced electric field sensitivity of rf-dressed rydberg dark states," *New Journal of Physics*, vol. 12, p. 065015, jun 2010. [Cited on page 37.]

[76] R. P. Abel, C. Carr, U. Krohn, and C. S. Adams, "Electrometry near a dielectric surface using rydberg electromagnetically induced transparency," *Phys. Rev. A*, vol. 84, p. 023408, Aug 2011. [Cited on page 37.]

[77] S. Kumar, H. Fan, H. Kübler, A. J. Jahangiri, and J. P. Shaffer, "Rydberg-atom based radio-frequency electrometry using frequency modulation spectroscopy in room temperature vapor cells," *Opt. Express*, vol. 25, pp. 8625–8637, Apr 2017. [Cited on page 37.]

[78] D. H. Meyer, K. C. Cox, F. K. Fatemi, and P. D. Kunz, "Digital communication with rydberg atoms and amplitude-modulated microwave fields," *Applied Physics Letters*, vol. 112, no. 21, p. 211108, 2018. [Cited on page 38.]

[79] Z. Song, H. Liu, X. Liu, W. Zhang, H. Zou, J. Zhang, and J. Qu, "Rydberg-atom-based digital communication using a continuously tunable radio-frequency carrier," *Opt. Express*, vol. 27, pp. 8848–8857, Mar 2019. [Cited on page 38.]

[80] C. L. Holloway, M. T. Simons, A. H. Haddab, C. J. Williams, and M. W. Holloway, "A "real-time" guitar recording using rydberg atoms and electromagnet-

ically induced transparency: Quantum physics meets music," *AIP Advances*, vol. 9, no. 6, p. 065110, 2019. [Cited on page 38.]

[81] M. T. Simons, J. A. Gordon, and C. L. Holloway, "Fiber-coupled vapor cell for a portable rydberg atom-based radio frequency electric field sensor," *Appl. Opt.*, vol. 57, pp. 6456–6460, Aug 2018. [Cited on page 38.]

[82] Virginia Diodes Inc., *VDI User Guide - AMC 331*, section 3 ed., Aug. 2012. [Cited on pages 38, 42, and 43.]

[83] M. T. Simons, J. A. Gordon, and C. L. Holloway, "Simultaneous use of cs and rb rydberg atoms for dipole moment assessment and rf electric field measurements via electromagnetically induced transparency," *Journal of Applied Physics*, vol. 120, no. 12, p. 123103, 2016. [Cited on page 40.]

[84] C. L. Holloway, J. A. Gordon, S. Jefferts, A. Schwarzkopf, D. A. Anderson, S. A. Miller, N. Thaicharoen, and G. Raithel, "Broadband rydberg atom-based electric-field probe for si-traceable, self-calibrated measurements," *IEEE Transactions on Antennas and Propagation*, vol. 62, no. 12, pp. 6169–6182, 2014. [Cited on page 40.]

[85] K.-H. Weber and C. J. Sansonetti, "Accurate energies of ns, np, nd, nf, and ng levels of neutral cesium," *Phys. Rev. A*, vol. 35, pp. 4650–4660, Jun 1987. [Cited on pages 47, 48, 49, 51, 147, and 148.]

[86] P. Goy, J. M. Raimond, G. Vitrant, and S. Haroche, "Millimeter-wave spectroscopy in cesium rydberg states. quantum defects, fine- and hyperfine-structure measurements," *Phys. Rev. A*, vol. 26, pp. 2733–2742, Nov 1982. [Cited on pages 47, 48, 49, 51, 144, and 147.]

[87] C. J. Sansonetti and C. J. Lorenzen, "Doppler-free resonantly enhanced two-photon spectroscopy of np and nf rydberg states in atomic cesium," *Phys. Rev. A*, vol. 30, pp. 1805–1811, Oct 1984. [Cited on pages 47, 48, 147, and 148.]

[88] C.-J. Lorenzen and K. Niemax, "Precise quantum defects of ns, np and nd levels in cs i," *Zeitschrift für Physik A Atoms and Nuclei*, vol. 315, no. 2, pp. 127–133, 1984. [Cited on pages 47, 49, and 51.]

[89] W. Li, I. Mourachko, M. W. Noel, and T. F. Gallagher, "Millimeter-wave spectroscopy of cold rb rydberg atoms in a magneto-optical trap: Quantum defects of the ns, np, and nd series," *Phys. Rev. A*, vol. 67, p. 052502, May 2003. [Cited on pages 47 and 144.]

[90] D. Weller, A. Urvoy, A. Rico, R. Löw, and H. Kübler, "Charge-induced optical bistability in thermal rydberg vapor," *Phys. Rev. A*, vol. 94, p. 063820, Dec 2016. [Cited on page 53.]

[91] D. Weller, J. P. Shaffer, T. Pfau, R. Löw, and H. Kübler, "Interplay between thermal rydberg gases and plasmas," *Phys. Rev. A*, vol. 99, p. 043418, Apr 2019. [Cited on page 53.]

[92] C. Carr, R. Ritter, C. G. Wade, C. S. Adams, and K. J. Weatherill, "Nonequilibrium phase transition in a dilute rydberg ensemble," *Phys. Rev. Lett.*, vol. 111, p. 113901, Sep 2013. [Cited on pages 53, 67, and 70.]

[93] D.-S. Ding, H. Busche, B.-S. Shi, G.-C. Guo, and C. S. Adams, "Phase diagram and self-organizing dynamics in a thermal ensemble of strongly interacting rydberg atoms," *Phys. Rev. X*, vol. 10, p. 021023, Apr 2020. [Cited on page 53.]

[94] D. Petrosyan and K. Mølmer, "Deterministic free-space source of single photons using rydberg atoms," *Phys. Rev. Lett.*, vol. 121, p. 123605, Sep 2018. [Cited on page 53.]

[95] F. Ripka, H. Kübler, R. Löw, and T. Pfau, "A room-temperature single-photon source based on strongly interacting rydberg atoms," *Science*, vol. 362, no. 6413, pp. 446–449, 2018. [Cited on page 53.]

[96] A. C. Tam, T. Yabuzaki, S. M. Curry, M. Hou, and W. Happer, "Inelastic cross sections in $\mathrm{Cs}(n^2 d_J) + \mathrm{Cs}(6^2 s_{\frac{1}{2}})$ collisions," *Phys. Rev. A*, vol. 17, pp. 1862–1868, Jun 1978. [Cited on pages 60 and 67.]

[97] C. Gabbanini, A. Lucchesini, and S. Gozzini, "Self-quenching mechanism in caesium rydberg states," *Journal of Physics B: Atomic, Molecular and Optical Physics*, vol. 25, pp. 3145–3154, jul 1992. [Cited on pages 60 and 67.]

[98] B. B. Hu and M. C. Nuss, "Imaging with terahertz waves," *Opt. Lett.*, vol. 20, pp. 1716–1718, Aug 1995. [Cited on pages 71 and 101.]

[99] S. Zhong, "Progress in terahertz nondestructive testing: A review," *Frontiers of Mechanical Engineering*, pp. 1–9, 2019. [Cited on pages 71, 93, and 101.]

[100] I. G. Hughes and T. P. A. Hase, *Measurements and their Uncertainties*. Oxford University Press, 2010. [Cited on page 80.]

[101] R. V. Jones, J. C. S. Richards, and T. R. Merton, "The polarization of light by narrow slits," *Proceedings of the Royal Society of London. Series A. Mathematical and Physical Sciences*, vol. 225, no. 1160, pp. 122–135, 1954. [Cited on page 84.]

[102] P. F. Chimento, N. V. Kuzmin, J. Bosman, P. F. A. Alkemade, G. W. 't Hooft, and E. R. Eliel, "A subwavelength slit as a quarter-wave retarder," *Opt. Express*, vol. 19, pp. 24219–24227, Nov 2011. [Cited on page 84.]

[103] A. Michelson, *Studies in Optics*. University of Chicago science series, University of Chicago Press, 1927. [Cited on page 86.]

[104] F. Rutz, M. Koch, S. Khare, M. Moneke, H. Richter, and U. Ewert, "Terahertz quality control of polymetric products," *International Journal of Infrared and Millimeter Waves*, vol. 27, pp. 547–556, Apr 2006. [Cited on page 93.]

[105] D. Nüßler and J. Jonuscheit, "Terahertz based non-destructive testing (ndt)," *tm - Technisches Messen*, no. 0, 2020. [Cited on page 93.]

[106] K.-H. Im, S.-K. Kim, J.-A. Jung, Y.-T. Cho, Y.-D. Wood, and C.-P. Chiou, "Nde characterization and inspection techniques of trailing edges in wind turbine blades using terahertz waves," *Journal of Mechanical Science and Technology*, vol. 33, pp. 4745–4753, Oct 2019. [Cited on page 93.]

[107] K. Ahi, S. Shahbazmohamadi, and N. Asadizanjani, "Quality control and authentication of packaged integrated circuits using enhanced-spatial-resolution terahertz time-domain spectroscopy and imaging," *Optics and Lasers in Engineering*, vol. 104, pp. 274 – 284, 2018. Optical Tools for Metrology, Imaging and Diagnostics. [Cited on pages 93 and 101.]

[108] A. Gowen, C. O'Sullivan, and C. O'Donnell, "Terahertz time domain spectroscopy and imaging: Emerging techniques for food process monitoring and quality control," *Trends in Food Science & Technology*, vol. 25, no. 1, pp. 40 – 46, 2012. [Cited on pages 93 and 97.]

[109] L. Afsah-Hejri, P. Hajeb, P. Ara, and R. J. Ehsani, "A comprehensive review on food applications of terahertz spectroscopy and imaging," *Comprehensive Reviews in Food Science and Food Safety*, vol. 18, no. 5, pp. 1563–1621, 2019. [Cited on pages 93 and 97.]

[110] M. Amanti, M. Fischer, G. Scalari, M. Beck, and J. Faist, "Low-divergence single-mode terahertz quantum cascade laser," *Nature Photonics*, vol. 3, no. 10, pp. 586–590, 2009. [Cited on page 94.]

[111] H. Richter, N. Rothbart, and H.-W. Hübers, "Characterizing the beam properties of terahertz quantum-cascade lasers," *Journal of Infrared, Millimeter, and Terahertz Waves*, vol. 35, no. 8, pp. 686–698, 2014. [Cited on page 94.]

[112] C. Sirtori, S. Barbieri, and R. Colombelli, "Wave engineering with thz quantum cascade lasers," *Nature Photonics*, vol. 7, no. 9, pp. 691–701, 2013. [Cited on page 94.]

[113] A. Adam, I. Kašalynas, J. Hovenier, T. Klaassen, J. Gao, E. Orlova, B. Williams, S. Kumar, Q. Hu, and J. Reno, "Beam patterns of terahertz quantum cascade lasers with subwavelength cavity dimensions," *Applied Physics Letters*, vol. 88, no. 15, p. 151105, 2006. [Cited on page 94.]

[114] S. Busch, M. Weidenbach, M. Fey, F. Schäfer, T. Probst, and M. Koch, "Optical properties of 3d printable plastics in the thz regime and their application for

3d printed thz optics," *Journal of Infrared, Millimeter, and Terahertz Waves*, vol. 35, no. 12, pp. 993–997, 2014. [Cited on page 94.]

[115] W. D. Furlan, V. Ferrando, J. A. Monsoriu, P. Zagrajek, E. Czerwińska, and M. Szustakowski, "3d printed diffractive terahertz lenses," *Optics letters*, vol. 41, no. 8, pp. 1748–1751, 2016. [Cited on page 94.]

[116] M. Auty, "State of the art imaging technology for food processing." Invited talk: 10th Intelligent Imaging, Apr. 2019. [Cited on page 97.]

[117] G.-J. Kim, J.-I. Kim, S.-G. Jeon, J. Kim, K.-K. Park, and C.-H. Oh, "Enhanced continuous-wave terahertz imaging with a horn antenna for food inspection," *Journal of Infrared, Millimeter, and Terahertz Waves*, vol. 33, pp. 657–664, Jun 2012. [Cited on page 97.]

[118] G. Ok, K. Park, H. J. Kim, H. S. Chun, and S.-W. Choi, "High-speed terahertz imaging toward food quality inspection," *Appl. Opt.*, vol. 53, pp. 1406–1412, Mar 2014. [Cited on page 97.]

[119] G. Ok, H. J. Shin, M.-C. Lim, and S.-W. Choi, "Large-scan-area sub-terahertz imaging system for nondestructive food quality inspection," *Food Control*, vol. 96, pp. 383 – 389, 2019. [Cited on page 97.]

[120] TeraSense, "Thz imaging scanner." `https://terasense.com/products/thz-scanner/`. [Accessed August 2020]. [Cited on page 97.]

[121] M. T. Mohd Khairi, S. Ibrahim, M. A. Md Yunus, and M. Faramarzi, "Noninvasive techniques for detection of foreign bodies in food: A review," *Journal of food process engineering*, vol. 41, no. 6, p. e12808, 2018. [Cited on pages 97 and 98.]

[122] B. Quinn, S. Butler, and R. Smithers, "Mars recalls chocolate bars in 55 countries after plastic found in product." `https://www.theguardian.com/lifeandstyle/2016/feb/23/mars-chocolate-product-recalls-snickers-milky-way-celebrations-germany-netherlands`, Feb 2016. [Accessed: August 2020]. [Cited on page 97.]

[123] Food Standards Agency. `https://www.food.gov.uk/news-alerts/search/alerts`, August 2020. [Accessed: August 2020]. [Cited on page 97.]

[124] EUFIC, "X-ray in food inspection." `https://www.eufic.org/en/food-production/article/the-use-of-x-rays-in-food-inspection`, Jan 2013. [Accessed: August 2020]. [Cited on page 97.]

[125] M. Graves, A. Smith, and B. Batchelor, "Approaches to foreign body detection in foods," *Trends in Food Science & Technology*, vol. 9, no. 1, pp. 21 – 27, 1998. [Cited on page 98.]

[126] C. Jördens and M. Koch, "Detection of foreign bodies in chocolate with pulsed terahertz spectroscopy," *Optical Engineering*, vol. 47, no. 3, pp. 1 – 5, 2008. [Cited on page 98.]

[127] J. A. S. Williams and W. Bonawi-Tan, "Online quality control with raman spectroscopy in pharmaceutical tablet manufacturing," *Journal of Manufacturing Systems*, vol. 23, no. 4, pp. 299 – 308, 2004. [Cited on page 99.]

[128] G. Gibson, J. Courtial, M. J. Padgett, M. Vasnetsov, V. Pas'ko, S. M. Barnett, and S. Franke-Arnold, "Free-space information transfer using light beams carrying orbital angular momentum," *Opt. Express*, vol. 12, pp. 5448–5456, Nov 2004. [Cited on page 105.]

[129] M. Krenn, R. Fickler, M. Fink, J. Handsteiner, M. Malik, T. Scheidl, R. Ursin, and A. Zeilinger, "Communication with spatially modulated light through turbulent air across vienna," *New Journal of Physics*, vol. 16, p. 113028, Nov 2014. [Cited on page 106.]

[130] G. Turnbull, D. Robertson, G. Smith, L. Allen, and M. Padgett, "The generation of free-space laguerre-gaussian modes at millimetre-wave frequencies by use of a spiral phaseplate," *Optics Communications*, vol. 127, no. 4, pp. 183 – 188, 1996. [Cited on page 106.]

[131] K. Miyamoto, K. Suizu, T. Akiba, and T. Omatsu, "Direct observation of the topological charge of a terahertz vortex beam generated by a tsurupica spiral

phase plate," *Applied Physics Letters*, vol. 104, no. 26, p. 261104, 2014. [Cited on page 106.]

[132] X. Wei, C. Liu, L. Niu, Z. Zhang, K. Wang, Z. Yang, and J. Liu, "Generation of arbitrary order bessel beams via 3d printed axicons at the terahertz frequency range," *Appl. Opt.*, vol. 54, pp. 10641–10649, Dec 2015. [Cited on page 106.]

[133] J. He, X. Wang, D. Hu, J. Ye, S. Feng, Q. Kan, and Y. Zhang, "Generation and evolution of the terahertz vortex beam," *Opt. Express*, vol. 21, pp. 20230–20239, Aug 2013. [Cited on page 106.]

[134] R. Imai, N. Kanda, T. Higuchi, K. Konishi, and M. Kuwata-Gonokami, "Generation of broadband terahertz vortex beams," *Opt. Lett.*, vol. 39, pp. 3714–3717, Jul 2014. [Cited on page 106.]

[135] Z. Xie, X. Wang, J. Ye, S. Feng, W. Sun, T. Akalin, and Y. Zhang, "Spatial terahertz modulator," *Scientific Reports*, vol. 3, no. 1, p. 3347, 2013. [Cited on page 106.]

[136] G. Ruffato, M. Massari, and F. Romanato, "Generation of high-order laguerre-gaussian modes by means of spiral phase plates," *Opt. Lett.*, vol. 39, pp. 5094–5097, Sep 2014. [Cited on page 106.]

[137] L. Allen, M. W. Beijersbergen, R. J. C. Spreeuw, and J. P. Woerdman, "Orbital angular momentum of light and the transformation of laguerre-gaussian laser modes," *Phys. Rev. A*, vol. 45, pp. 8185–8189, Jun 1992. [Cited on page 106.]

[138] Z. Guo, Z. Wang, M. I. Dedo, and K. Guo, "The orbital angular momentum encoding system with radial indices of laguerre–gaussian beam," *IEEE Photonics Journal*, vol. 10, pp. 1–11, Oct 2018. [Cited on page 107.]

[139] A. Faßbender, J. Babocký, P. Dvořák, V. Křápek, and S. Linden, "Invited article: Direct phase mapping of broadband laguerre-gaussian metasurfaces," *APL Photonics*, vol. 3, no. 11, p. 110803, 2018. [Cited on page 107.]

[140] A. Chopinaud, M. Jacquey, B. Viaris de Lesegno, and L. Pruvost, "High helicity vortex conversion in a rubidium vapor," *Phys. Rev. A*, vol. 97, p. 063806, Jun 2018. [Cited on page 109.]

[141] P. Vaity, J. Banerji, and R. Singh, "Measuring the topological charge of an optical vortex by using a tilted convex lens," *Physics Letters A*, vol. 377, no. 15, pp. 1154 – 1156, 2013. [Cited on page 109.]

[142] M. J. Padgett, F. M. Miatto, M. P. J. Lavery, A. Zeilinger, and R. W. Boyd, "Divergence of an orbital-angular-momentum-carrying beam upon propagation," *New Journal of Physics*, vol. 17, p. 023011, feb 2015. [Cited on page 113.]

[143] V. V. Kotlyar, S. N. Khonina, A. A. Kovalev, V. A. Soifer, H. Elfstrom, and J. Turunen, "Diffraction of a plane, finite-radius wave by a spiral phase plate," *Opt. Lett.*, vol. 31, pp. 1597–1599, Jun 2006. [Cited on page 113.]

[144] K. Saitoh, Y. Hasegawa, N. Tanaka, and M. Uchida, "Production of electron vortex beams carrying large orbital angular momentum using spiral zone plates," *Journal of Electron Microscopy*, vol. 61, pp. 171–177, 03 2012. [Cited on page 113.]

[145] W. Harm, S. Bernet, M. Ritsch-Marte, I. Harder, and N. Lindlein, "Adjustable diffractive spiral phase plates," *Opt. Express*, vol. 23, pp. 413–421, Jan 2015. [Cited on page 113.]

[146] M. Beijersbergen, R. Coerwinkel, M. Kristensen, and J. Woerdman, "Helical-wavefront laser beams produced with a spiral phaseplate," *Optics Communications*, vol. 112, no. 5, pp. 321 – 327, 1994. [Cited on page 113.]

[147] S. Sundbeck, I. Gruzberg, and D. G. Grier, "Structure and scaling of helical modes of light," *Opt. Lett.*, vol. 30, pp. 477–479, Mar 2005. [Cited on page 113.]

[148] C. Winnewisser, F. Lewen, and H. Helm, "Transmission characteristics of dichroic filters measured by thz time-domain spectroscopy," *Applied Physics A*, vol. 66, pp. 593–598, Jun 1998. [Cited on page 114.]

[149] C. P. Pearman, C. S. Adams, S. G. Cox, P. F. Griffin, D. A. Smith, and I. G. Hughes, "Polarization spectroscopy of a closed atomic transition: applications to laser frequency locking," *Journal of Physics B: Atomic, Molecular and Optical Physics*, vol. 35, pp. 5141–5151, dec 2002. [Cited on page 140.]

[150] L. R. Pendrill, "Variation of fine structure along atomic rydberg series," *Physica Scripta*, vol. 27, pp. 371–373, may 1983. [Cited on page 147.]

Appendices

Appendix A

Laser Stabilisation Techniques

As outlined in Chapter 3, we use a three-step excitation scheme to excite atoms to Rydberg level. The first two lasers in the ladder scheme (852 nm and 1470 nm) are locked to an atomic reference using polarisation spectroscopy. This reference is provided by a Cs bulk vapour cell which does not require additional heating. Both lasers are locked to the zero crossing of an error signal using a PID control circuit.

A.1 Ground State Polarisation Spectroscopy

The 852 nm probe laser is stabilised to the $6S_{1/2}$, F $= 4 \rightarrow 6P_{3/2}$, F$' = 5$ hyperfine transition using polarisation spectroscopy.This is a sub-Doppler pump-probe technique allowing the laser to be locked to a specific hyperfine transition and hence achieve stabilisation to within a few MHz.

In this technique a circularly polarised pump beam is aligned such that it is almost counterpropagating with a linearly polarized weak probe beam. The pump beam drives σ^+ transitions between the ground and exited states, leading to optical pumping of the population into the $m_F = F$ level of the ground state. The linearly polarised probe beam can be thought of as having two components, each having equal amplitude but opposite circular polarisation. Each component will interact differently with the pumped atomic vapour, with one driving σ^+ and the other σ^- transitions. These transitions will have different transition strengths, as defined by the Clebsch-Gordan coefficients, and hence the two components of the probe beam

will experience a different amount of absorption. This will result in a rotation of the polarisation of the probe beam which can then be detected by measuring absorption using two photodiodes at the outputs of a PBS cube. In the absence of the pump beam the vapour is isotropic and the probe beam polarisation is not altered. This results in an equal signal at both photodiodes and hence the difference is zero. When the medium is pumped and becomes anisotropic, the rotation of polarisation of the probe beam results in different intensities at each photodiode and hence a non-zero difference signal. It is this difference between the photodiode signals that will provide the error signal for laser locking [64, 149].

In the experiments described in this thesis, the circularly polarised pump beam optically pumps population into the $F = 4$, $m_F = 4$ hyperfine level of the Cs ground state $(6S_{1/2})$. The probe beam can then drive transitions to the $F' = 3, 4, 5$ hyperfine levels of the excited state $(6P_{3/2})$. The hyperfine transition that provides the strongest signal in the polarisation spectrum is the $F = 4 \rightarrow F' = 5$ transition. This is due to the 'closed' $F = 4, m_F = 4 \rightarrow F' = 5, m'_F = 5$ transition displaying the greatest anisotropy.

Figure A.1 shows the error signal (top) and the saturated absorption signal (bottom) for transitions from the $6S_{1/2}$, F = 4 hyperfine state in Cs. The positions of features due to the hyperfine transitions F = 4 $\rightarrow$ F' = 3, 4, 5 are indicated by the blue dashed lines. The grey dotted lines indicate the positions of the crossover resonances and are found halfway between pairs of hyperfine transitions. The closed transition F = 4 $\rightarrow$ F' = 5, set to be at zero detuning, has the sharpest dispersive signal in the polarisation spectrum and is used as the laser lock error signal. The outer peaks, caused by the $F = 4 \rightarrow F' = 3$ and $F = 4 \rightarrow F' = 5$ transitions, are separated by 452.137 MHz [62].

A.2   Excited State Polarisation Spectroscopy

The 1470 nm laser is locked to the $6P_{3/2}, F' = 5 \rightarrow 7S_{1/2}, F'' = 4$ transition using excited state polarisation spectroscopy [65]. The principle is similar to that of ground state polarisation spectroscopy, but here the pump and probe are of different
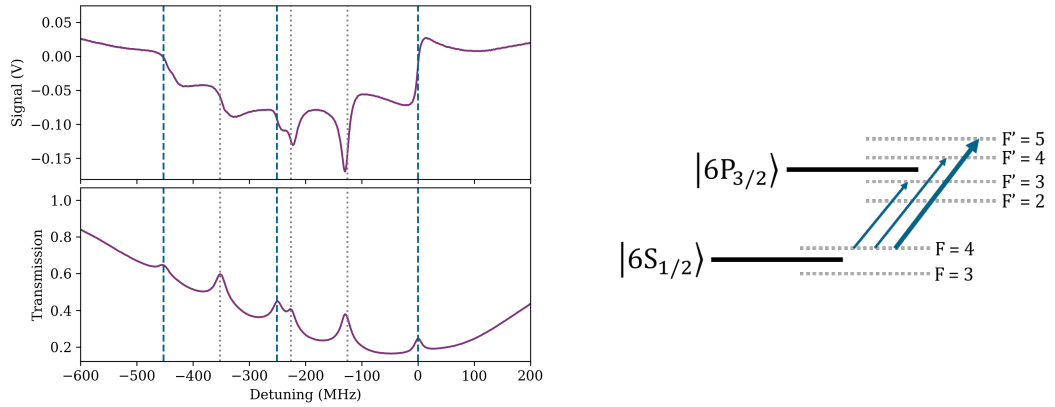
Figure A.1: **Ground state polarisation spectroscopy.** *Left:* Polarisation spectroscopy signal (upper) and saturated absorption spectroscopy signal (lower) of part of the D2 line in Cs. The blue dashed lines show features due to hyperfine transitions (F = 4 → F' = 3, 4, 5 from left to right), the grey dotted lines show the locations of crossover resonances. Zero detuning is set to be resonant with the F = 4 → F' = 5 closed transition, used for laser locking. *Right:* Hyperfine transitions responsible for the features indicated by the blue dashed lines are shown with blue arrows. The closed transition used for laser stabilisation is shown in bold.

frequencies. A circularly polarised pump beam resonant with the $6S_{1/2}, F = 4 \rightarrow 6P_{3/2}, F' = 5$ transition transfers population into the $m_{F'} = F'$ state. This optical pumping creates an anisotropy in the response of the vapour to a linearly polarised probe beam resonant with the $6P_{3/2}, F' = 5 \rightarrow 7S_{1/2}, F'' = 4$ transition. As there are no σ^+ transitions possible from the $6P_{3/2}$, $F' = 5$, $m_{F'} = 5$ state, the component of the probe beam driving σ^+ transitions will experience less absorption than the component driving σ^- transitions. As in ground state polarisation spectroscopy, this difference in absorption results in a rotation of the polarisation of the probe beam.
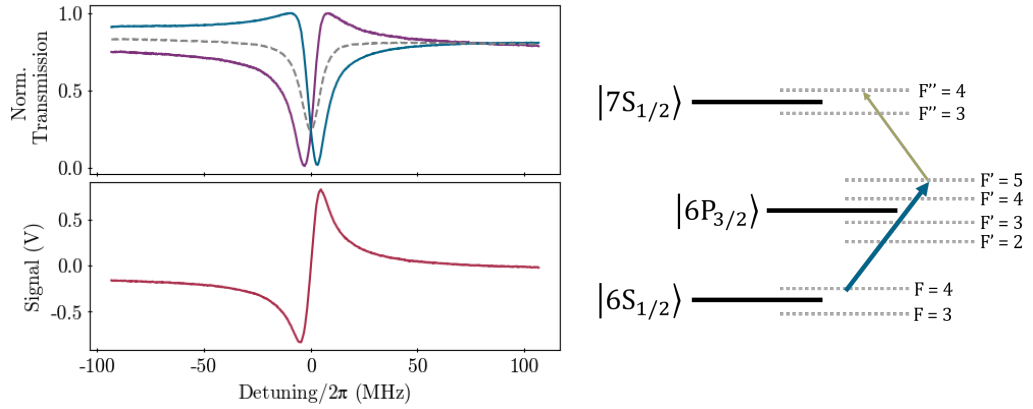
Figure A.2: **Excited state polarisation spectroscopy** *Left*: The signals recorded at each photodiode individually is shown on the upper plot. The dashed line is the average transmission, found by adding the two signals. The lower plot shows the dispersive anisotropy signal used as the error signal for laser locking, found by subtracting the two individual photodiode signals. *Right:* The hyperfine levels involved in the excited state polarisation spectroscopy scheme. The blue and green arrows represent the transition addressed by the pump (852 nm) and probe (1470 nm) lasers respectively.

Appendix B

Quantum Defect Measurements

In Chapter 4 we evaluated new values for the quantum defects in Cs by performing a global fit. We also noted that this was not the method that had been used previously in literature for calculating these values. Here we will follow the approach to obtaining values for quantum defects previously used in literature and show why we decided it was not the best way to use our data.

The frequency interval $\nu_{n,n'}$ between two levels with equal l and j and principal quantum numbers n and n' can be expressed using the Rydberg formula

$$\nu_{n,n'} = R_{\text{red}}c \left(\frac{1}{(n - \delta_{lj}(n))^2} - \frac{1}{(n' - \delta_{lj}(n'))^2} \right) \tag{2.0.1}$$

where R_{red} is the reduced Rydberg constant equal to Re/h, c is the speed of light and $\delta_{lj}(n)$ is the quantum defect for a given value of l and j. For each l and j the n-dependence of the quantum defect can be parametrised through the Ritz formula as

$$\delta(n) = \delta_0 + \frac{\delta_2}{(n - \delta_0)^2} + \frac{\delta_4}{(n - \delta_0)^4} + \frac{\delta_6}{(n - \delta_0)^6} + ... \tag{2.0.2}$$

Measuring the quantum defects hence comes down to determining the coefficients $\delta_{0,2,4}$ for given values of l and j.

B.1   Calculating Quantum Defects Using Two-Photon Transitions

Since the quantum defects have both l and j dependence, experiments usually use two-photon transitions between states with the same value of l and j such that there is only a single quantum defect value to consider [86, 89]. Even though our experiment measured single photon intervals we can combine pairs of transitions with a state in common to determine the interval between two states with the same value of l and j. We will use the example of calculating the quantum defect for the $P_{3/2}$ states; in this case the pairs of transitions will have either an $S_{1/2}$ or $D_{5/2}$ state in common. From our data we identify 6 pairs of transitions that can be used in this calculation. The next step is to use the measured single-photon transition frequencies to calculate the frequency of the 'two-photon' $nP_{3/2} \rightarrow n'P_{3/2}$ transition. In order to do this we first determine the configuration of the states used to know whether to add or subtract the frequencies. Fig. B.1 shows the three possible configurations of transitions. In the first two cases the common state (S/D) is higher/lower in energy than the P states so the frequency difference between the P states (grey arrow) is found from the difference in the transition frequencies (red arrows). In the third case the common state lies between the two P states, so the two-photon frequency is found by adding the two single photon transition frequencies.

We follow the approach of Li et al. [89] (who in turn follows Goy et al. [86]) in which they use 'two-photon techniques to measure the $ns \rightarrow (n+1)s$ and $nd \rightarrow (n+1)d$ intervals and from them derive improved quantum defects' in Rb.

We start by obtaining an 'average' quantum defect $\delta^*(n, n')$ for each interval from the measured frequency by rewriting equation 2.0.1 as

$$\Delta_\mathrm{f}(n, n') = R_\mathrm{red}c \left(\frac{1}{(n - \delta^*(n, n'))^2} - \frac{1}{(n' - \delta^*(n, n'))^2} \right). \qquad (2.1.3)$$

This can be solved to give a value of δ^* for each interval. These average quantum defects are then plotted against $1/n^{*2}$ where $n^* = \frac{(n+n')}{2} - 3.5589599$. Here 3.5589599 is the previously quoted literature value of δ_0. From performing a linear fit as shown in Fig. B.2 we can extract initial estimates for δ_0^* and δ_2^*.
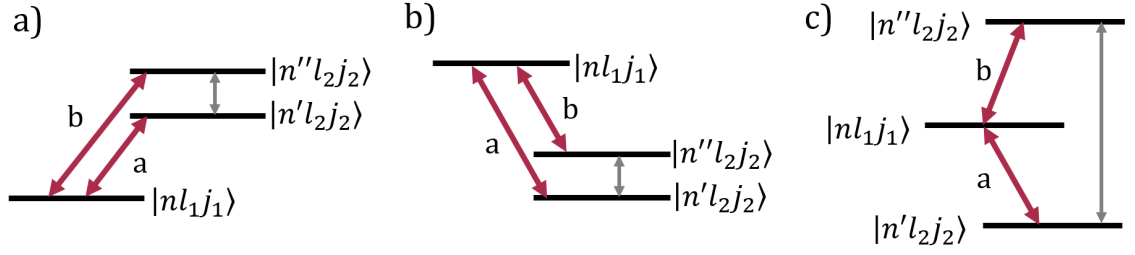
Figure B.1: **State configurations for determining effective 2-photon transition frequencies.** In cases a and b the transition frequency between states with equal l and j (grey arrow) can be found as the difference between the single-photon transition frequencies (red arrows). In case c the 2-photon transition is found as the sum of the two single-photon transitions.
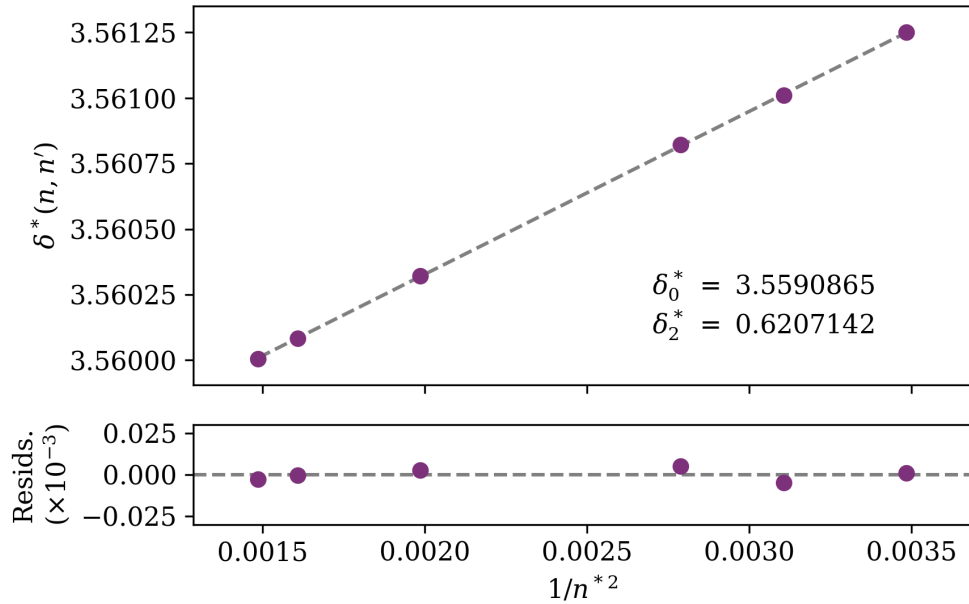

Figure B.2: **Estimating quantum defects.** The average quantum defect δ^* plotted as a function of $1/n^{*2}$. From the linear fit we extract values of δ_0^* and δ_2^*.
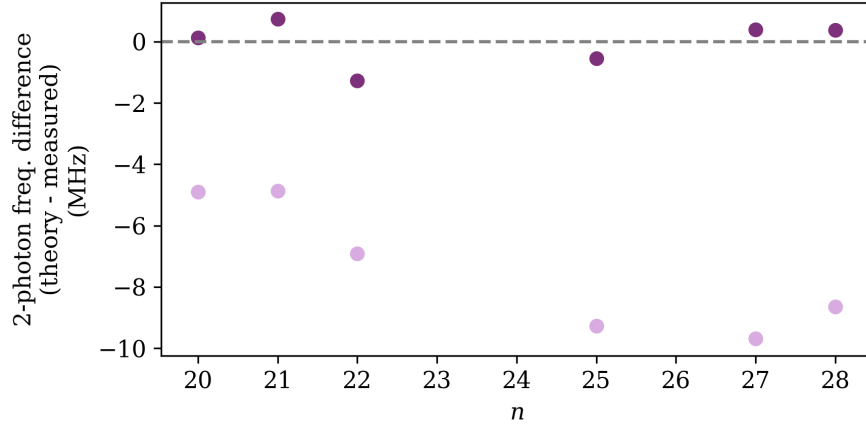
Figure B.3: **Difference between theory and experimental 2-photon intervals.** The difference between our measured 2-photon transition frequencies and those calculated from equation 2.0.1 using both the previous literature values (light purple) and our new optimised values (dark purple) for δ_0 and δ_2.

These preliminary estimates are then used as a starting point for an optimisation to minimise the difference between the measured two-photon transition frequencies and those predicted using equation 2.0.1. The results of this optimisation (using the `scipy.optimize.curve_fit` function in Python) gives values of $\delta_0 = 3.55907055$ and $\delta_2 = 0.37424433$. The difference between the theoretical values of the two-photon transition frequencies and our measured two-photon intervals are shown in Fig. B.3 for both the initial and optimised values of δ_0 and δ_2. Our new optimised values clearly reduce the difference between the predicted and observed two-photon intervals.

Ideally we would use this method to calculate optimised values for the quantum defects of all series for which we have data ($S_{1/2}$, $P_{1/2,3/2}$ and $D_{3/2,5/2}$). However for some series we have very few suitable transition pairs with which to calculate two-photon intervals. For instance we have only 3 datapoints for the $P_{1/2}$ series and 4 in each of the D series. Using this method on this data would involve performing fits and optimisations with a comparable number of datapoints to the free parameters in the model. Out of a total of 63 measured transition frequencies, the requirement of finding transitions with states in common such that we can extract the two-photon interval leaves us with only 27 viable measurements. This leads us to the conclusion

that this is not the best method for calculation of the quantum defects in Cs from our data, hence in Chapter 4 we perform an optimisation simultaneously for all series, allowing us to make use of all our measured datapoints.

B.2 Calculating Quantum Defects From Fine Structure Intervals

When presenting values for the quantum defects that have been previously reported in literature (see Table 4.1) we noted that the values for the quantum defects of the $n\mathrm{P}_{3/2}$ and $n\mathrm{D}_{3/2}$ were not directly reported in [85]. Instead they state that the values of the quantum defects for these series can be derived from the quantum defects for the $n\mathrm{P}_{1/2}$ and $n\mathrm{D}_{5/2}$ series and knowledge of the relevant fine structure intervals. Again this fine-structure data is not presented in [85] but referenced from [86] and [87]. In order to compare our measured values for the quantum defects to those given in [85] we use this fine-structure data to predict what values would have been presented in [85] for the $n\mathrm{P}_{3/2}$ and $n\mathrm{D}_{3/2}$ series. We will outline the method used to calculate the values for the $n\mathrm{P}_{3/2}$ series (using fine structure data in [87]) and note that the method used for the $n\mathrm{D}_{3/2}$ series is identical but uses data from [86]. To calculate the fine structure interval Δ_{fs}, we use an empirical formula proposed by Pendrill [150]

$$\Delta_{\mathrm{fs}} = \frac{A}{(n^*)^3} + \frac{B}{(n^*)^4} + \frac{C}{(n^*)^5} + \frac{D}{(n^*)^6} + \frac{E}{(n^*)^7}, \qquad (2.2.4)$$

where A, B, C, D, E are coefficients extracted from fitting given in Table IV of [87], and n^* is the effective quantum number defined through

$$n^* = n^*_\infty - \frac{a}{(n^*_\infty)^2} - \frac{b}{(n^*_\infty)^4} - \frac{c}{(n^*_\infty)^6}. \qquad (2.2.5)$$

Here $n^*_\infty = n - \epsilon_\infty$ and the values of a, b, c and ϵ_∞ are given in Table III of [87].

The fine structure intervals in the P series can be expressed as

$$\Delta_{\mathrm{fs}} = \frac{-R_\infty e}{h} \left(\frac{1}{(n - \delta_{P_{1/2}})^2} + \frac{1}{(n - \delta_{P_{3/2}})^2} \right), \qquad (2.2.6)$$
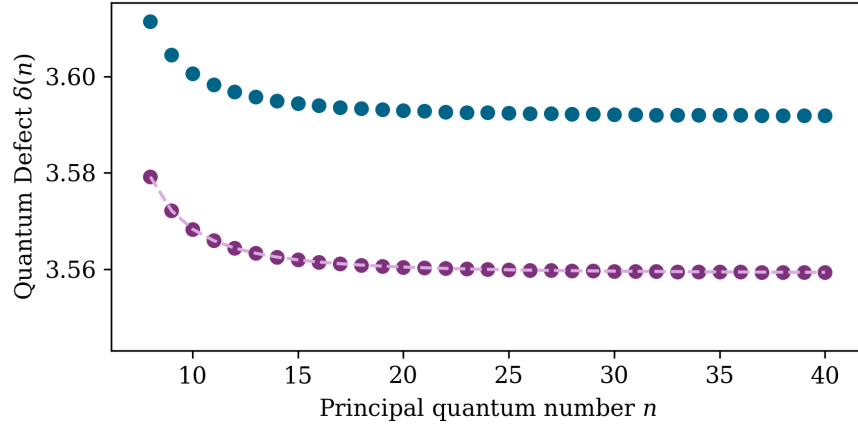
Figure B.4: **Calculating quantum defects from fine structure intervals.** The values for the quantum defects for $P_{1/2}$ (blue) and $P_{3/2}$ (purple) series as a function of n, calculated from formulas in [85] and [87]. The light purple dashed line indicates the fitted Ritz equation (eqn. 4.4.6) from which we extract the coefficients of the quantum defects for the $P_{3/2}$ series.

where $\delta_{P_{1/2,3/2}}$ is the quantum defect for the relevant level. Rearranging this we find that the quantum defect for the $P_{3/2}$ states is related to that for the $P_{1/2}$ states and the fine-structure interval through

$$\delta_{P_{3/2}}(n) = n - \sqrt{\left(\frac{1}{(n - \delta_{P_{1/2}}(n))^2} - \frac{h\Delta_{\text{fs}}}{Re} \right)}. \qquad (2.2.7)$$

This allows us to use the fine-structure intervals as calculated above along with the quantum defects given in [85] to determine values of $\delta_{P_{3/2}}$ for $8 < n < 40$. These values, along with those using the coefficients in [85] are shown in Fig. B.4. We then fit the Ritz formula (eqn. 4.4.6) to these values to obtain values for the coefficients of the quantum defect $\delta_{0,2,4}$ for the $nP_{3/2}$ series. This fit is indicated by the dashed line in Fig. B.4. The values for these coefficients are given in Table 4.1 and are indicated by (*). The uncertainties are those given by the fitting algorithm used.